UNIVERSIDADE FEDERAL DO CEARÁ
CENTRO DE TECNOLOGIA
DEPARTAMENTO DE ENGENHARIA METALÚRGICA E DE MATERIAIS
PROGRAMA DE PÓS-GRADUAÇÃO EM ENGENHARIA E CIÊNCIA DE MATERIAIS

LARYSSA COUTINHO DA SILVA

BIOCHAR AND BIOCHAR-BENTONITE COMPOSITE FROM CARNAUBA (*COPERNICIA PRUNIFERA*) STRAW MODIFIED BY HIGH-ENERGY BALL MILLING: PREPARATION, CHARACTERIZATION, AND METHYLENE BLUE ADSORPTION

FORTALEZA
2026

LARYSSA COUTINHO DA SILVA

BIOCHAR AND BIOCHAR-BENTONITE COMPOSITE FROM CARNAUBA (*COPERNICIA PRUNIFERA*) STRAW MODIFIED BY HIGH-ENERGY BALL MILLING: PREPARATION, CHARACTERIZATION, AND METHYLENE BLUE ADSORPTION

Dissertation presented to the Postgraduate Program in Materials Science and Engineering of the Federal University of Ceará as a partial requirement for the degree of Master of Science in Materials Science and Engineering.

Supervisor: Prof. Dr. Ricardo Emílio Ferreira Quevedo Nogueira.

FORTALEZA

2026

LARYSSA COUTINHO DA SILVA

BIOCHAR AND BIOCHAR-BENTONITE COMPOSITE FROM CARNAUBA (*COPERNICIA PRUNIFERA*) STRAW MODIFIED BY HIGH-ENERGY BALL MILLING: PREPARATION, CHARACTERIZATION, AND METHYLENE BLUE ADSORPTION

Dissertation presented to the Postgraduate Program in Materials Science and Engineering of the Federal University of Ceará as a partial requirement for the degree of Master of Science in Materials Science and Engineering.

.

Approved on: 02/06/2026

EXAMINING COMMITTEE

_____

Prof. PhD. Ricardo Emílio Ferreira Quevedo Nogueira (Orientador)
Universidade Federal do Ceará (UFC)

_____

Prof. PhD. Maria Alexsandra de Sousa Rios
Universidade Federal do Ceará (UFC)

_____

Prof. PhD. Men de Sa Moreira de Souza Filho
Empresa Brasileira de Pesquisa Agropecuária (EMBRAPA)

For those who seek knowledge and strive to make a difference.

ACKNOWLEDGEMENTS

I am deeply grateful to my family for their support, encouragement, and understanding throughout my academic journey. I also sincerely thank Pedro Queiros Santiago, with whom I jointly conducted analyses and experiments, making a significant contribution to the development of this work.

I sincerely thank Prof. Ricardo Emilio Nogueira for his guidance throughout this research. I am also deeply grateful to Prof. Maria Alexandra Rios for providing equipment and necessary materials to this research. I also thank the examination committee members for their time.

I would like to express my gratitude to the staff of the following laboratories for their support and assistance: the Technological Innovations and Chemical Specialties Group (GRINTEQUI) for support with material preparation and proximate analysis; the X-Ray Laboratory (LRX) for X-ray diffraction measurements; the Electron Microscopy Laboratory (LME) for SEM/EDS analyses; the Vibrational Spectroscopy Laboratory (LEV) for FTIR measurements; the Advanced Materials Laboratory for high-energy ball milling and thermal analysis (TG/DTG); the Biomaterials Laboratory for providing the centrifuge; and the Analytical Center of the Postgraduate Program in Chemistry for assistance with UV–Vis measurements.

This study was financed in part by the Coordenação de Aperfeiçoamento de Pessoal de Nível Superior - Brasil (CAPES) - Finance Code 001.

“To learn and then have occasion to practice what you have learned – is this not satisfying?”(Confucius, *The Analects,* Book I)

ABSTRACT

The conversion of agrowaste into engineered adsorbent materials represents a sustainable strategy for wastewater treatment. Biochar and biochar–clay composites were prepared from raw and dewaxed carnauba (*Copernicia Prunifera*) straw through high-energy ball milling (HEBM) and evaluated for methylene blue (MB) adsorption. Carbonization at 550 °C enriched fixed carbon and ash while reducing volatile matter. Dewaxed biochar (DCSB) exhibited higher carbon content (45.63 wt%) and a higher degree of carbonization compared to non-dewaxed biochar (CSB), leading to superior adsorption performance (Langmuir q_m = 328.13 mg g^{-1} for DCSB vs. 255.70 mg g^{-1} for CSB). SEM analysis revealed that HEBM produced highly fragmented materials with a fine powder-like morphology, while FTIR and XRD analyses confirmed the preservation of the fundamental chemical structure and the predominantly amorphous character of the biochars. A material-dependent response to HEBM was observed: CSB required higher specific energy (26.46 kJ g^{-1}) to reach its maximum adsorption capacity, whereas DCSB achieved its optimum at a much lower energy (7.86 kJ g^{-1}), indicating that dewaxing alters the biochar's susceptibility to mechanochemical activation. Notably, bentonite-containing composites exhibited broader energy tolerance, maintaining high adsorption performance across a wide range of milling conditions, indicating greater robustness of the composites to variations in HEBM conditions. FTIR, EDS, and XRD analyses confirmed the successful incorporation of bentonite into the composites. HEBM enhanced adsorption kinetics, while bentonite improved removal efficiency (up to 97.75%) and surface heterogeneity. Among modified samples, adsorption followed the Elovich model (R^2 up to 0.99), suggesting the presence of heterogeneous adsorption sites, while equilibrium data were best described by the Freundlich isotherm (R^2 up to 0.97). Maximum adsorption capacities calculated from the Langmuir model reached 307.86 mg g^{-1} (BDCSB4002) and 274.61 mg g^{-1} (DCSB2006), although the Langmuir model did not provide the best fit for the modified materials reflecting the heterogeneous nature of the adsorption process. The adsorption mechanism involves π–π interactions, electrostatic attraction, hydrogen bonding, and intraparticle diffusion. These findings demonstrate that DCSB exhibits the highest Langmuir maximum adsorption capacity, HEBM and bentonite modification offer improvements in adsorption kinetics and removal efficiency, supporting the potential of engineered carnauba biochar and biochar–clay composites as sustainable adsorbents dye removal in wastewater treatment.

Keywords: biochar; carnauba; high energy ball milling; bentonite; methylene blue; adsorption.

RESUMO

A conversão de resíduos agroindustriais em materiais adsorventes desenvolvidos representa uma estratégia sustentável para o tratamento de águas residuais. Biochar e compósitos biochar–argila foram preparados a partir de palha de carnaúba (*Copernicia prunifera*) in natura e com remoção da cera por moagem de alta energia (MAE) e avaliados quanto à adsorção do corante azul de metileno (AM). A carbonização a 550 °C enriqueceu o carbono fixo e as cinzas, enquanto reduziu os voláteis. O biocarvão desencerado (DCSB) apresentou maior teor de carbono (45,63%) e maior grau de carbonização em comparação ao biocarvão não desencerado (CSB), promovendo melhor adsorção (Langmuir q_m= 328.13 mg g^{-1} for DCSB vs. 255.70 mg g^{-1} for CSB). As análises de SEM revelaram que a HEBM produziu materiais altamente fragmentados, com morfologia semelhante a um pó fino, enquanto as análises de FTIR e DRX confirmaram a preservação da estrutura química fundamental e das características difratométricas típicas de biocarvões predominantemente amorfos. Observou-se uma resposta dependente do material à MAE: o CSB necessitou de maior energia específica (26.46 kJ g^{-1}) para atingir sua capacidade máxima de adsorção, enquanto o DCSB alcançou seu ótimo com energia muito menor (7,86 kJ g^{-1}), indicando que a descera altera a suscetibilidade do biocarvão à ativação mecanoquímica. Notavelmente, os compósitos contendo bentonita exibiram maior tolerância energética, mantendo alto desempenho de adsorção em uma ampla faixa de condições de moagem, indicando maior robustez dos compósitos frente a variações nas condições de HEBM. As análises de FTIR, EDS e DRX confirmaram a incorporação bem-sucedida da bentonita aos compósitos. A MAE melhorou a cinética de adsorção, enquanto a bentonita aumentou a eficiência de remoção (até 97,75%) e a heterogeneidade superficial. Entre as amostras modificadas, a adsorção seguiu o modelo de Elovich (R^2 até 0,99), sugerindo a presença de sítios de adsorção heterogêneos, enquanto os dados de equilíbrio foram mais bem descritos pela isoterma de Freundlich (R^2 até 0,97). As capacidades máximas de adsorção calculadas pelo modelo de Langmuir atingiram 307,86 mg g^{-1} (BDCSB4002) e 274,61 mg g^{-1} (DCSB2006), embora o modelo de Langmuir não tenha fornecido o melhor ajuste para os materiais modificados, refletindo a natureza heterogênea do processo de adsorção. O processo de adsorção é provavelmente governado por uma combinação de interações π–π, atração eletrostática, ligações de hidrogênio e difusão intrapartícula. Esses achados demonstram que, embora o biocarvão DCSB exiba a maior capacidade máxima de adsorção pelo modelo de Langmuir, a MAE e a incorporação de bentonita proporcionam melhorias na cinética de adsorção e na eficiência de remoção, corroborando o potencial do biocarvão de carnaúba e de

seus compósitos como adsorventes sustentáveis para a remoção de corantes em tratamento de águas residuárias.

Palavras -chave: biocarvão; carnaúba; moagem de alta energia; azul de metileno; adsorção

LIST OF FIGURES

LIST OF TABLES

ABREVIATIONS AND ACRONYMS LIST

AEC	Anion Exchange Capacity
AISI	American Iron and Steel Institute
ASTM	American Society for Testing and Materials
ATR	Attenuated Total Reflectance
BCC	Biochar–Clay Composite
BET	Brunauer–Emmett–Teller
BSE	Backscattered Electron
C	Carbon (elemental)
CAS	Chemical Abstracts Service Registry Number
CEC	Cation Exchange Capacity
CHNS	Carbon, Hydrogen, Nitrogen, Sulfur (elemental analysis)
CS	Carnauba Straw
CSB	Carnauba Straw Biochar
DCS	Dewaxed Carnauba Straw
DCSB	Dewaxed Carnauba Straw Biochar
DLaTGS	Deuterated L-Alanine Doped Triglycine Sulfate (detector)
DLS	Dynamic Light Scattering
DSC	Differential Scanning Calorimetry
DTA	Differential Thermal Analysis
DTG	Derivative Thermogravimetry
EBC	European Biochar Certificate
EDA	Electron Donor–Acceptor
EDS	Energy-Dispersive X-ray Spectroscopy
FC	Fixed Carbon
FTIR	Fourier Transform Infrared Spectroscopy
H	Hydrogen (elemental)
HEBM	High-Energy Ball Milling
HTC	Hydrothermal Carbonization
IBGE	Instituto Brasileiro de Geografia e Estatística (Brazil)
MB	Methylene Blue
MC	Moisture Content
MW	Molecular Weight

N	Nitrogen (elemental)
NaHMP	Sodium Hexametaphosphate
NBC	Nanobiochar
OPEFB	Oil Palm Empty Fruit Bunch
PEVS	Produção da Extração Vegetal e da Silvicultura (Brazil)
PFO	Pseudo-First Order
PSO	Pseudo-Second Order
rpm	Rotations per minute
RSM	Response Surface Methodology
SDG	Sustainable Development Goal (UN)
SE	Secondary Electron
SEM	Scanning Electron Microscopy
SSA	Specific Surface Area
TG	Thermogravimetric Analysis
UV–Vis	Ultraviolet–Visible Spectroscopy
VM	Volatile Matter
WGS	World Geodetic System 1984
XRD	X-ray Diffraction

SYMBOL LIST

C_o	Initial concentration of adsorbate
C_e	Equilibrium concentration of adsorbate
q_e	Adsorption capacity at equilibrium
q_t	Adsorption capacity at time *t*
q_m	Maximum adsorption capacity (Langmuir)
K_L	Langmuir constant (affinity)
K_F	Freundlich constant
N	Freundlich exponent
k_1	Pseudo-first-order rate constant
k_2	Pseudo-second-order rate constant
k_p	Intraparticle diffusion constant
R_L	Separation factor (Langmuir)
V	Volume of solution
M	Adsorbent mass
H	Removal efficiency
T	Time
A	Initial sorption rate (Elovich model)
B	Desorption constant (Elovich model)
C	Boundary layer thickness (Weber–Morris)
R^2	Coefficient of determination
T	Temperature
pH	Negative logarithm of H^+ concentration
Λ	Wavelength
Ω	Angular velocity
R	Radius
V	Velocity
F	Impact frequency
E	Specific milling energy
P	Power
S	Detachment parameter
D	Interlayer spacing (XRD)
2θ	Bragg angle

wt%	Weight percent
SD	Standard deviation

TABLE OF CONTENT

1 INTRODUCTION

The contamination of soil, water, and air by inorganic and organic pollutants has intensified due to anthropogenic activities, posing significant risks to ecosystems and human health. Hazardous compounds, such as pharmaceuticals, pesticides, per- and polyfluoroalkyl substances, hydrocarbons, dioxins, and synthetic dyes, have been widely reported as emerging contaminants (Wijesooriya *et al.*, 2023).

Synthetic dyes are of particular concern due to their widespread industrial use and frequent release into aquatic environments through continuous discharges, accidental spills, and improper disposal during production, transportation, and wastewater handling(Arif *et al.*, 2021; Tkaczyk; Mitrowska; Posyniak, 2020). Even at low concentrations, dyes cause intense coloration, reduce light penetration, and adversely affect aquatic ecosystems, as illustrated in Figure 1. Addressing dye-contaminated waters is therefore essential for sustainable water management and aligns with the United Nations Sustainable Development Goal 6, which aims to improve access to safe water and sanitation, particularly through Target 6.3, focused on minimizing pollutant discharges and promoting efficient and economically viable wastewater treatment solutions(United Nations General Assembly, 2015).

Figure 1 - Environmental contamination of aquatic systems by synthetic dyes: (a) malachite green spill in Jundiaí, Brazil; (b) wildlife affected by blue dye; (c) red dye discharge into the Jian River, China; (d) industrial dye effluents entering the Caledon River, Lesotho

Source: Adapted from – a) and b) Vazamento..(2024); c) Our...(2020) and d) Blue…(2021)

Several technologies, including membrane separation, ion exchange, advanced oxidation, and biological degradation, have been employed for remediation purposes (Fernandes *et al.*, 2011). However, these methods are often limited by high operational costs, energy consumption, and technical complexity, which hinder their large-scale application. In

contrast, adsorption has emerged as a promising alternative due to its simplicity, cost-effectiveness, and scalability, provided that suitable adsorbent materials are developed (Jiang *et al.*, 2023).

Biochar, a carbon-rich porous material produced by the thermochemical conversion of biomass under oxygen-limited conditions, has gained recognition as an environmentally sustainable adsorbent. Its advantages include high specific surface area, tunable surface chemistry, cation-exchange capacity, and the possibility of being derived from renewable waste feedstocks (Akanji *et al.*, 2023; Wijesooriya *et al.*, 2023). Despite these intrinsic properties, pristine biochar often exhibits limited adsorption capacity for some pollutants, which has led to a growing interest in its modification through chemical, physical, or mechanical routes(Bao *et al.*, 2022).

Clay minerals, such as bentonite, kaolinite, and vermiculite, have long been used as adsorbents owing to their abundance, low cost, high cation-exchange capacity, and surface area. In addition to direct use, clays can be physically or chemically modified to improve selectivity and efficiency, or incorporated into composites with materials such as polymers, biochar, or nanoparticles. Among these, biochar-clay composites (BCC) have attracted increasing attention, as they combine the structural stability and ion-exchange properties of clays with the porosity, functional groups, and adsorption potential of biochar(Akanji *et al.*, 2023; Wijesooriya *et al.*, 2023).

High-energy ball milling (HEBM) has recently emerged as a promising technique for biochar modification. By applying strong mechanical forces, HEBM reduces particle size to the nanoscale, increases surface area, alters crystallinity, and enhances the abundance of surface functional groups(Dellisanti; Valdré, 2005; Jiang *et al.*, 2023; Lopez-Tenllado; Motta; Hill, 2021). For instance, montmorillonite–biochar composites prepared by ball milling have demonstrated high removal of organic dyes, while vermiculite–biochar composites enhanced the adsorption of arsenic species due to increased surface area and cation activation(Jiang *et al.*, 2023).

Methylene blue (MB), a cationic dye widely used in the textile and printing industries, is often discharged into water streams, where it poses ecological and health risks due to its toxicity and persistence (Jiang *et al.*, 2023; Khan *et al.*, 2022). Its removal has therefore been extensively studied as a model system for testing adsorbents(Khan *et al.*, 2022; Oladoye *et al.*, 2022). Given the potential of mineral–biochar composites and the growing that HEBM can

enhance their adsorption efficiency, the development of engineered adsorbents targeting MB removal remains an active research area.

The carnauba palm (*Copernicia prunifera*), native to northeastern Brazil, is an abundant biomass source. Its leaves, typically used for wax extraction, are the main agro-industrial residue and represent a potential bioadsorbent (Fernandes et al., 2011; Ferreira da Silva et al., 2018; Junio et al., 2022, 2023; Pereira et al., 2020). Previous research has primarily investigated the use of carnauba dewaxed leaves as an adsorbent for heavy metals, such as Cu, and synthetic dyes(Ferreira da Silva et al., 2018; Goes et al., 2019; Pereira et al., 2021). Furthermore, a study demonstrated that incorporating this material into a bentonite-based composite further enhanced its adsorption performance(Pereira *et al.*, 2020). However, the production of biochar and biochar–clay composites from carnauba leaves for adsorption applications remains unexplored in the literature.

1.1 Objectives

1.1.1 General Objective

To produce and characterize biochar and biochar–bentonite composites derived from raw and dewaxed carnauba (*Copernicia prunifera)* straw via high-energy ball milling, and to evaluate their adsorption performance for methylene blue removal from aqueous solutions, thereby supporting the achievement of United Nations Sustainable Development Goals (SDGs) 6, 12, and 13.

1.1.2 Specific Objectives

- To produce biochar from raw and dewaxed *Copernicia prunifera* straw.
- To prepare biochar–bentonite composites using high-energy ball milling (HEBM).
- To evaluate the effect of dewaxing and bentonite incorporation on the physicochemical properties of the produced materials.
- To characterize the produced biochar and biochar–clay composites using techniques such as X-ray diffraction (XRD), Fourier-transform infrared spectroscopy (FTIR), electron microscopy, and thermal analysis.
- To evaluate the adsorption capacity of modified and unmodified biochar for methylene blue dye under different experimental conditions.
- To analyze the adsorption data to determine the involved mechanisms and applicable kinetic and isotherm models.

2 LITERATURE REVIEW

2.1 Sustainable Development Goals and Circular Bioeconomy

The growing demand for natural resources and the increasing generation of waste have intensified global efforts toward the development of more sustainable production systems. In this context, the United Nations established the 2030 Agenda for Sustainable Development, which comprises 17 Sustainable Development Goals (SDGs) designed to address major environmental, economic, and social challenges. Among these goals, SDG 6 (Clean Water and Sanitation), SDG 12 (Responsible Consumption and Production), and SDG 13 (Climate Action) are particularly associated with resource management, waste reduction, and environmental protection(United Nations General Assembly, 2015).

Achieving these goals requires a transition from the traditional linear economy model, based on extraction, use, and disposal, toward more sustainable frameworks(United Nations General Assembly, 2015). The concepts of circular economy and bioeconomy have emerged as complementary approaches capable of supporting this transition(Ferraz; Pyka, 2023; Ubando; Felix; Chen, 2020). While the circular economy aims to maintain the value of materials and resources within production systems for as long as possible, the bioeconomy focuses on the sustainable utilization of renewable biological resources to produce materials, chemicals, and energy(Ferraz; Pyka, 2023; Sherwood, 2020; Ubando; Felix; Chen, 2020).

The integration of these concepts has led to the development of the circular bioeconomy, a framework that promotes the efficient use of biomass resources while minimizing waste generation(Ferraz; Pyka, 2023). Recent studies have highlighted circular bioeconomy as an important pathway for achieving several SDGs, particularly those related to sustainable production, environmental protection, and resource efficiency. Furthermore, the valorization of agricultural and agro-industrial residues has been identified as a key strategy for reducing environmental impacts and generating additional economic value from biomass streams(Awasthi *et al.*, 2020; Song *et al.*, 2021).

Biomass plays a central role in circular bioeconomy systems because, unlike fossil resources, it can be continuously regenerated through natural cycles(Awasthi *et al.*, 2020). Lignocellulosic residues generated by agricultural and forestry activities represent abundant renewable feedstocks that can be transformed into a wide range of value-added products. Their utilization contributes not only to waste reduction but also to the replacement of non-renewable raw materials, supporting more sustainable production chains*(Sherwood, 2020)*.

Among the available biomass valorization routes, thermochemical conversion technologies enable the transformation of lignocellulosic residues into value-added products(Ubando; Felix; Chen, 2020). Biochar has gained increasing attention due to its versatility and potential applications in environmental remediation, soil improvement, carbon sequestration, catalysis, and water treatment(Sun *et al.*, 2025; Xie *et al.*, 2022). Moreover, its production from biomass residues aligns with circular bioeconomy principles by promoting waste valorization, resource recovery, and pollution mitigation(Ferraz; Pyka, 2023; Sherwood, 2020).

2.2 Lignocellulosic Biomass

Biomass encompasses all biologically produced organic matter(Fahmy *et al.*, 2020). Lignocellulosic biomass is a category of biomass whose major constituents are cellulose, hemicellulose, and lignin, while minor components include extractive and inorganic components(Dai *et al.*, 2020; Kambo; Dutta, 2015; Nascimento; Neto, 2014; Qin *et al.*, 2022; Seow *et al.*, 2022).

As illustrated in Figure 2, cellulose, hemicellulose, and lignin are intimately interwoven and interconnected through a network of non-covalent bonds and cross-links, which confer structural integrity and rigidity to plant cell walls(Dai *et al.*, 2020; Kambo; Dutta, 2015).

Figure 2 - Lignocellulosic Biomass structure

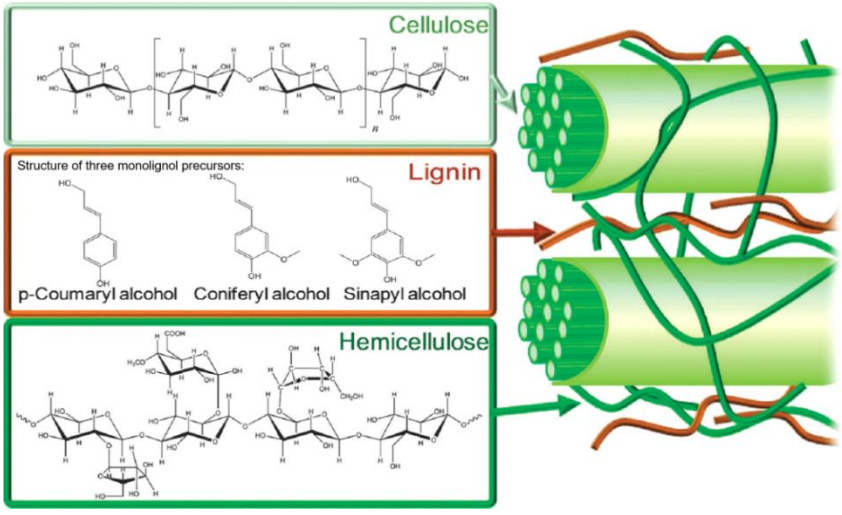

Source: Adapted from Kambo; Dutta (2015)

Cellulose forms the main structural framework of plant cell walls. It is a high–molecular weight linear polysaccharide composed of β(1–4)-linked glucose units, synthesized through the photosynthetic conversion of CO_2 and water(Dai *et al.*, 2020; Kambo; Dutta, 2015; Qin *et al.*, 2022).

Hemicellulose is a heterogeneous class of polymers produced via various enzymatic reactions, whose sugar monomers — such as xylose, mannose, galactose, etc. — varies according to the plant species. With a shorter chain length than cellulose, it plays a key role in binding cellulose microfibrils and forming cross-links with lignin, thereby enhancing the mechanical stability of the cell wall(Dai *et al.*, 2020; Kambo; Dutta, 2015; Qin *et al.*, 2022).

Lignin, in turn, is an irregular, tridimensional aromatic polymer primarily built from monolignol precursors: coniferyl, p-coumaryl, and sinapyl alcohol. These alcohol units provide the base for the formation of lignin building blocks that are connected through several types of linkages — such as biphenyl ether, aryl ether, dibenzodioxocin, and phenylcoumaran.— as presented in Figure 3. Lignin acts as a hydrophobic matrix that imparts rigidity, impermeability, and resistance to microbial and oxidative degradation(Dai *et al.*, 2020; Kambo; Dutta, 2015; Qin *et al.*, 2022; Shah *et al.*, 2023).

Figure 3 - Main linkages of lignin structure

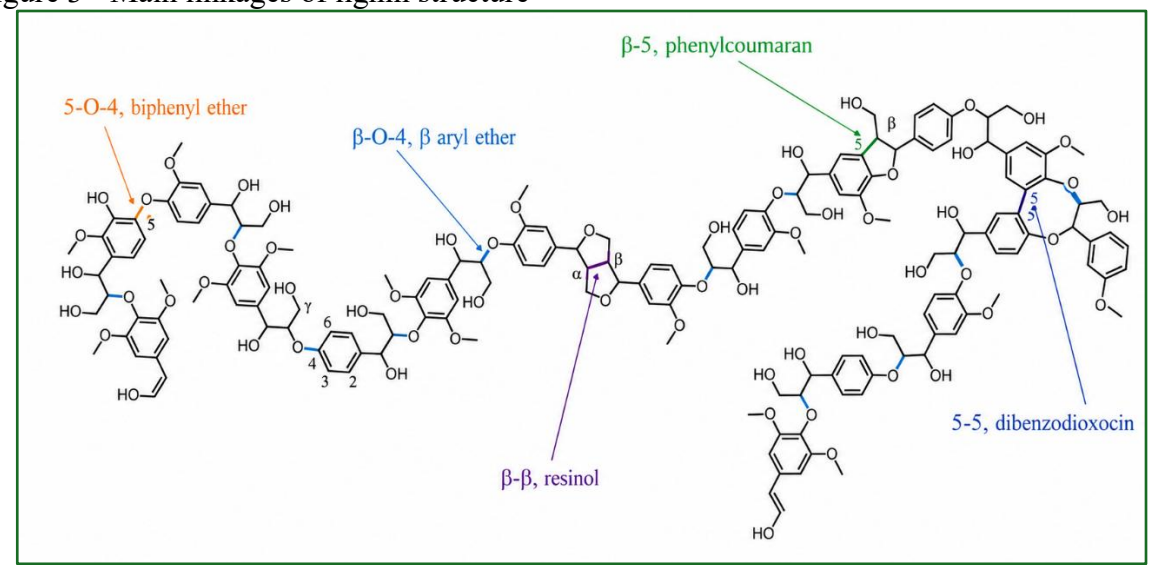

Source: Adapted from Shah et al. (2023)

The relative proportion of these macromolecules varies among different lignocellulosic feedstocks(Dai *et al.*, 2020; Seow *et al.*, 2022), and this compositional variability influences their thermal degradation behavior, thereby affecting both the yield and the physicochemical characteristics of products obtained from thermochemical conversion(Seow *et al.*, 2022; Weber; Quicker, 2018). In general, hemicellulose decomposes at approximately 200–300 °C, cellulose at 315–400 °C, and lignin over a broader temperature range between 160 to 900 ºC(Seow *et al.*, 2022).

Lignocellulosic biomass also contains a fraction of organic compounds collectively referred to as extractives(Esteves; Sen; Pereira, 2023; Lehmann; Joseph, 2015; Qin *et al.*, 2022;

Sampaio; Lima; Pires, 2025). These low-molecular-weight substances are produced through plant metabolic processes and comprise primary metabolites — such as simple sugars, amino acids, fats, and carboxylic acids — and secondary metabolites — such as phenolic compounds, terpenes, phytosterols, and aliphatics(Esteves; Sen; Pereira, 2023). The content, structure, biological function, and composition of extractives vary according to plant species, tissue type, season, age, and environmental conditions(Esteves; Sen; Pereira, 2023; Sampaio; Lima; Pires, 2025). Although they can influence gaseous emission profiles during pyrolysis, their typically low concentrations mean they are not expected to substantially affect biochar yield(Lehmann; Joseph, 2015).

The inorganic component of biomass includes macronutrients such as nitrogen (N), phosphorus (P), potassium (K), magnesium (Mg), sulfur (S), calcium (Ca), and smaller amounts micronutrients such as chlorine (Cl), alkaline earth metals, transition metals, and trace elements(Chandraratne *et al.*, 2021; Lehmann; Joseph, 2015). After complete oxidation at high temperatures, these inorganic components remain as ash, which plays an important role in combustion behavior, slagging, and fouling tendencies(Lehmann; Joseph, 2015).

2.2.1 Copernicia Prunifera as a Biomass Source

The carnauba (*Copernicia prunifera*) —Figure 4 — is a native xerophytic palm tree from northeastern Brazil that typically grows near rivers in clay or alluvial soils(Alves; Coêlho, 2008; Junio *et al.*, 2022). Carnauba palms can reach heights of up to 10 meters and produce 45–60 leaves per year(Alves; Coêlho, 2008; Junio *et al.*, 2022). The leaves are found in the crown of the plant, arranged spirally around the stem, and exhibit a slightly bluish-green hue due to the wax powder layer covering the lamina(Alves; Coêlho, 2008). The powdery wax layer on the leaves is an adaptation to arid environments. This layer reflects light, reducing heat damage to the photosynthetic system, limits water loss through transpiration, and protects against fungal infections(Alves; Coêlho, 2008).

Figure 4 - Carnauba Palm at the Pici Campus, Federal University of Ceará.

Source: Author

The density of carnauba occurrence is linked to the clay content in the soil; in alluvial soils with higher clay content, the density of palm trees is greater(Alves; Coêlho, 2008). This palm is also tolerant of prolonged droughts and floods, high salinity levels, and intense solar radiation(Alves; Coêlho, 2008; Junio *et al.*, 2022).

The annual report “Produção da Extração Vegetal e da Silvicultura (PEVS)” from the Instituto Brasileiro de Geografia e Estatística (IBGE) (2023), presents the production and value of wax powder, wax, and fibers between 2000 and 2023, as shown in Figure 5. Wax production (panel a) has declined since the mid-2000s, while its value has fluctuated with occasional peaks. Wax powder production (panel b) remained stable with oscillations, whereas its value showed strong fluctuations over the years. Fiber production (panel c) varied, but its economic value has shown a steady upward trend, especially after 2015.

Figure 5 - Production and value of (a) wax (b) wax powder and (c) fibers.

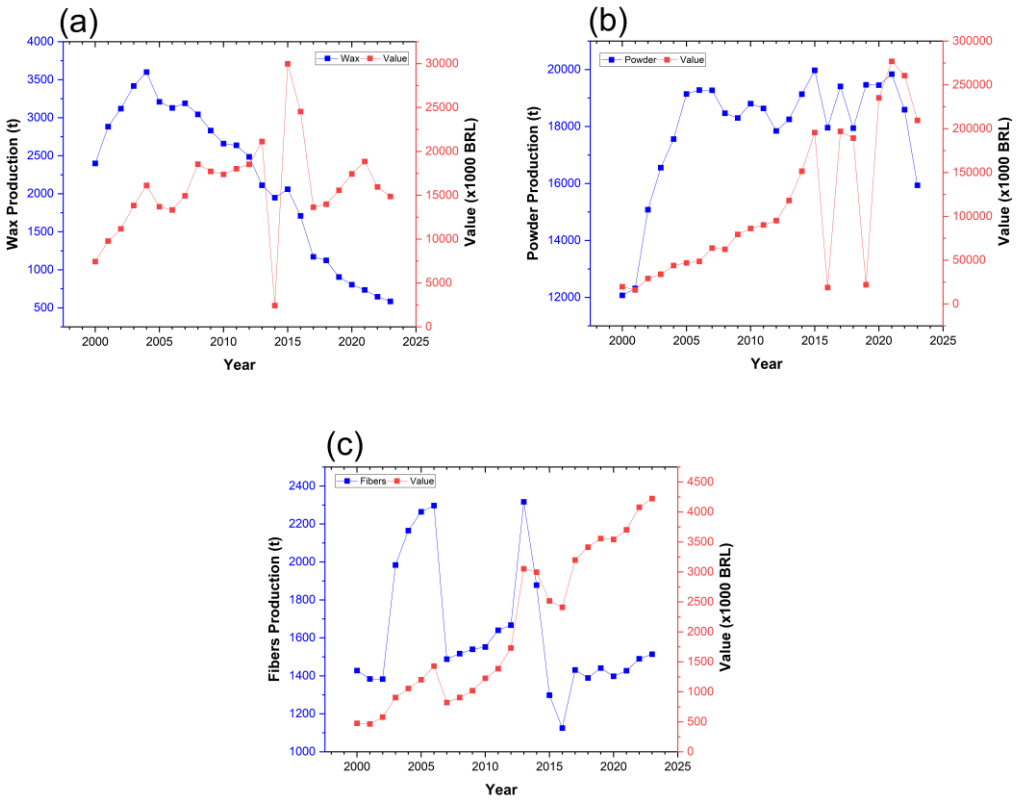

Source: Adapted data from Instituto Brasileiro de Geografia e Estatística (2023)

Carnauba wax is the most widely known product from carnauba(Junio *et al.*, 2022). Its extraction process begins with the manual harvesting of leaves, followed by drying, which may be conducted on the ground, on racks, or in solar dryers — the latter producing cleaner, higher-quality wax powder. Once dried, the leaves — hereafter referred to as carnauba straw — are processed in mechanical beaters that dislodge the powder, which is then collected, packed, and transported for further processing(Alves; Coêlho, 2008).

The main agricultural residue from this process is the dewaxed carnauba straw (Alves; Coêlho, 2008; Gonçalves *et al.*, 2023; Junio *et al.*, 2023, 2022; Silva, F. L. da, 2017). Current production data indicate a potential annual generation of approximately 170,000–290,000 tonnes of dewaxed carnauba straw(Alves; Coêlho, 2008; Instituto Brasileiro de Geografia e Estatística, 2023; Silva, F. L. da, 2017), emphasizing the relevance of this residue as a renewable and abundant lignocellulosic biomass. After wax powder extraction, carnauba straw can be used in handicrafts — such as hats, baskets, handbags, brooms, and others(Alves; Coêlho, 2008; Junio *et al.*, 2022). When not used for this purpose, the leaves become waste(Junio *et al.*, 2022).

Recent research, however, has sought to add value to this residue by exploring alternative applications. Studies have demonstrated that carnauba's straw, due to their high cellulose content, serves as excellent substrates for enzyme production and bioethanol

generation(Silva, F. L. da, 2017). Additionally, this residue has been found to be an effective mulching material, promoting plant survival and growth in degraded areas(Gonçalves *et al.*, 2023). Moreover, the fibrous nature of these leaves enables their use as reinforcement in composite materials (Junio *et al.*, 2023, 2022).

Regarding adsorption, carnauba straw powder removed Cu(II) ions with a maximum capacity of 9.5 mg/g(Ferreira Da Silva *et al.*, 2018; Pereira *et al.*, 2021). When treated with bentonite clay, its Cu(II) adsorption capacity increased to 21.98 mg/g compared to the natural powder(Pereira *et al.*, 2020). Carnauba straw has also been investigated for dye removal, achieving adsorption capacities of 0.294 mmol/g (at 25 ºC) for methylene blue and 0.399 mmol/g (at 55 ºC) for crystal violet(Goes *et al.*, 2019).

2.3 Biochar

The definition of biochar is not entirely uniform across literature. Lehmann and Joseph(Lehmann; Joseph, 2015) describe biochar as a carbon-rich material produced by heating biomass under absent or oxygen-limited conditions. Similarly, the International Biochar Initiative (IBI)(International Biochar Initiative (IBI), 2015) defines biochar as a solid material obtained from the thermochemical conversion of biomass in an oxygen-limited environment. In contrast, the European Biochar Certificate (EBC)(Schmidt *et al.*, 2024) adopts a more restrictive approach, considering pyrolysis as the conventional route for biochar production and classifying products derived from processes such as hydrothermal carbonization (HTC), torrefaction, and gasification separately.

Its elemental composition is primarily carbon, along with oxygen, nitrogen, and inorganic ash, and its physicochemical properties—such as porosity, surface area, functional groups, and surface chemistry—depend strongly on the biomass feedstock and operating parameters, including temperature, residence time, and heating rate (Qin *et al.*, 2022; Seow *et al.*, 2022).

Biochar has attracted considerable attention because its physicochemical properties enable applications in soil fertility improvement, contaminant immobilization, wastewater remediation, carbon sequestration, and energy-related technologies(Akanji *et al.*, 2023; Qin *et al.*, 2022).

2.3.1 Conversion of Biomass into Biochar

Biomass can be converted into biochar through different thermochemical routes, including pyrolysis, hydrothermal carbonization (HTC), torrefaction, gasification, and conventional carbonization under oxygen-limited conditions(Lehmann; Joseph, 2015; Qin *et al.*, 2022). However, pyrolysis remains the most widely studied and employed process for biochar production. During pyrolysis, biomass is thermally decomposed in the absence or near-absence of oxygen, resulting in the formation of three main product fractions: biochar (carbon-rich solid product), bio-oil (condensable vapors resulting in a liquid product fraction), and biogas (non-condensable gases) (Chandraratne *et al.*, 2021; Kambo; Dutta, 2015; Lehmann; Joseph, 2015).

Depending on the operating conditions — i.e., heating rate, residence time and temperature — pyrolysis processes can be classified slow, fast, flash and advanced pyrolysis. Although the exact values of these operational conditions reported in the literature vary depending on the type of biomass and experimental objectives, some general trends can be highlighted.

Slow pyrolysis is conducted over relatively long residence times (minutes to hours) and at low temperatures (300–700 °C) with slow heating rates (0.1–10 °C min^{-1}). The low heating rate limits secondary pyrolysis and thermal cracking in lignocellulosic biomass, resulting in biochar as the main product. At heating rates below 10 °C min^{-1}, chemical bonds gradually break, and the biomass structure is reorganized into a more stable matrix, inhibiting the formation of volatile compounds(Tan, H. *et al.*, 2021).

Fast pyrolysis primarily produces liquid and gaseous products (bio-oil and biogas)(Sampaio; Lima; Pires, 2025). It typically occurs at higher temperatures (600–1000 °C)(Tan, H. *et al.*, 2021), with rapid heating rates (>100 °C min^{-1})(Yaashikaa *et al.*, 2020) and short residence times (0.5–10 s)(Fahmy *et al.*, 2020). This process yields considerable quantities of bio-oil with fuel properties suitable for use in turbines, boilers, and internal combustion engines(Al-Rumaihi *et al.*, 2022).

Flash pyrolysis, which maximizes bio-oil yield (up to 75%), is conducted at temperatures approaching 1000 °C, with extremely high heating rates (>700 °C min^{-1}) and very short residence times (<0.5 s). One of the main challenges of flash pyrolysis lies in the thermal instability of its products. Furthermore, the catalytic influence of char often results in more viscous oils with solid impurities, increasing processing costs for upgrading and reducing economic feasibility(Al-Rumaihi *et al.*, 2022).

Advanced pyrolysis methods are usually modifications of conventional processes designed to improve the yield, composition, and properties of the products. Approaches include vacuum, microwave, solar, and plasma pyrolysis.

Although pyrolysis is the dominant route for biochar production, other thermochemical conversion processes have also been employed to obtain biomass-derived carbonaceous materials(Sun *et al.*, 2025; Yaashikaa *et al.*, 2020). Hydrothermal carbonization (HTC) is carried out in aqueous media under elevated temperature and pressure, producing hydrochar with physicochemical properties distinct from those of pyrolysis-derived biochars(Yaashikaa *et al.*, 2020). Torrefaction is a mild thermal treatment generally performed between 200 and 300 °C under inert or oxygen-limited conditions, yielding a solid product with enhanced fuel properties and improved hydrophobicity(Yaashikaa *et al.*, 2020). Gasification, in contrast, operates at higher temperatures and controlled amounts of oxidizing agents, primarily aiming at syngas production while generating a carbon-rich solid residue as a by-product. The characteristics of the resulting materials depend strongly on the conversion technology and operating conditions employed(Qin *et al.*, 2022; Sun *et al.*, 2025).

In addition to dedicated pyrolysis reactors, muffle furnaces operated under oxygen-limited conditions have been widely employed for laboratory-scale production of biomass-derived carbonaceous materials. Silva. et al. (2024) developed a simplified thermochemical process using a conventional muffle furnace to produce coconut shell biochars under oxygen-limited conditions and compared them with biochars obtained through slow pyrolysis in an inert-atmosphere reactor. The authors produced materials at temperatures ranging from 350 to 700 °C and residence times of 30 and 90 min. Although differences in yield and morphology were observed, both production routes generated materials with similar spectroscopic characteristics and significant adsorption capacity toward methylene blue, demonstrating that oxygen-limited carbonization in a muffle furnace can produce biochars with properties comparable to those obtained in dedicated pyrolysis systems.

Similarly, Chaudhary; Dinakaran; Rao, (2024) compared biochars produced from urban biowastes using a laboratory muffle furnace and a traditional tin kiln under equivalent thermal conditions (600 °C for 60 min). The resulting materials exhibited comparable physicochemical properties, including pH, electrical conductivity, cation exchange capacity, nutrient content, and carbon content. Furthermore, both production methods showed similar heavy-metal adsorption performance, indicating that the production method had a limited effect on the overall functionality of the biochars. Based on these findings, the authors suggested that muffle furnace

carbonization can serve as a practical and reliable alternative for laboratory-scale biochar production.

2.3.2 Properties of Biochar

The properties of biochar are highly dependent on the feedstock composition and the operational parameters of the pyrolysis process. These characteristics determine its potential applications, such as soil amendment, carbon sequestration, and pollutant adsorption. Table 1 summarizes key biochar properties, their definitions, and their significance for characterization and applications.

Table 1 - Main biochar properties and their significance for biochar characterization and applications.

Properties	Definition	Indication
Mass yield	The ratio of pyrolyzed product mass to raw biomass mass	Indication of biochar production efficiency
Density	Mass of the material divided by the volume occupied that includes interstitial space	Low density and high porosity indicate low weight per unit volume. Bulk density is important for shipping and handling of biochar.
Specific surface area (SSA)	Total surface area of a material per unit of mass.	High SSA indicates greater adsorption capacity and water holding capacity of biochar
Porosity	Ratio of the volumes of voids or pore space divided by the total volume	The porosity together with the specific surface area affect the ability of biochar as adsorbent, soil amendment and reactivity under certain conditions
Pore volume and pore size distribution	Total volume of openings and pores in biochar. The pore-size distribution is the relative abundance of each pore size.	Pore volume and pore size distribution considerably influence hydrophobicity, water holding capacity and affinity of compounds toward biochar.
Electric conductivity	How much voltage is required to get an amount of electric current to flow	It represents the ability of a material to conduct electric current
Elemental composition	Content of element C, H, N, and S	Indicator of the degree of carbonization, stability and amorphous carbon structure
	H/C mole ratio, O/C mole ratio	Low O/C and H/C mole ratios normally indicate high stability of biochar
pH-value	pH = -log [H+]	Indicator of alkalinity (or acidity) of biochar
Surface functional groups	Aromatic and heterocyclic carbons on biochar surfaces	Indicator of biochar's capacity to adsorb pollutants and contaminants in aqueous solution, activity of biochar in anaerobic digestion, performance of biochar as catalyst
Heating value/energy content	Heat generated per unit mass or per unit volume	Indicator of the upper limit of the available thermal energy produced by a complete combustion

Properties	Definition	Indication
Fixed carbon content	Content of fixed carbon after subtracting the percentages of moisture, volatile matter and ash of one biochar sample, and is determined as FC(%) = [100-(VM+Ash)]	Indicating carbonization degree of one sample and content of carbon in the sample
Volatile matter content (VM)	Volatile matters (i.e., gases) driven off from the biochar as it is heated to specified conditions (i.e., temperature and gas atmosphere)	VM reflect the labile fractions of biochar
Ash content and composition	Non-combustible residues from the inorganic or mineral components of biochar	Ash content associated with alkaline chemical species is often related to liming effects of biochar. The contents of certain inorganic elements (i.e., Ca and K) in biochar are important for potential agronomic and environmental benefits for fertilizing soil and enhancing soil quality
Cation exchange capacity (CEC)	Amount of exchangeable cations that biochar can hold	Indicator of biochar's impacts on soil fertility
Anion exchange capacity (AEC)	Amount of anions that biochar can adsorb	Indicator of biochar's effect to reduce leaching of anionic nutrients in soil
Hydrophobicity and water holding capacity	Affinity of biochar to water and capacity of biochar to contain and retain water	Indicator of biochar's ability to retain water in the soil, decrease mobility of the water and reduce water stress in plants
Stability	The proportion of initial carbon remaining after abiotic and biotic degradation	Indication of biochar's recalcitrance in certain applications (i.e., carbon sequestration) along various conditions and time scales
Surface functional group	Functional groups present at surface of biochar that increase its sorption properties include carboxylic (−COOH), hydroxyl (−OH), amine, amide and lactonic groups	Indicator of biochar's capacity to adsorb organic and heavy pollutants, catalytic performance

Source: Reproduced from Xie *et al.* (2022)

For environmental applications, particularly the removal of organic pollutants from wastewater, certain physicochemical properties play a critical role in determining the adsorption performance of biochar, including specific surface area (SSA), porosity, pore volume and pore size distribution, surface functional groups, pH, elemental composition (especially H/C and O/C ratios), and stability(Xie *et al.*, 2022).

Specific surface area (SSA) is defined as the total surface area of a material per unit of mass and is typically measured by gas physisorption (e.g., N_2 at 77 K using the Brunauer-Emmett-Teller method)(Sun *et al.*, 2025). High SSA is one of the most important indicators of biochar's adsorption capacity, as it provides a greater number of active sites for the physical retention of organic pollutants (Xie *et al.*, 2022). For neutral organic compounds, biochar with larger SSA exhibits a stronger capability to adsorb these contaminants (Xie *et al.*, 2022). Generally, increasing the pyrolysis temperature increases SSA up to a certain threshold (approximately 800–1000°C), above which pore collapse may occur(Sun *et al.*, 2025). Biochar produced at high temperatures (e.g., >500°C) tends to have a larger surface area and more micropores, making it more suitable for organic pollutant removal (Xie *et al.*, 2022). Activated biochars can achieve SSA values exceeding 1000 m^2/g, further enhancing adsorption performance(Sun *et al.*, 2025).

Porosity refers to the ratio of void volume to total volume, while pore volume is the total volume of openings and pores within biochar, and pore size distribution describes the relative abundance of each pore size class (micropores <2 nm, mesopores 2–50 nm, and macropores >50 nm)(Sun *et al.*, 2025). These properties considerably influence the affinity of organic compounds toward biochar, as pollutants can be adsorbed through physical settling and pore-filling routes, where solute molecules condense and fill the pores(Xie *et al.*, 2022). Microporosity and mesoporosity are particularly important for adsorption, as they provide high surface area and confinement effects that enhance retention. Biochar produced at high temperatures exhibits a well-developed micropore structure due to the escape of volatiles during pyrolysis(Sun *et al.*, 2025). For effective removal of organic contaminants, a combination of micropores (for high energy density) and mesopores (for fast diffusion) is often desirable(Xie *et al.*, 2022).

Surface functional groups on biochar include carboxylic (−COOH), hydroxyl (−OH), amine, amide, lactonic, carbonyl, and aromatic ring structures(Sun *et al.*, 2025). These groups are key indicators of biochar's capacity to adsorb organic pollutants from aqueous solutions(Xie *et al.*, 2022). The type and concentration of surface functional groups play a crucial role in the

adsorption mechanisms, which may involve electrostatic interactions, hydrogen bonding, π-π stacking, and complexation(Sun *et al.*, 2025; Xie *et al.*, 2022). At lower pyrolysis temperatures (300–400°C), biochar retains more oxygen-containing functional groups (e.g., carboxyl and hydroxyl), which increase hydrophilicity and cation exchange capacity(Sun *et al.*, 2025). At higher temperatures (600–700°C), biochar becomes more hydrophobic and aromatic, favoring the adsorption of nonpolar and hydrophobic organic compounds via π-π interactions(Xie *et al.*, 2022). The presence of persistent free radicals on biochar surfaces has also been reported, which may contribute to the degradation of adsorbed pollutants(Sun *et al.*, 2025).

The pH of biochar is an inherent property that generally ranges from 7.1 to 10.5 (alkaline), although values from 3.1 to 12.0 have been reported depending on feedstock and pyrolysis conditions(Xie *et al.*, 2022). Higher pyrolysis temperatures produce more alkaline biochar due to the enrichment of ash-forming alkali and alkaline earth metals (e.g., Ca, K, Mg)(Sun *et al.*, 2025). For adsorption applications, both the pH of biochar and the pH of the solution are important. The solution pH affects the surface charge of biochar and the ionization state of pollutant molecules, thereby influencing electrostatic interactions(Xie *et al.*, 2022). At higher pH values, phenolic −OH groups on biochar surfaces dissociate, creating a negative charge that can enhance electrostatic attraction to cationic species(Xie *et al.*, 2022). Conversely, for anionic pollutants, lower solution pH (acidic conditions) favors adsorption due to protonation of surface functional groups(Xie *et al.*, 2022). Experimental studies have shown that adsorption capacity for organic pollutants often reaches a maximum at an optimal pH and then drops as pH increases further, due to electrostatic repulsion(Xie *et al.*, 2022).

Regarding elemental composition, biochar is primarily composed of carbon, hydrogen, and oxygen, with smaller amounts of nitrogen and sulfur(Sun *et al.*, 2025). The molar ratios H/C and O/C are useful indicators of carbonization degree and the abundance of polar functional groups(Xie *et al.*, 2022). Low H/C and O/C ratios indicate high aromaticity and hydrophobicity, which are associated with greater stability and higher affinity for nonpolar organic compounds(Leng *et al.*, 2019; Xie *et al.*, 2022).

Biochar produced at higher temperatures has lower H/C and O/C ratios, indicating a more condensed aromatic structure and reduced polarity. Studies have shown that the adsorption capacity of biochar for neutral organic compounds decreases with increasing O/C and H/C ratios, as higher ratios correspond to more polar, less hydrophobic surfaces(Xie *et al.*, 2022). Therefore, for effective removal of organic pollutants, a balance between sufficient

functional groups (for specific interactions) and high aromaticity (for hydrophobic and π-π interactions) is often required.

Futhermore, biochar stability is defined as the proportion of initial carbon remaining after abiotic and biotic degradation and is an indication of biochar's recalcitrance under various conditions and time scales(Xie *et al.*, 2022). The carbon structure, particularly the degree of aromatic condensation, is the most decisive factor determining biochar stability(Leng *et al.*, 2019). Biochar with high aromaticity and low H/C ratio is more resistant to biological and thermochemical degradation, which is important for long-term applications(Leng *et al.*, 2019).

For adsorption purposes, stability also affects the reusability and long-term performance of biochar as an adsorbent. Aging and degradation processes (e.g., wetting-drying cycles, mild oxidation) can alter surface functional groups and porosity, potentially enhancing or reducing adsorption capacity over time (Xie *et al.*, 2022). While less stable biochars (produced at lower temperatures) may degrade faster, they initially possess more oxygen-containing functional groups that are beneficial for polar pollutant adsorption(Sun *et al.*, 2025). Thus, the choice of biochar for environmental applications must consider the trade-off between initial adsorption performance and long-term stability.

2.4 Clay and Clay Minerals

Clay is a natural fine-grained material having diameter less than 0.005 mm and is composed mainly of clay minerals formed through the weathering and alteration of rocks rich in feldspars and other primary minerals(Kumari; Mohan, 2021). These materials are characterized by their plasticity when wet and by their ability to harden when dried or fired, properties that have made clay important in natural processes and in a wide range of applications(Nunes *et al.*, 2023; Theng, 2024).

The term “clay” usually refers to the natural earthy material itself, while “clay minerals” denote the hydrated phyllosilicates that give clay its distinctive properties, such as plasticity and cohesion(Theng, 2024). Clays are usually composed of one or more clay minerals and can also include trace amounts of quartz (SiO_2), metal oxides (Al_2O_3, MgO, etc.), and organic matter(Kumari; Mohan, 2021).

2.4.1 Structure of Clay minerals

Clay minerals are typically phyllosilicates formed by sheets of silicon tetrahedra (Si^{4+} surrounded by four oxygen atoms, Figure 6a) and aluminum or magnesium octahedra (Al^{3+} or

Mg^{2+} coordinated to six hydroxyls, Figure 6b) arranged in layered structures(Kumari; Mohan, 2021; Theng, 2024).

Figure 6 - Clays mineral structure

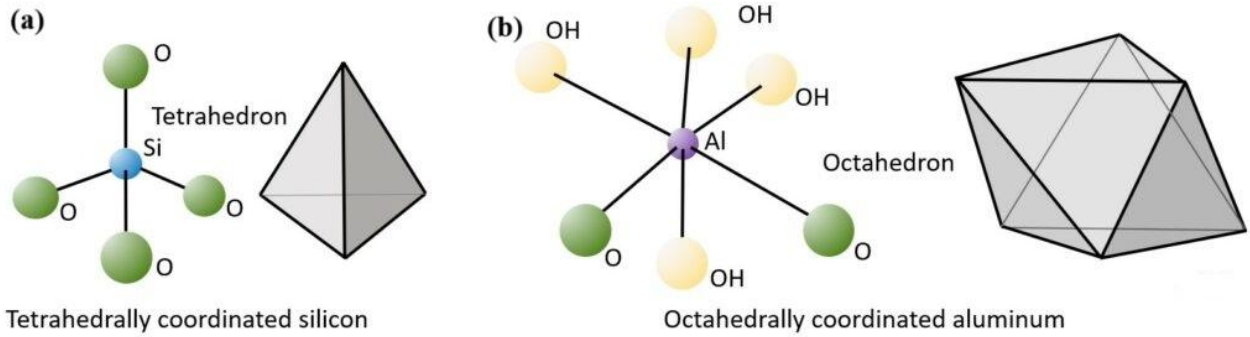

Source: Adapted from Earle (*S.d.*])

The combination of one tetrahedral (T) sheet with one octahedral (O) sheet gives rise to the 1:1 or T–O layer type (Figure 7a). Likewise, the stacking of two tetrahedral sheets with an intermediate octahedral sheet, in which the tetrahedral sheets point inward, forms the 2:1 or T–O–T layer type (Figure 7b)(Kumari; Mohan, 2021; Theng, 2024).

Figure 7 - Layer types of clay minerals

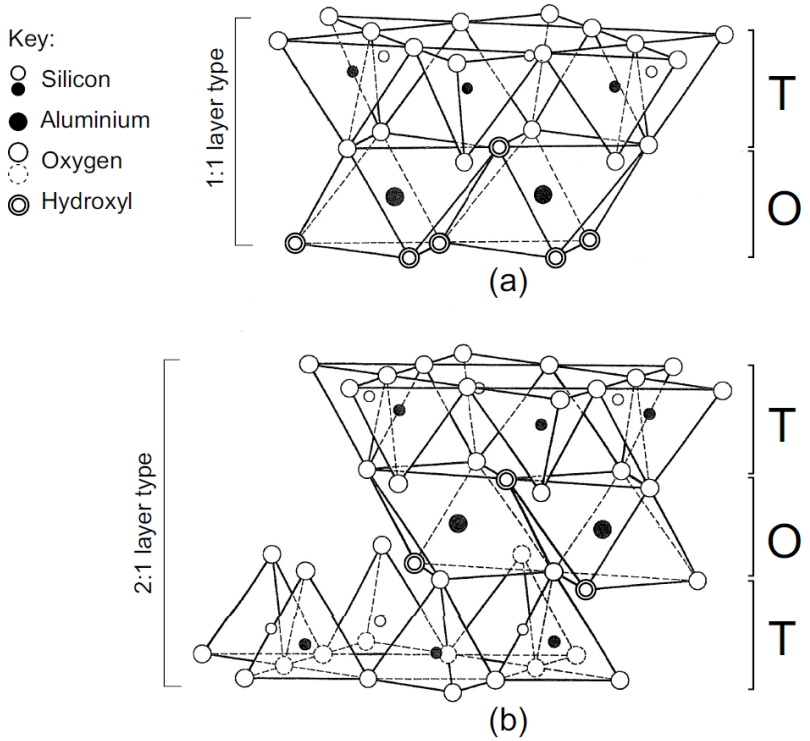

Source: Reproduced from Theng (2024)

Clay minerals can be grouped according to their layer type, which defines their structural arrangement and properties(Kumari; Mohan, 2021; Theng, 2024). Table 2 presents the principal

groups of clay minerals, their typical layer thickness, interlayer materials, and representative species.

Table 2 - Classification of Clay Minerals

Layer type	Group	Layer thickness (nm)	Interlayer materials	Representative species
1:1	Kaolinite	~0.7	None	Kaolinite, dickite, nacrite, lizardite
2:1	Serpentine	0.7-1.0	None	Halloysite, chrysotile
2:1	Talc and Pyrophyllite	~0.9	None	Talc, pyrophyllite
2:1	Smectite	≥0.96	Hydrated exchangeable cations; variable water	Montmorillonite, beidellite, nontronite, saponite, hectorite, sauconite
2:1	Vermiculite	≥0.94	Hydrated exchangeable cations; variable water	Dioctahedral and trioctahedral vermiculite
2:1	Mica	True: 0.85-1.0	K^+; Variable water	Muscovite, celadonite
		Brittle: 0.85-2.0	K^+ or Ca^+	Biotite, phlogopite, margarite
		Interlayer deficient: 0.6-0.85	K^+; variable water	Illite
2:1	Chlorite	1.4	O-H sheet	Donbassite, sudoite, chamosite
2:1 modulated	Sepiolite	1.34	Ca^+ and $4H_2O$	Sepiolite
2:1 modulated	Palygorskite	1.29	Ca^+ and $2H_2O$	Palygorskite

Source: Adapted from Kumari; Mohan (2021); Theng (2024)

2.4.2 Bentonite clay

Bentonite is a natural clay belonging to the smectite group and composed predominantly of montmorillonite, a 2:1 phyllosilicate in which an alumino-octahedral sheet is sandwiched between two silica tetrahedral sheets(Kumari; Mohan, 2021; Marouf et al., 2021; Pourhakkak et al., 2021). This mineral originates mainly from the alteration of volcanic ash in fresh or marine environments millions of years ago, a process that produces large deposits worldwide. It was first described in 1890 in Wyoming, near Fort Benton, which gave rise to its name.

Significant reserves are currently found in the United States, Europe, North Africa, Japan, China, and Algeria (Kumari; Mohan, 2021; Marouf et al., 2021).

The structural unit of montmorillonite consists of a gibbsite-like octahedral layer placed between two tetrahedral silica layers (Figure 8)(Marouf *et al.*, 2021; Pourhakkak *et al.*, 2021). Isomorphic substitutions within the octahedral sheet (e.g., Mg^{2+} or Fe^{2+} replacing Al^{3+}) and, to a lesser extent, within the tetrahedral sheet (Al^{3+} replacing Si^{4+}) generate a permanent negative surface charge. This imbalance is compensated by hydrated exchangeable cations (Na^{+}, Ca^{2+}, K^{+}, Mg^{2+}) in the interlayer space, which gives bentonite its characteristic swelling behavior, high cation exchange capacity (CEC), and strong adsorption ability (Kumari; Mohan, 2021; Marouf et al., 2021; Pourhakkak et al., 2021).

Figure 8 - Montmorillonite structure

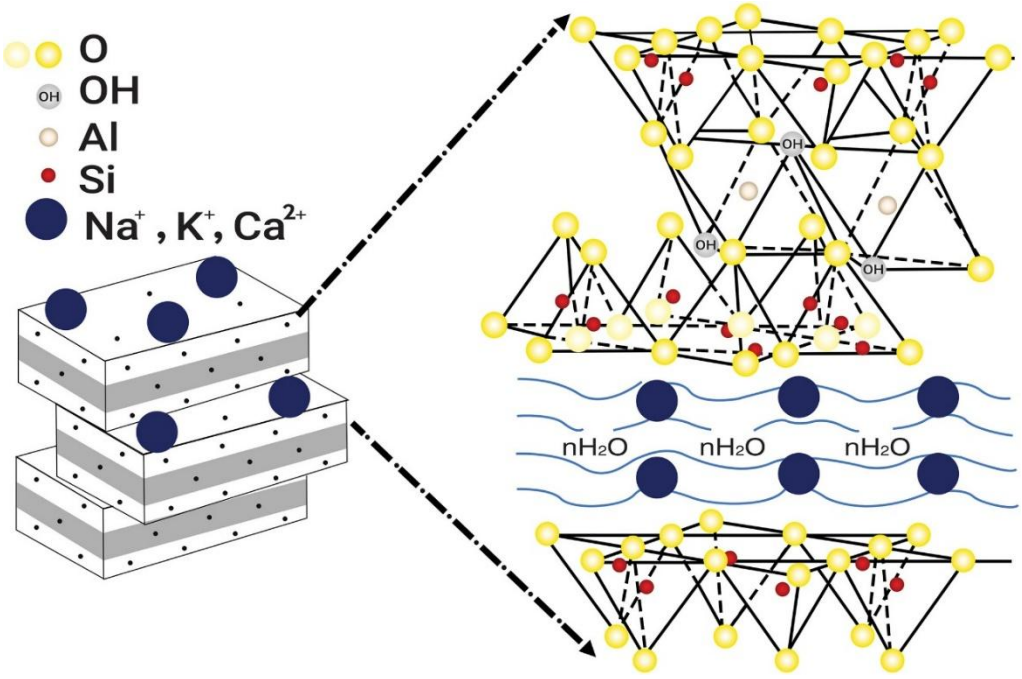

Source: Reproduced from Pourhakkak *et al.* (2021)

Bentonite is classified according to the dominant exchangeable cation. Sodium bentonite exhibits exceptional swelling and colloidal properties, making it suitable for drilling fluids and sealing barriers. Calcium bentonite is an efficient adsorbent for oils and impurities and forms the basis of fuller's earth; it can be converted into sodium bentonite through ion exchange (sodium activation). Potassium bentonite (or K-bentonite) is potassium-rich and associated with illitic compositions derived from volcanic ash (Kumari; Mohan, 2021; Marouf et al., 2021).

2.5 High Energy Ball Milling (HEBM)

Milling is a unit operation widely used in different industrial processes involving solid materials. Its main purposes are to reduce particle size and/or to increase the specific surface area of the material, which can improve reactivity and performance in subsequent applications. Milling also induces changes in the microstructure of particles, such as lattice distortions, crystal deformations, and refinement, which are essential for producing materials with tailored structural and textural properties(Leonel *et al.*, 2014).

High-energy ball milling (HEBM) is particularly important in the preparation of nanostructured materials and solid-state reactions. The technique relies on the continuous impact and friction of milling balls, which generate mechanical energy sufficient to break chemical bonds, deform crystalline lattices, and create defects in the material. These processes lead to a significant reduction in particle size, often reaching the nanoscale, and promote surface activation that can be exploited in the functionalization of biochar and other carbonaceous solids (Kumar *et al.*, 2020).

Several parameters determine the efficiency and outcome of HEBM, including milling time, rotation speed, ball-to-sample mass ratio, temperature, number and diameter of balls, and the volume of the container . The interaction between these factors influences the energy transferred to the particles and, consequently, the extent of structural modification(Kumar *et al.*, 2020; Leonel *et al.*, 2014).

In planetary ball mills(Figure 9a), which are the most used devices at the laboratory scale, both rotational and translational motions occur simultaneously. The support rotates in one direction while the jars rotate in the opposite direction, subjecting the balls to complex centripetal forces (Figure 9b). These dynamics result in multiple types of energy dissipation, including ball–ball collisions, ball–wall impacts, ball–ball friction, and compression effects, which together enhance the efficiency of milling (Kumar *et al.*, 2020; Leonel *et al.*, 2014).

Figure 9 - HEBM. a)Planetary ball mill b) Milling dynamics

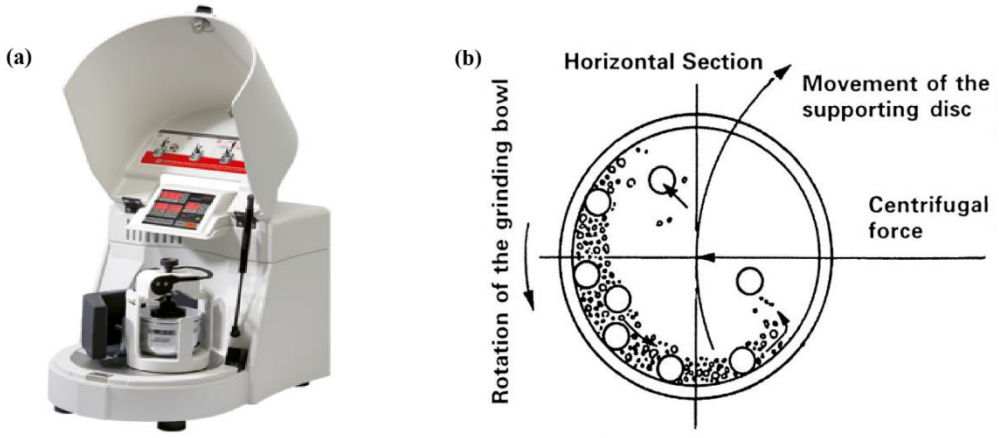

Source: Adapted from Suryanarayana (2007)

Previous work has revealed significant structural modifications in biochar due to HEBM. Lopez-Tenllado; Motta; Hill (2021) investigated multiple biochar samples and found that this mechanical treatment increases pore volume and acidity, improving methylene blue adsorption. Microporosity developed through the exposure of occluded pores, while surface oxygen groups were increasingly exposed, with acidity proportional to the original oxygen content of the biochar. These changes were to energy input, with energy inputs above 25 kJ/g not resulting in further porosity development, and surface acidity continuing to develop up to 60–90 kJ/g.

Complementarily, Ng et al. (2022) applied high-energy milling to oil palm empty fruit bunch (OPEFB) biochar, producing nanobiochar (NBC) with an average particle size of approximately 100 nm after 60 minutes. The NBC exhibited an irregular, polygonal morphology distinct from the initial fibrous structure, high thermal stability, and only minor changes in crystalline dimensions. Prolonged milling, however, led to particle agglomeration due to mechanical compaction and hydrogen bond formation.

Similarly, high-energy ball milling has been applied to clays. Kovalchuk et al. (2023) showed that mechanochemical activation of montmorillonite partially amorphized the crystalline structure, reduces particle size from ~6.6 nm to 4.3 nm after 1 hour, and transforms the morphology from plate-like to more spherical and quasi-regular particles. These changes increase the specific surface area from 89.1 to 146.8 m^2/g and create new reactive sites, improving adsorption capacity for ions such as cesium, strontium, and uranium. Dellisanti; Valdré (2005) further reported that prolonged milling reduces crystallite size and progressively

destabilizes the structure, while potentially causing particle aggregation. Careful control of milling duration is therefore essential to maximize surface area and preserve particle dispersion.

2.6 Characterization Techniques of Biochar and Biochar-Clay Composites

Detailed characterization of biochar and its composites with clays is fundamental to understanding their physical, chemical, and structural properties, which directly influence their performance in environmental applications, such as pollutant adsorption. Modern analytical techniques allow for the investigation of these materials, from their morphology and elemental composition to their thermal stability and surface functionality(Akanji *et al.*, 2023; Igalavithana *et al.*, 2017; Yaashikaa *et al.*, 2020).

2.6.1 Proximate and Elemental Analysis

Proximate analysis quantifies moisture, volatiles, fixed carbon, and ash (mineral content), following standards such as ASTM D1762-84(Igalavithana *et al.*, 2017). For composites, a drastic increase in ash content is a clear indicator of the incorporated mineral load(Akanji *et al.*, 2023; Igalavithana *et al.*, 2017). Elemental analysis (CHNS) quantifies the percentages of carbon, hydrogen, nitrogen, and sulfur. Calculations of atomic ratios (O/C, H/C) are valuable proxies for the degree of aromaticity and surface polarity of the material, parameters that are significantly altered by the introduction of clay(Akanji *et al.*, 2023; Amin *et al.*, 2016; Igalavithana *et al.*, 2017).

2.6.2 Fourier Transform Infrared Spectroscopy (FTIR)

FTIR is the primary technique for identifying surface functional groups, which are active sites for adsorption. Modification with clays introduces unmistakable vibration bands for Si-O-Si, Si-O, and Al-O bonds. Simultaneously, it alters the intensity and position of intrinsic biochar bands (C=O, C=C, C-O). The increase in oxygenated groups is particularly important, as it facilitates adsorption mechanisms such as electrostatic interactions, hydrogen bonding, and ion exchange(Akanji *et al.*, 2023; Amalina *et al.*, 2022; Arif *et al.*, 2021; Yaashikaa *et al.*, 2020).

2.6.3 Scanning Electron Microscopy with Energy-Dispersive X-ray Spectroscopy (SEM-EDS)

SEM is indispensable for the direct observation of morphological changes. Images of composites reveal the distribution of clay particles over the porous surface of the biochar, increasing roughness and creating new active sites (Akanji *et al.*, 2023; Arif *et al.*, 2021).

Semiquantitative analysis by EDS (Energy-Dispersive X-ray Spectroscopy) confirms the presence and homogeneous dispersion of characteristic clay elements (Si, Al, Mg, Fe, Ca), chemically validating the modification observed microscopically(Akanji *et al.*, 2023; Amalina *et al.*, 2022; Arif *et al.*, 2021).

2.6.4 Surface Area and Porosity Analysis (BET)

The specific surface area, pore volume, and pore size distribution are primarily determined by gas physisorption. N_2 adsorption (77 K) is ideal for meso- and macropores, while CO_2 adsorption (273 K) is more sensitive for characterizing micropores(Igalavithana *et al.*, 2017). Modification with clays can significantly increase the biochar's surface area due to the precipitation of mineral particles, although it may also lead to partial pore blockage, reducing the average pore diameter (Akanji *et al.*, 2023; Arif *et al.*, 2021).

2.6.5 X-Ray Diffraction (XRD)

XRD is a fundamental technique for structural and phase analysis, identifying the mineralogical composition and crystallinity of the material. In composites, successful impregnation is confirmed by the emergence of characteristic peaks of clay minerals (e.g., montmorillonite at ~6.5°; quartz at ~28.8°) that are absent in pristine biochar. The diffraction pattern also reveals the carbonaceous structure, with typical peaks for graphite (~24°) and amorphous carbon (~43°)(Akanji *et al.*, 2023; Arif *et al.*, 2021).

2.7 Adsorption

Adsorption is a mass transfer process in which molecules from a fluid phase (liquid or gas) accumulate on the surface of a solid material, called the adsorbent, while the retained species is referred to as the adsorbate. This phenomenon occurs due to unsaturated surface forces on the adsorbent, which interact with the adsorbate through van der Waals and electrostatic interactions (physisorption), or through stronger covalent bonding (chemisorption). The efficiency of adsorption is strongly related to the surface area and porosity of the adsorbent, since a larger external surface provides more active sites for interaction (Nascimento *et al.*, 2020; Noble; Terry, 2004).

The adsorption process may occur via different mechanisms. Steric effects are observed when the pore dimensions of the adsorbent selectively allow the entry of certain molecules, excluding others. In equilibrium-driven adsorption, the selectivity arises from the greater

affinity of the adsorbent surface for specific compounds. In aqueous systems, solution pH plays a crucial role by controlling both the chemical speciation of adsorbates (e.g., protonation or deprotonation of organic molecules, hydrolysis of metal cations) and the surface charge of the adsorbent, thereby influencing electrostatic interactions(Da Silva Neto et al., 2023; Nascimento et al., 2020; Wang; Guo, 2020).

Adsorption has become one of the most widely applied separation and treatment techniques, particularly in water and wastewater purification. Compared to conventional separation methods, adsorption offers several advantages, including high efficiency, simple operation, applicability in dilute systems, and low energy requirements. However, challenges such as the regeneration and reusability of adsorbents remain, since desorption steps may lead to partial loss of sorbent mass and adsorption capacity over repeated cycles(Noble; Terry, 2004; Wang; Guo, 2020).

2.7.1 Adsorption isotherms

The study of adsorption equilibrium is essential to understand the mechanisms involved in adsorption processes and to obtain parameters relevant for the design of separation systems. When an adsorbent encounters a solution containing an adsorbate, the adsorption proceeds until equilibrium is reached, that is, when the concentration of solute in the liquid phase remains constant and the adsorption capacity of the solid is determined(Abin-Bazaine *et al.*, 2022; Nascimento *et al.*, 2020).

At this stage, the amount of adsorbate retained on the solid surface corresponds to the amount removed from the solution, and the adsorption capacity (q_e) can be calculated through a mass balance (Equation 1)(Nascimento *et al.*, 2020).

$$q_e = \frac{(C_o - C_e)V}{m} \quad (1)$$

Where:

- C_o is the initial concentration of adsorbate (mg L^{-1});
- C_e is the equilibrium concentration of adsorbate (mg L^{-1});
- V is the volume of solution (L);
- m is the adsorbent mass (g), and
- q_e is the adsorption capacity (mg g^{-1}).

The removal efficiency (η, (%)) can be calculated using Eq. (2)(WANG, et al., 2023):

$$\eta(\%) = \frac{(C_o - C_e)}{C_o} \times 100\% \quad (2)$$

Adsorption isotherms are equations that describe the relationship between the amount of solute adsorbed by the adsorbent and its equilibrium concentration in the liquid phase(Abin-Bazaine *et al.*, 2022). A variety of theoretical and empirical isotherm models have been proposed to correlate equilibrium data, including Henry, Langmuir, Freundlich, Temkin, Dubinin–Radushkevich, Redlich–Peterson, Sips, and others(Abin-Bazaine *et al.*, 2022; Nascimento *et al.*, 2020).

However, the most applied models are the Langmuir and Freundlich isotherms, due to their simplicity and ability to adequately describe experimental adsorption data. The Langmuir model provides the maximum adsorption capacity of the material, while the Freundlich model accounts for the heterogeneity of adsorption sites(Nascimento *et al.*, 2020).

2.7.1.1 Langmuir isotherm model

The Langmuir isotherm is one of the most widely used models to describe adsorption processes. It is based on several assumptions: a fixed number of adsorption sites are available on the adsorbent surface; all sites have equal energy; adsorbed molecules do not interact with each other; and adsorption occurs in a monolayer, where each site can hold only one adsorbate molecule(Nascimento *et al.*, 2020). According to this model, the maximum adsorption corresponds to complete coverage of the surface with a single layer of adsorbate molecules, and the adsorption energy remains constant across all sites (Abin-Bazaine *et al.*, 2022).

The Langmuir isotherm is expressed in Equation 3(Nascimento *et al.*, 2020; Shakya; Vithanage; Agarwal, 2022):

$$q_e = \frac{q_m K_L C_e}{[1 + K_L C_e]} \quad (3)$$

Where:

- q_e is the adsorption capacity at equilibrium ($mg\ g^{-1}$);
- q_m is the maximum adsorption capacity corresponding to complete monolayer coverage ($mg\ g^{-1}$);
- K_L is the Langmuir constant related to the affinity between adsorbate and adsorbent ($L\ mg^{-1}$), and
- C_e is the equilibrium concentration of the adsorbate in solution ($mg\ L^{-1}$).

A characteristic feature of the Langmuir isotherm is the dimensionless separation factor, R_L(Equation 4), which indicates the favorability of adsorption (Nascimento *et al.*, 2020; Shakya; Vithanage; Agarwal, 2022)::

$$R_L = \frac{1}{[1 + K_L C_o]} \quad (4)$$

Where C_i is the initial adsorbate concentration The value of R_L indicates the type of adsorption: $R_L > 1$ is unfavorable, $R_L = 1$ is linear, $0 < R_L < 1$ is favorable, and $R_L = 0$ corresponds to irreversible adsorption(Abin-Bazaine *et al.*, 2022; Nascimento *et al.*, 2020).

2.7.1.2 Freundlich isotherm model

The Freundlich isotherm is an empirical model commonly used to describe adsorption on heterogeneous surfaces and systems with multilayer adsorption(Nascimento *et al.*, 2020). Unlike the Langmuir model, the Freundlich model does not assume a uniform adsorption energy or a monolayer coverage. Instead, it considers an exponential distribution of adsorption sites with different energies, reflecting the heterogeneity of the adsorbent surface(Abin-Bazaine *et al.*, 2022; Nascimento *et al.*, 2020).

The Freundlich equation is expressed in Equation 5(Nascimento *et al.*, 2020; Shakya; Vithanage; Agarwal, 2022):

$$q_e = K_F C_e^{\frac{1}{n}} \quad (5)$$

Where:

- K_F is Freundlich's constant in (mg g^{-1}), and
- n is Freundlich's dimensionless exponent related to the intensity of the adsorption.

Where the slope $\frac{1}{n}$ and intercept $log\ K_F$ can be determined by linear regression of experimental data. If $0 < \frac{1}{n} < 1$ the adsorption is favorable, with smaller values of $\frac{1}{n}$ corresponding to stronger interactions between adsorbate and adsorbent, whereas $\frac{1}{n} = 1$ represents linear adsorption and equivalent site energies(Abin-Bazaine *et al.*, 2022; Nascimento *et al.*, 2020).

It is important to note that the Freundlich model does not predict a maximum adsorption capacity, and adsorption may theoretically continue to increase with increasing C_e. Therefore, this model is best applied within a moderate concentration range and may not accurately describe adsorption at extremely high concentrations(Nascimento *et al.*, 2020). Despite this

limitation, the Freundlich model is widely used due to its simplicity and ability to describe non-ideal adsorption on heterogeneous surfaces(Abin-Bazaine *et al.*, 2022; Nascimento *et al.*, 2020).

2.7.2 Adsorption kinetics

The adsorption kinetics describes the rate of solute removal as a function of contact time and is directly related to mass transfer and diffusion phenomena. This process generally involves three steps (Figure 10): (i) external diffusion, where the adsorbate diffuses across the liquid film surrounding the adsorbent; (ii) intraparticle diffusion, where the adsorbate migrates into the pores of the adsorbent; and (iii) final binding of the adsorbate to active sites on the adsorbent surface (Nascimento et al., 2020; Wang; Guo, 2020).

Figure 10 - Steps of adsorption phenomena

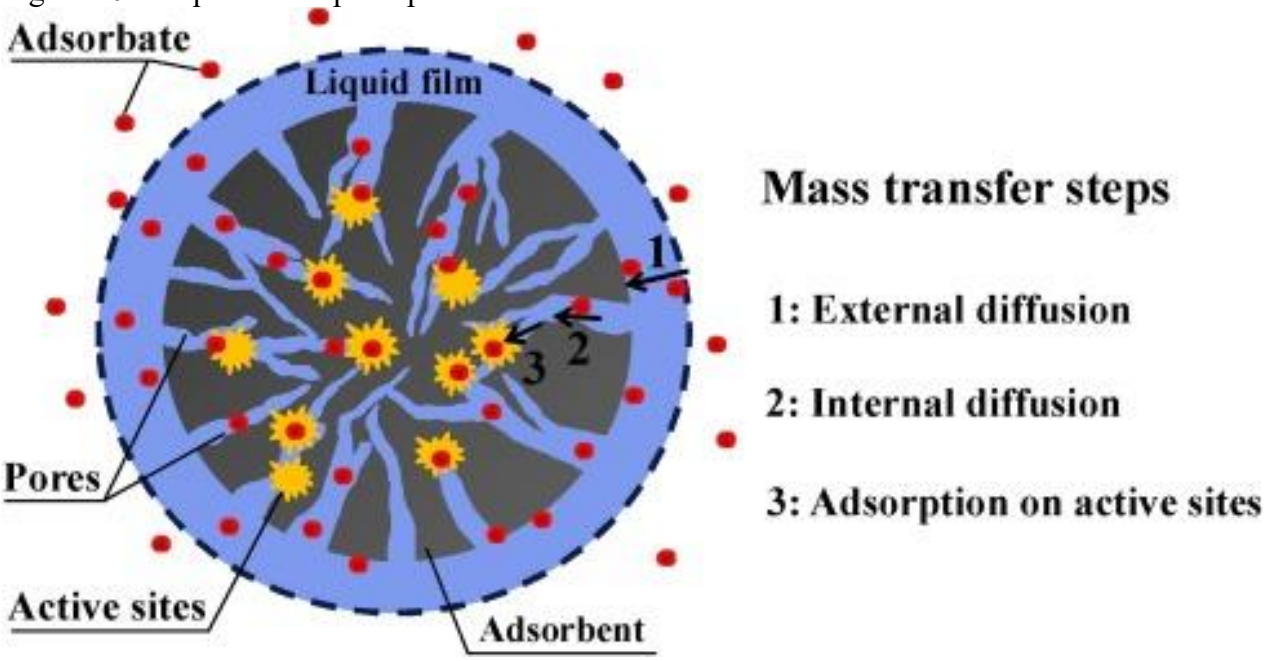

Source: Reproduced from Wang; Guo (2020)

Several factors, including initial concentration, agitation speed, particle size, pH, ionic strength, and temperature, strongly influence the adsorption rate, with intraparticle diffusion often regarded as the rate-limiting step, especially in microporous materials(Nascimento et al., 2020; Wang; Guo, 2020).

From a mechanistic perspective, adsorption kinetics is a complex process that may be controlled by diffusion or by chemically activated interactions. To interpret this behavior, different kinetic models have been proposed, such as the pseudo-first order (PFO) model, the pseudo-second order (PSO) model, Elovich, Avrami, Weber–Morris, Ritchie, and other mass

transfer models. Among these, PFO and PSO are the most widely applied, since they satisfactorily fit a large variety of experimental datasets and allow the estimation of kinetic parameters associated with adsorption.(Bujdák, 2020; Nascimento *et al.*, 2020).

While both PFO and PSO models are applied across diverse adsorption systems (e.g., biomass or nanomaterials for removing heavy metals or pharmaceuticals), the PSO model is generally perceived as superior because it accurately fits most kinetic datasets(Revellame *et al.*, 2020).

2.7.2.1 Pseudo-First Order (PSO) model

PFO model was first proposed by Lagergren in 1898, and it is given in Equation 6 (Bujdák, 2020; Nascimento et al., 2020; Wang; Guo, 2020):

$$q_t = q_e(1 - exp(-k_1 t)) \quad (6)$$

Where k_1 is the PFO rate constant (min^{-1}), and q_e and q_t are the amounts of adsorbate adsorbed per gram of adsorbent ($\mathrm{mg\,g^{-1}}$) at equilibrium and at time t, respectively(Nascimento, et al., 2020; Wang; Guo, 2020).

2.7.2.2 Pseudo-Second Order model

PSO model is expressed in Equation 7(Nascimento et al., 2020; Shakya; Vithanage; Agarwal, 2022; Wang; Guo, 2020):

$$q_t = \frac{q_e^2 k_2 t}{1 + q_e k_2 t} \quad (7)$$

Where k_2 is the PSO rate constant ($g\ mg^{-1}\ min^{-1}$).

2.7.2.3 Elovich model

The Elovich model (Equation 8), originally developed for gas–solid chemisorption kinetics, has also been successfully applied to describe adsorption processes in liquid-phase systems(Nascimento et al., 2020; Shakya; Vithanage; Agarwal, 2022; Wang, Guo, 2020):

$$q_t = \frac{1}{\beta} ln(1 + \alpha\beta t) \quad (8)$$

Where α is the initial sorption rate in ($\mathrm{mg\,g^{-1}h^{-1}}$) and β is the desorption constant in ($\mathrm{g\,mg^{-1}}$).

2.7.2.4 Intraparticle Diffusion Model (Weber-Morris model)

The intraparticle diffusion model proposed by Weber and Morris was evaluated using Eq. (9):

$$q_t = k_p t^{1/2} + C \qquad (9)$$

where k_p is the intraparticle diffusion constant in (mg $g^{-1}h^{-10.5}$) and C is the boundary layer thickness.

2.7.3 Methylene Blue as a model adsorbate

Methylene blue (MB) is a synthetic cationic dye extensively used in various industrial and biomedical applications. Chemically identified as $C_{16}H_{18}N_3ClS$ (Figure 11), MB has a molecular weight of 319.85 g/mol, is highly soluble in water, and exhibits a characteristic maximum absorbance at approximately 664 nm(Khan *et al.*, 2022). Its aromatic planar structure facilitates π–π interactions with adsorbent surfaces, while the positive charge enhances electrostatic affinity toward negatively charged materials(Oladoye *et al.*, 2022).

Figure 11 – Methylene blue chemical structure

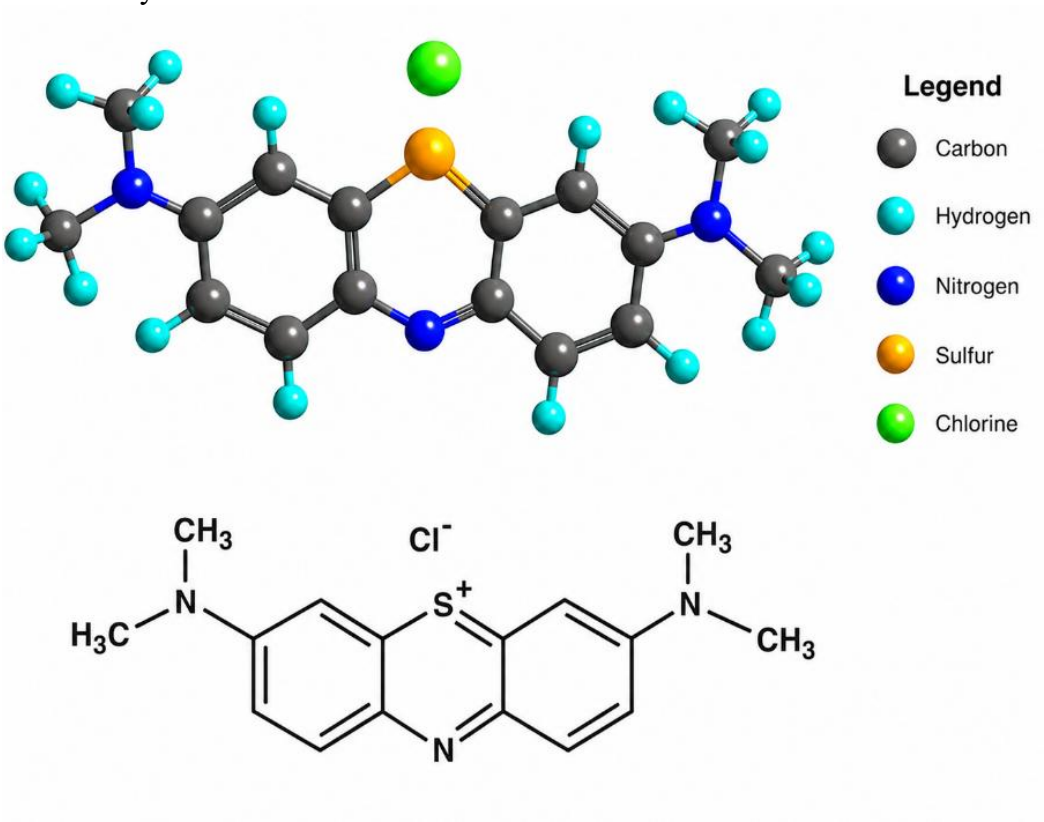

Source: Adapted From Methylene…(2011)

Industrially, MB is widely employed in the textile sector for dyeing cotton, wool, and silk, as well as in paper, leather, cosmetic, and food industries(Oladoye *et al.*, 2022). Beyond its industrial role, MB also presents biomedical relevance, historically used as an antimalarial drug, in the treatment of methemoglobinemia, vasoplegia, and more recently in photodynamic therapy for cancer(Khan *et al.*, 2022). Despite its beneficial applications, MB is

environmentally persistent and poorly biodegradable, posing serious ecological and health risks when released into aquatic ecosystems(Oladoye *et al.*, 2022). In humans, excessive exposure has been associated with respiratory distress, gastrointestinal irritation, cardiovascular effects, and reproductive toxicity(Khan *et al.*, 2022; Oladoye *et al.*, 2022).

Due to its structural representativeness of other aromatic cationic dyes, ease of spectrophotometric detection, aqueous solubility, and abundance of data in the literature, MB is commonly employed as a model adsorbate for evaluating adsorption efficiency of different materials (Khan *et al.*, 2022; Oladoye *et al.*, 2022), some examples are summarized in Table 3.

Table 3 - Examples of methylene blue adsorption by different materials

Adsorbent	q_m (mg g^{-1})	Reference
Rape Straw Biochar	148.94	(Mandzhieva *et al.*, 2022)
Rice Husk Biochar	17.97	(Ahmad, A. *et al.*, 2020)
Sugarcane Bagasse Biochar	4.45	(Cai *et al.*, 2025)
Date Palm Frond Biochar	206.61	(Zubair *et al.*, 2020)
Ryegrass Straw Biochar	28.7	(da Silva, E. O. *et al.*, 2020)
Ryegrass Straw Biochar (treated with HCl)	67.19	(da Silva, E. O. *et al.*, 2020)
Pequi Almonds Biochar	500.00	(Melo *et al.*, 2023)
Bentonite	291.00	(Daou *et al.*, 2024)
Bentonite (Activated with NaOH)	22.13	(Hamad *et al.*, 2024)

Source: Author

2.8 Biochar-Clay Composites

Biochar-Clay composites (BCC) have recently gained attention as multifunctional materials that combine the advantages of both clay minerals and biochar for environmental and agricultural applications. The combination is motivated by the need to overcome certain limitations of pristine biochar, such as low surface area, variable adsorption capacity, and potential negative impacts on soil ecology. By integrating clays, which are naturally abundant aluminosilicates with high surface area, cation exchange capacity, and structural versatility, the resulting composites exhibit enhanced physicochemical properties and improved adsorption performance(Akanji *et al.*, 2023).

From an environmental perspective, BCC has demonstrated effectiveness in the removal of heavy metals, dyes, and organic pollutants due to synergistic mechanisms such as electrostatic interactions, hydrogen bonding, cation exchange, and electron donor–acceptor (EDA) interactions(Akanji *et al.*, 2023; Arif *et al.*, 2021). Moreover, their agricultural relevance is notable, as they improve soil fertility, increase nutrient retention, and contribute to carbon sequestration(Wang, L. *et al.*, 2022).

Clay minerals most employed in BCC include montmorillonite, attapulgite, bentonite, and illite, each contributing specific structural and surface functionalities. Montmorillonite, for example, provides interlayer cation exchange capacity, allowing immobilization of toxic metals such as Cu, Zn, Pb, and As(Wang, L. *et al.*, 2022). Attapulgite, with its fibrous structure and abundant hydroxyl groups, has been shown to improve the adsorption capacity of biochar while stabilizing its morphology and thermal stability(Lin *et al.*, 2023). Bentonite-modified biochar, on the other hand, have proven effective in water treatment by enhancing porosity, surface charge, and pollutant binding(Arif *et al.*, 2021).

The synthesis of BCC can be broadly classified into pre-treatment and post-treatment methods (Figure 12). In the pre-treatment route, biomass feedstock is impregnated with clay suspensions prior to pyrolysis, ensuring the mineral particles are well integrated into the resulting carbon matrix. In contrast, post-treatment involves impregnation of pre-formed biochar with clay suspensions or solutions, often followed by drying and thermal treatment, to coat the surface and pores of the biochar with mineral phases(Akanji *et al.*, 2023; Arif *et al.*, 2021).

Figure 12 - Synthesis of Biochar-Clay Composites

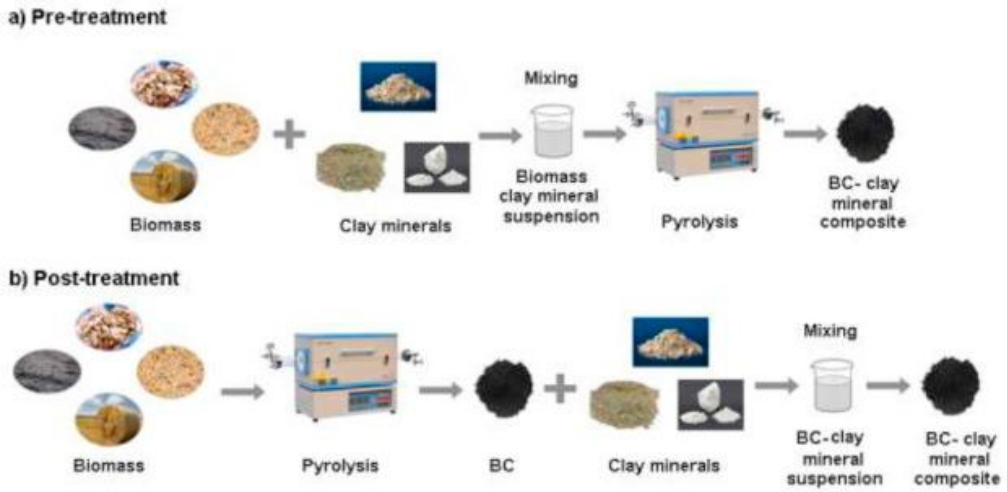

Source: Reproduced from (Arif *et al.*, 2021)

The properties of BCC depend on parameters such as the biochar/clay ratio, pyrolysis temperature, and feedstock type, which govern porosity, surface chemistry, and pollutant affinity. A summary of synthesis conditions of BCC with different feedstocks is presented in Table 4.

Table 4 - Synthesis conditions of biochar-clay composites with different feedstocks

Type of composite	Clay	Biomass	Ratio of clay to biomass	Carbonization temperature (°C)	Carbonization time (min)	Ratio of clay to liquid
Bentonite–biochar composite	Bentonite	Cassava peel, Alternanthera philoxeroides, Sweet sorghum bagasse, Prosopis juliflora	1:2, 1:5, 1:5, –	500, 300, 400, 400–500	60, 120, –, –	25 g: 500 ml, 2 g: 500 ml, –, –
Montmorillonite and red earth–biochar composite	Montmorillonite and red earth	Cotton woods, Municipal waste	1:5, 1:5	500, 500	30, 30	50 g: 2000 ml, 50 g: 2000 ml
Biochar–montmorillonite composites	Montmorillonite	Peanut shell, Cauliflower leaves, Bamboo powder	–, –, 1:1	250, 500, 300–500	120, 360, 60	30 g: 600 ml, –, –
Iron–clay–biochar composite	Kaolinite and bentonite	Bamboo	–	250, 350, 450, 550	30	–
Attapulgite–clay–biochar composite	Attapulgite	Bagasse, Potato stem, Macadamia nutshells/groundnut shells, Cauliflower leaves	1:5, 1:5, –, 1:5	700, 500, 365–700, 500	240, 360, 30, 360	4 g: 50 ml, 2 g: 80 ml, 30 g: 120 ml, 4 g: 200 ml
Silica/zeolite–biochar composite	Silica or zeolite	Date palm waste	–	600	180	4 g: 1000 ml
Biochar–chitosan/clay nanocomposite	Montmorillonite clay	Residual bark chips	–	600	120	–
Montmorillonite/kaolinite–biochar composites	Montmorillonite and kaolinite	Oak leaves; Bamboo, bagasse and hickory chips	–, 1:5	600, 600	60, 60	–, 2 g: 500 ml

Source: Adapted from Akanji *et al.*(2023)

3 METODOLOGY

3.1 Biochar and BCC preparation

3.1.1 Biomasses harvest and physical preparation

Carnauba palms were collected from naturally occurring trees at a specific location near (3.7431° S, 38.5788° W; WGS 84) on Pici Campus of the Federal University of Ceará, located in Fortaleza, State of Ceará, Brazil (SISGEN registration no. A2B4F8E).

The carnauba leaves were harvested, sun dried and then the straw (Figure 13) were separated from the stalks. A portion of the straw was set aside for wax extraction — to obtain dewaxed straw — while the remaining leaves were ground and sieved through an 18-mesh screen.

Figure 13 – Carnauba straw

Source: Author

Wax extraction was performed by rubbing a synthetic sponge over the leaf surface to remove the wax layer. The material was subsequently shredded and sieved using an 18-mesh screen to obtain a uniform particle size. Figure 14a shows the carnauba straw (CS) and dewaxed carnauba straw (DCS) leaves, while Figure 14b presents the raw material after shredding and sieving.

Figure 14 – (a) Carnauba straw (CS) and Dewaxed Carnauba Straw (DCS)

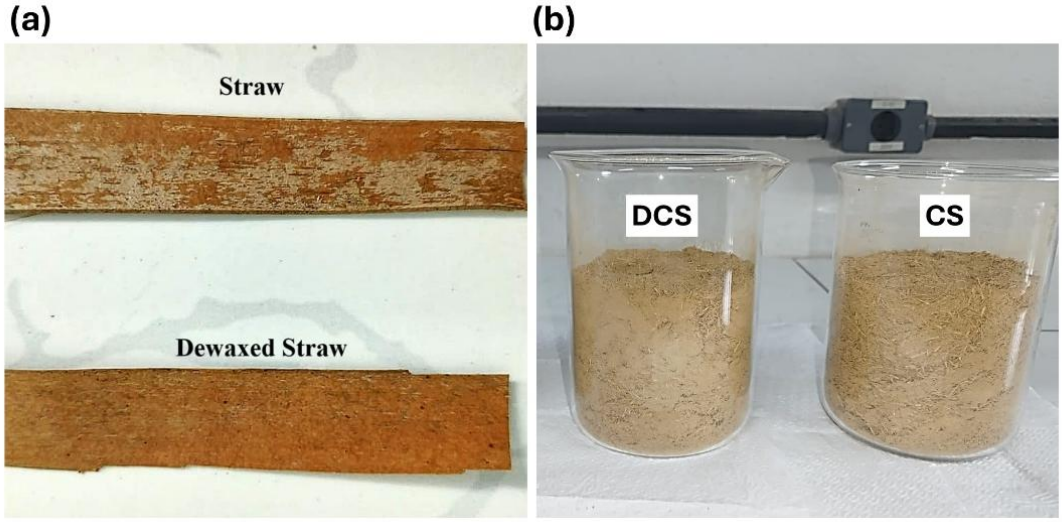

Source: Author

The shredding and sieving steps followed preparation method A of the ASTM E1757-01 (American Society for Testing and Materials, 2015) standard, which defines procedures for processing biomass into a suitable form for compositional analysis.

3.1.2 Biochar conversion

After the previous procedure, the CS and DCS samples were submitted, separately, to the carbonization process. The samples were placed in a ceramic crucible with a lid to ensure anaerobic conditions at atmospheric pressure and heated in a muffle furnace (Q318m21, Quimis, Brazil) — Figure 15a — from room temperature to 550 °C at a controlled rate of 10 °C/min, followed by a residence time of 1 hour at the target temperature. After the hold time, the furnace was turned off and allowed to cool to room temperature. The resulting biochar (CSB and DCSB, Figure 15b) was then removed and stored in a desiccator containing silica gel to cool completely and prevent any moisture reabsorption prior to characterization.

Figure 15 - (a) Muffle furnace used for the carbonization of carnauba straw samples; (b) Produced biochars

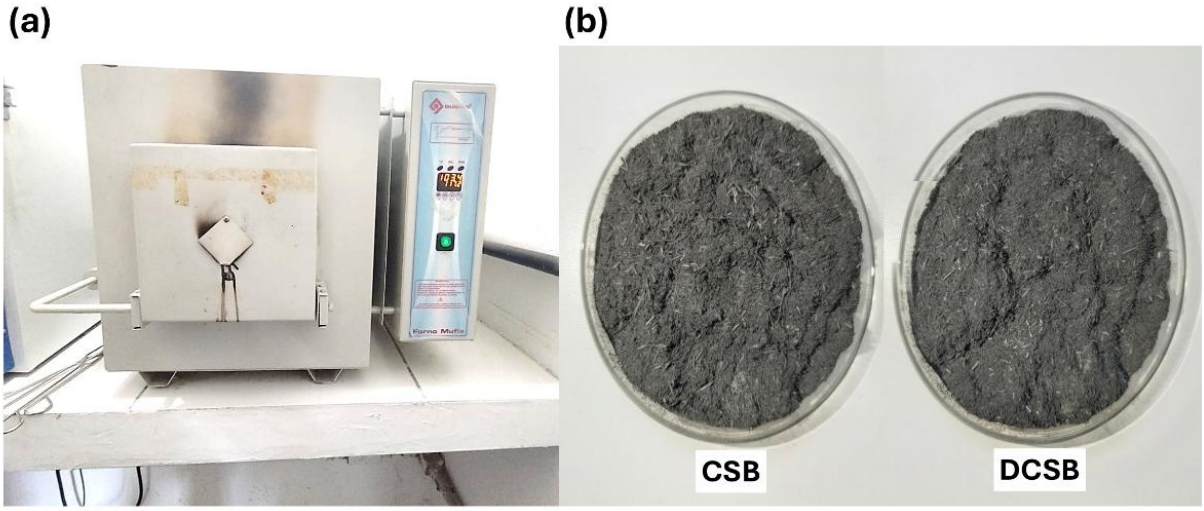

Source: Author

3.1.3 BCC preparation

The clay used to prepare BCC samples was a commercially available enological sodium bentonite (MASTER®, Brazil) — Figure 16. Its mineralogical and chemical characteristics were evaluated by XRD, FTIR, SEM–EDS analyses and TG/DTG, with the detailed results presented in Appendix A. Biochar–clay composites (BCC) were prepared by mixing biochar and bentonite in a 5:1 mass ratio under dry conditions(Akanji *et al.*, 2023; Gao; Goldfarb, 2021), without the use of solvents or dispersing agents. The mixtures were homogenized prior to the milling process.

Figure 16 - Bentonite Clay

Source: Author

3.2 High Energy Ball Milling

High-energy ball milling was carried out using a Pulverisette 6 (Fritsch GmbH, Germany) planetary mill (Figure 17a). Both biochar samples and biochar–clay composites were processed, with 10 g of material per batch. Stainless steel (AISI 304) balls (Figure 17b) were used, maintaining a 1:10 mass ratio (sample:balls)(Akanji *et al.*, 2023; Harindintwali *et al.*, 2023).

Figure 17 - (a) Planetary ball mill Pulverisette 6; (b) Stainless Steel AISI 304 Balls

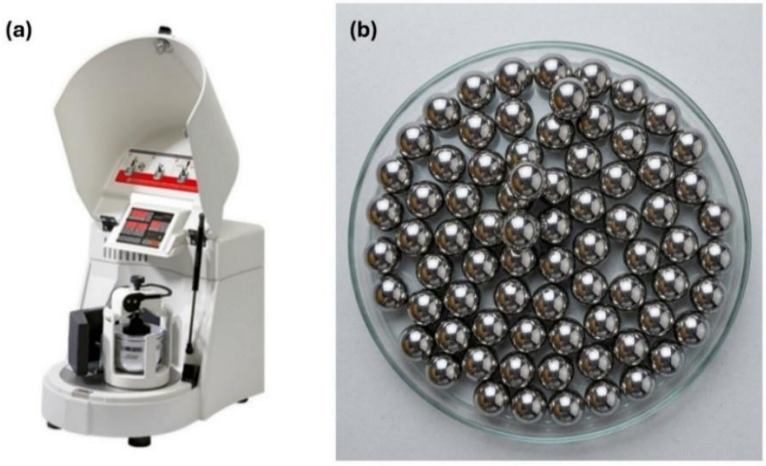

Source: Author

Milling was performed at different operating conditions: 200, 300, and 400 rpm for 2, 4, and 6 h, Table 5 presents the nomenclature adopted for the milled materials.

Table 5- Identification and coding of HEBM-modified samples

Material	**Sample type**	**Time (h)**	**Rotation speed (rpm)**		
			200	300	400
Biochar	CSB	2	CSB2002	CSB3002	CSB4002
		4	CSB2004	CSB3004	CSB4004
		6	CSB2006	CSB3006	CSB4006
	DCSB	2	DCSB2002	DCSB3002	DCSB4002
		4	DCSB2004	DCSB3004	DCSB4004
		6	DCSB2006	DCSB3006	DCSB4006
BCC	B-CSB	2	B-CSB2002	B-CSB3002	B-CSB4002
		4	B-CSB2004	B-CSB3004	B-CSB4004
		6	B-CSB2006	B-CSB3006	B-CSB4006
	B-DCSB	2	B-DCSB2002	B-DCSB3002	B-DCSB4002
		4	B-DCSB2004	B-DCSB3004	B-DCSB4004
		6	B-DCSB2006	B-DCSB3006	B-DCSB4006

Source: Author

The calculation of the specific milling energy is detailed in Appendix B.

3.3 Characterization techniques

3.3.1 Proximate Analysis

Proximate analysis was performed on CS and DCS samples and on their corresponding biochars (CSB and DCSB, respectively), with all measurements conducted in quadruplicate.

Moisture content. Moisture content was determined using a Shimadzu MOC63u moisture analyzer. Approximately 1 gram of each sample was analyzed at 105°C till the constant weight (American Society for Testing and Materials, 2011).

Volatile Matter. Approximately 1 gram of each sample were put in a porcelain crucible covered with a lid and placed in muffle furnace, maintained at 950 °C ± 20 °C for 7 minutes (American Society for Testing and Materials, 2019). The weight loss percent —i.e. volatile matter (VM) percent — was calculated by the following Equation 6:

$$\mathrm{VM}\ (\%) = 100\ \times \left(\frac{\mathrm{W_i} - \mathrm{W_f}}{\mathrm{W_i} - \mathrm{W_c}}\right) \tag{6}$$

Ash Content. Approximately 1 gram of each sample were put in a porcelain crucible and placed in muffle furnace at 575 °C ± 25 °C for 3 hours (ASTM E1755(American Society for Testing and Materials, 2001)). The ashes content percentage was calculated using Equation 7:

$$Ash\ (\%) = 100 \times \left(\frac{(W_i - W_f) \times 100}{W_s \times W_i}\right) \tag{7}$$

The remaining material from each sample (CS, DCS, CSB, and DCSB) was stored in an airtight container for subsequent ash characterization.

Fixed Carbon. The fixed carbon (FC) content was calculated by applying the mass balance for each sample using Equation 8:

$$FC\ (\%) = 100\ -\ (MC +\ VM + AC) \tag{8}$$

3.3.2 Elemental Analysis

Elemental composition (C, H, N) was determined by direct combustion using a Perkin Elmer 2400 Series II analyzer (PerkinElmer, USA). Approximately 2 mg of feedstock and its biochar samples were weighed in tin capsules and analyzed in duplicate. Oxygen content was calculated by difference from the carbon, hydrogen, and nitrogen contents.

3.3.3 SEM/EDS

Surface morphology and elemental composition were analyzed using a scanning electron microscope (TM3000, Hitachi, Japan) coupled with an energy-dispersive spectroscopy system (ED3000, Swift Analytical, UK). Imaging was conducted in SE and BSE modes at an accelerating voltage of 15 kV. Elemental composition was determined by EDS over the 0–20 keV spectral range. Data analysis focused on identifying morphological differences and variations in elemental composition among raw, biochar, and ash samples. SEM/EDS analyses were also carried out on bentonite clay.

3.3.4 XRD

X-ray diffraction patterns were obtained using a diffractometer (X'Pert PRO, PANalytical, Netherlands). This analysis of realized using Co-Kα radiation and data were collected over a 2θ range of 3º–100º with a step size of 0.013º.

3.3.5 FTIR

Fourier-transform infrared (FTIR) spectra were collected using a Bruker VERTEX 70v spectrometer with an ATR attachment. A Globar source was used for mid-infrared region measurements, with detection by a DLaTGS pyroelectric detector. Spectra were acquired in the range of 4000 to 380 cm^{-1} at a resolution of 2 cm^{-1}, averaging 128 scans per sample.

3.3.6 Thermal Analysis

Thermogravimetric (TG), differential thermogravimetric (DTG), differential scanning calorimetry (DSC) and differential thermal (DTA) analyses were performed using a thermal analysis (STA 449 F3 Jupiter, NETZSCH, Germany) equipment. The sample was subjected to a temperature range of 30 °C to 900 °C, with a heating rate of 10.0 K/min, in a controlled atmosphere. An Al_2O_3 crucible was used, with shielding gas (nitrogen, flow rate of 20 mL/min) and purge gas (synthetic air 80/20, flow rate of 50 mL/min).

3.4 Adsorption Studies

Adsorption experiments were carried out in batch mode using biochar and biochar–clay composites as adsorbents. Methylene blue (MB, CAS: 122965-43-9, $C_{16}H_{18}ClN_3S{\cdot}xH_2O$, MW: 319.85 g mol^{-1}, Neon, Brazil) was employed as adsorbate and prepared using distilled water. A stock solution with concentration of 1.0 g L^{-1} was prepared by dissolving 1.0 g of MB in 1.0 L

of distilled water. Working solutions at the desired concentrations were obtained by appropriate dilution of the stock solution.

For construction of the methylene blue calibration curve, the stock solution was diluted to prepare ten standard solutions with concentrations of 0.15, 0.5, 1, 2, 5, 7.5, 10, 15, 17.5, and 20 mg L^{-1}. The absorbance of each solution was measured in quadruplicate using a UV–Vis spectrophotometer (UV-2600, Shimadzu, Japan) over a wavelength range of 400–800 nm. The MB concentration was determined at its maximum absorbance wavelength (λ = 664 nm).

3.4.1 Preliminary Screening Using Response Surface Methodology (RSM)

Due to the large number of biochar samples modified by high-energy ball milling under different conditions, Response Surface Methodology (RSM) was employed as a preliminary adsorption screening strategy to select representative samples for detailed characterization and adsorption studies. The screening assays were carried out in 50 mL glass beakers containing 10 mL of MB solution (15 mg L^{-1}) at pH 6.0, using 2 mg of adsorbent under constant agitation. The adsorption performance was evaluated based on adsorption capacity (mg g^{-1}) and the milled biochars with and without bentonite exhibiting the highest and lowest adsorption performances were selected for subsequent analyses.

3.4.2 General Adsorption Procedure

Adsorption assays were conducted using the unmodified biochars and the modified biochars with and without bentonite selected after the preliminary adsorption screening in 100 mL glass beakers containing 50 mL of MB solution at pH 6.0, using a predetermined mass of adsorbent.

All experiments were performed in quadruplicate under agitation in a horizontal shaker (SK-180-Pro, Go Shaker, China) at 250 rpm and 25 °C. After the specified contact time, the suspensions were centrifuged (MIKRO 120, Hettich, Germany) at 4000 rpm for 10 min to separate the solid phase from the supernatant. The absorbance of the supernatant was measured by UV-Vis spectrometry at 664 nm to determine the residual methylene blue concentration, which was calculated using Equation (1).

3.4.3 Effect of Adsorbent Dosage

The effect of adsorbent dosage on methylene blue removal was evaluated by varying the mass of biochar and biochar–clay composites. Adsorbent masses of 2, 5, 10, 15, 20, and 25

mg were added to 50 mL of methylene blue solution with an initial concentration of 15 mg L^{-1}. The experiments were conducted for a contact time of 120 min. The adsorption efficiency (%) for each adsorbent dosage was calculated using Equation (2). Table 6 presents the experimental conditions for dosage assays.

Table 6 - Experimental conditions for the adsorbent dosage assays

Experiment	Dye concentration (mg L^{-1})	Biochar mass (mg)	Solution volume (mL)	pH*	Contact time
Effect of biochar dosage	15	2, 5, 10,15,20,25	50	6	120 min

***Before each experiment, the solution pH was adjusted to 6.0 using 0.1 M HCl or 0.1 M NaOH.**

Source: Author

3.4.4 Effect of Contact Time and Adsorption Kinetics

Kinetic studies were performed using an initial methylene blue concentration of 15 mg L^{-1} and an adsorbent mass of 5 mg. Contact times of 0, 5, 15, 30, 60, 120, 180, and 240 min were investigated. The adsorption kinetics were evaluated using the pseudo-first-order (PFO), pseudo-second-order (PSO), Elovich, and Weber–Morris models, according to Equations (6, 7, 8 and 9 respectively).Table 7 summarizes the experimental conditions employed in the kinetic adsorption experiments.

Table 7 - Experimental conditions employed in the effect of contact time experiments

Experiment	Dye concentration (mg L^{-1})	Biochar mass (mg)	Solution volume (mL)	pH*	Contact time
Effect of contact time	15	5	50	6	0, 5, 15, 30, 60, 120, 180, 240 min

***Before each experiment, the solution pH was adjusted to 6.0 using 0.1 M HCl or 0.1 M NaOH.**

Source: Author

3.4.5 Effect of the Initial Dye Concentration and Adsorption Isotherms

Adsorption isotherm experiments were conducted to investigate the equilibrium adsorption behavior of methylene blue. Solutions with initial concentrations of 2.5, 5, 8, 10, 15, 20, 40, 50, 70, and 100 mg L^{-1} were used, with a contact time of 120 min. The experimental equilibrium data were fitted to the Langmuir and Freundlich isotherm models using Equations

(2) and (3), respectively. The conditions adopted for the adsorption isotherm experiments are presented in Table 8.

Table 8 - Experimental conditions for evaluating the effects of the initial dye concentration

Experiment	Dye concentration (mg L^{-1})	Biochar mass (mg)	Solution volume (mL)	pH*	Contact time
Effect of initial dye concentration	2.5, 5, 8, 10, 15, 20, 40, 50, 70, 100, 150	5	50	6	120 min

***Before each experiment, the solution pH was adjusted to 6.0 using 0.1 M HCl or 0.1 M NaOH.**

Source: Author

4 RESULTS AND DISCUSSION

4.1 Screening of Milled Samples Using Response Surface Methodology (RSM)

Response Surface Methodology (RSM) was employed as a preliminary screening tool to systematically evaluate the influence of high-energy ball milling parameters on the adsorption performance of the prepared materials and to identify representative samples for further physicochemical characterization and detailed adsorption studies. The experimental results were analyzed considering milling speed and milling time as the main process variables affecting adsorption capacity(q_e).

The contour plots presented in Figure 18a–d illustrate the combined effects of milling speed and milling time on the q_e for the different materials, while the corresponding plots of adsorption capacity as a function of specific milling energy (Figure 18e–f) provide an integrated representation of the mechanical activation effect.

Figure 18 - Effect of milling parameters on adsorption capacity. Contour plots for (a) CSB, (b) BCSB, (c) DCSB, and (d) BDCSB; and adsorption capacity as a function of specific milling energy for samples derived from (e) CSB and (f) DCSB.

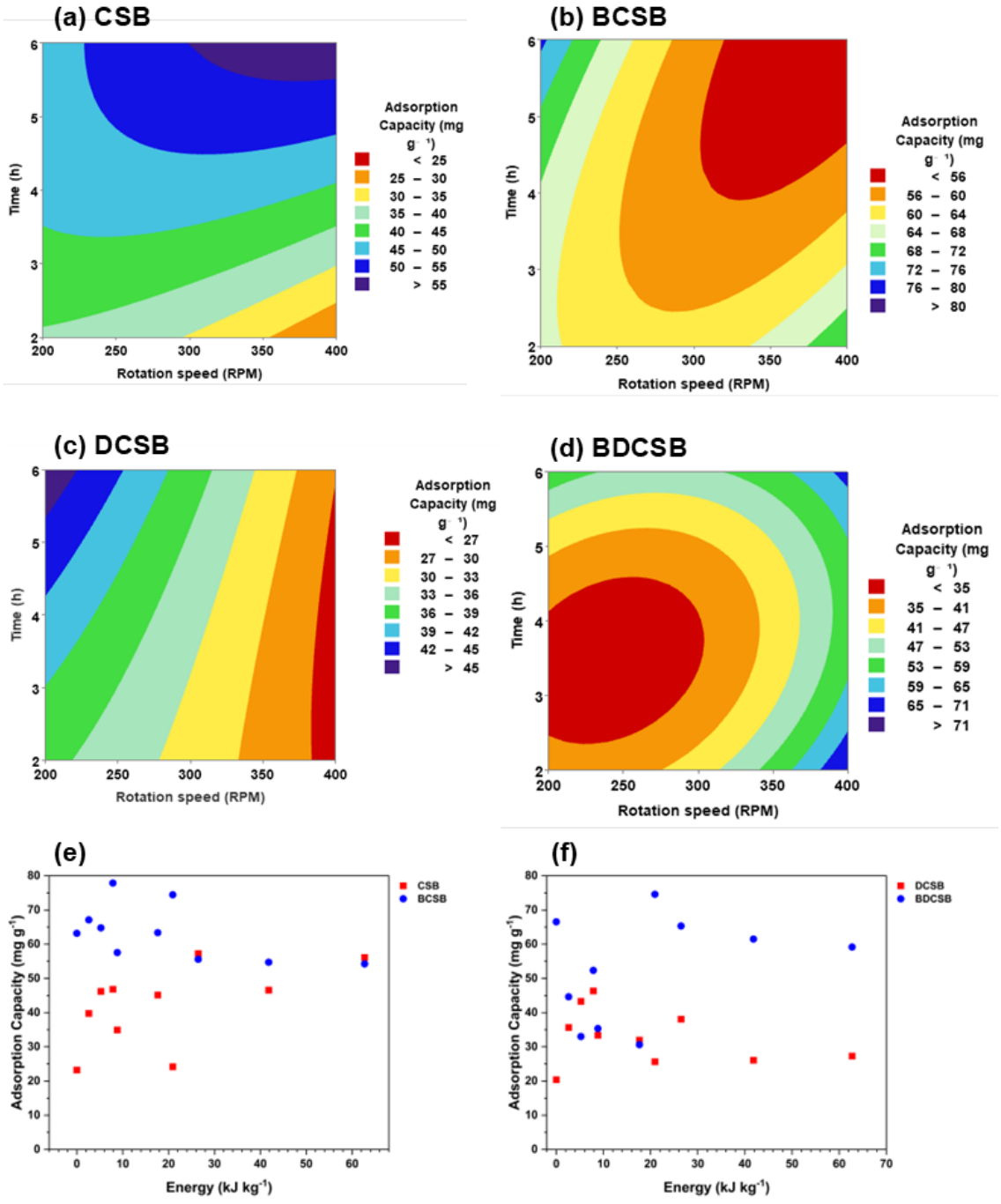

Source: Author

For the pristine biochars CSB and DCSB, the contour plots (Figure 18a and 18c) indicate that mechanical milling generally improves the adsorption performance compared to the non-milled samples. The adsorption capacity of CSB increased from approximately 23 mg g^{-1} to values above 55 mg g^{-1}, while DCSB increased from approximately 20 mg g^{-1} to around 46 mg

g^{-1} under specific milling conditions. These results suggest that high-energy milling promotes structural modifications in the biochar matrix that increase the accessibility of adsorption sites.

Regarding specific energy dependence (Figure 23e–f) reveals that the optimal milling conditions were material-dependent. For CSB, the highest adsorption capacity (57.26 mg g^{-1}) was achieved at a specific energy of 26.46 kJ g^{-1} (300 rpm, 6 h). Further increasing the energy to 41.82 kJ g^{-1} (400 rpm, 4 h) or 62.73 kJ g^{-1} (400 rpm, 6 h) did not result in additional improvements; on the contrary, a slight decline in performance was observed. This behavior suggests that, beyond an optimal energy threshold, excessive milling may induce detrimental effects such as particle agglomeration, pore collapse, or structural over-amorphization, which can reduce the accessibility of adsorption sites.

In contrast, DCSB exhibited a different response. The maximum adsorption capacity for this material (46.35 mg g^{-1}) was achieved at a much lower specific energy of 7.86 kJ g^{-1} (200 rpm, 6 h). At higher energies (e.g., 62.73 kJ g^{-1})the adsorption capacity decreased by approximately 45% relative to the optimum, indicating that DCSB is more sensitive to excessive milling than CSB.

This differential response may be attributed to the dewaxing process, which removes the waxy coating and exposes a more reactive or more fragile surface. The absence of wax may reduce the lubricating effect during milling, leading to more intense mechanochemical stress and faster onset of structural degradation. Alternatively, the higher ash content of DCSB (28.60% vs. 22.73% for CSB) may influence the energy dissipation mechanisms during ball impacts, altering the effective energy transferred to the carbonaceous fraction.

Such improvements are commonly associated with structural changes induced by mechanical activation. Previous studies have shown that ball milling can increase pore volume and expose previously occluded micropores while also enhancing the concentration of oxygen-containing functional groups on the biochar surface(Lopez-Tenllado; Motta; Hill, 2021). These changes increase the number of accessible adsorption sites and can enhance interactions between the adsorbent and target contaminants.

In addition to changes in porosity and surface chemistry, ball milling can significantly reduce the particle size of biochar. Harindintwali et al. (2023) reported that mechanical milling may transform granular biochar into ultrafine or nano-scale particles, improving dispersion in aqueous systems and facilitating contaminant diffusion toward adsorption sites. This reduction in particle size and improved dispersion may contribute to the enhanced adsorption capacities observed for the milled CSB and DCSB samples.

Behavior becomes more complex when bentonite is incorporated into the biochar matrix, as observed for BCSB and BDCSB (Figure 18b and Figure 18d). The control samples of these composites already exhibit relatively high adsorption capacities (≈63–66 mg g^{-1}), which suggests that the mineral phase may contribute significantly to the adsorption process. Mechanochemical activation can also modify clay minerals. For instance, Kovalchuk et al. (2023) demonstrated that high-energy milling of montmorillonite can partially amorphized the crystalline structure, reduce particle size, and increase the specific surface area, creating additional reactive sites for adsorption.

For the BCC samples, the relationship between specific energy and adsorption capacity differed notably from that of the pristine biochars (Figure 23e–f). BCSB achieved its highest q_e (77.87 mg g^{-1}) at 7.86 kJ g^{-1} (200 rpm, 6 h) — the same energy that optimized DCSB — while BDCSB reached 74.58 mg g^{-1} at 20.91 kJ g^{-1} (400 rpm, 2 h). More importantly, both BCC samples maintained relatively high adsorption capacities across a broader range of milling energies compared to their pristine counterparts. For example, even at the highest energy tested (62.73 kJ g^{-1}), the q_e values for BCSB and BDCSB remained above 54 mg g^{-1}, representing less than 30% loss from their respective optima. In contrast, pristine CSB and DCSB lost approximately 40–55% of their optimal q_e under similar conditions.

This broader energy tolerance suggests that the presence of bentonite may serve a protective or stabilizing role during HEBM. The clay particles could act as a lubricant or buffer, reducing the intensity of direct biochar–biochar and biochar–ball collisions, thereby preventing excessive structural degradation(Chen, S. *et al.*, 2022; Uçurum; Özdemir, 2024). Alternatively, the formation of biochar–clay interfaces may create new adsorption sites that compensate for any loss in carbonaceous porosity(Hamzaoui *et al.*, 2015). These observations indicate that the mechanochemical response to HEBM is highly dependent on material composition and pre-treatment history(Marsh *et al.*, 2026), and that optimization of milling parameters must be performed on a case-by-case basis rather than assuming universal conditions.

However, prolonged mechanical treatment may also induce structural destabilization and particle aggregation. Dellisanti; Valdré (2005) reported that extended milling can progressively reduce crystallite size while promoting aggregation phenomena, whereas Ng et al. (2022) observed that prolonged milling of biochar may lead to particle agglomeration due to mechanical compaction and hydrogen bond formation between particles. These effects can partially limit the accessibility of adsorption sites despite reductions in particle size.

This balance between structural activation and aggregation phenomena may explain the less systematic trends observed for the biochar–bentonite composites. While moderate milling may improve dispersion and increase the number of accessible adsorption sites, excessive mechanical energy may promote particle agglomeration or partial pore blockage within the composite structure. As illustrated in Figures 18e and 18f, adsorption capacities for BCSB and BDCSB remain relatively high across different milling energies but do not exhibit a clear monotonic increase.

These results reveal that the optimal specific energy for maximizing adsorption performance varies substantially among the four material types: approximately 26.5 kJ g^{-1} for CSB, 7.9 kJ g^{-1} for DCSB and BCSB, and 20.9 kJ g^{-1} for BDCSB. This variability underscores the importance of material-specific optimization in mechanochemical processing and highlights that factors such as wax content, ash composition, and clay incorporation profoundly influence the response to HEBM.

The RSM screening indicates that high-energy milling significantly enhances the adsorption capacity of pristine biochars, primarily through particle size reduction and structural activation, whereas its effect on biochar–bentonite composites is less pronounced due to the already dominant contribution of the mineral phase and the potential occurrence of aggregation phenomena at higher milling energies.

Based on these results, the samples exhibiting the best and worst adsorption performances (presented in Table 9) were selected for further investigation, together with the corresponding control materials. These selected samples were subjected to additional physicochemical characterization as well as detailed adsorption studies, including kinetic and equilibrium isotherm experiments, to better understand the structural factors governing adsorption behavior.

Table 9 - Selected samples for detailed adsorption studies

Material	Sample	Adsorption Capacity (mg g^{-1})*	Selection
Biochar	CSB	23.23 ± 1.17	Control
	CSB4002	24.19 ± 0.53	Lowest
	CSB3006	57.26 ± 5.60	Highest
	DCSB	20.39 ± 0.74	Control
	DCSB4002	25.65 ± 0.49	Lowest
	DCSB2006	46.35 ± 1.74	Highest
BCC	BCSB4006	54.25 ± 4.67	Lowest
	BCSB2006	77.87 ± 1.80	Highest
	BDCSB3004	30.64 ± 0.25	Lowest
	BDCSB4002	74.58 ± 4.65	Highest

***Adsorption capacity values are reported as mean ± standard deviation (n=4)**

Source: Author

4.2 Physicochemical Characterization of Biomass and Biochars

4.2.1 Characterization of Raw Biomass and Unmodified Biochar

This section is based on results previously published in the article *"Production and Characterization of Carnauba Straw (Copernicia prunifera) Biochar: Influence of Wax Removal on Adsorption of Methylene Blue"(Coutinho da Silva et al., 2026)*, available through ACS Publications (DOI: 10.1021/acsomega.6c00684). As these results have already been discussed in detail in that work, only a summary of the main findings related to the characterization of the raw biomass and unmodified biochar is presented here to avoid redundancy.

The biochar yield and key physicochemical parameters are summarized in Table 10. Pyrolysis induced the expected compositional changes, characterized by an increase in ash content and fixed carbon, as well as a reduction in volatile matter and moisture. The dewaxing process affected primarily the inorganic fraction, resulting in higher ash content in DCS compared to CS. This trend remained after carbonization, although no statistically significant difference was observed between CSB and DCSB. These findings suggest that wax removal promotes the concentration of mineral constituents and slightly improves carbonization efficiency.

Table 10 - Biochar yield and key physicochemical parameters

Parameters	CS	DCS	CSB	DCSB
Yield (%)	-	-	33.68±1.01[a]	34.27±1.98[a]
Bulk Density (g cm^{-3})	0.2809 ± 0.0012[b]	0.2964 ± 0.0005[a]	0.2553 ± 0.0004[b]	0.2630 ± 0.0010 [a]
Proximate analysis				
Ash Content (%)	12.53 ± 0.31[a]	14.20 ± 0.85[b]	22.73 ± 1.02[a]	28.60 ± 4.30[a]
Volatile Matter (%)	71.60 ± 1.43[a]	69.90 ± 0.85[a]	35.10 ± 5.25[b]	19.00 ± 3.05[a]
Moisture (%)	8.32 ± 0.45[a]	8.97 ± 0.17[a]	3.49 ± 0.30[a]	4.23 ± 0.62[a]
Fixed Carbon (%)	7.57 ± 1.18[a]	6.97 ± 1.12[a]	38.67 ± 4.71[a]	48.21 ± 7.30[a]
Ultimate analysis and molar ratios				
C (wt%)	44.66 ± 0.11	42.24 ± 0.30	45.18 ± 0.25	45.63 ± 0.11
H (wt%)	5.29 ± 0.12	4.89 ± 0.14	1.49 ± 0.02	1.65 ± 0.01
N (wt%)	0.88 ± 0.010	0.88 ± 0.02	0.89 ± 0.02	0.92 ± 0.01
O (wt%)	36.66 ± 0.11	37.79 ± 0.46	29.73 ± 0.26	23.21± 0.11
H/C	1.41	1.38	0.39	0.43
O/C	0.62	0.67	0.49	0.43
(N+O)/C	0.84	0.92	0.68	0.53
EDS				
Si (wt%)	22.02	26.82	32.92	34.30
K (wt%)	15.28	6.66	9.39	5.88
Cl (wt%)	17.49	5.74	6.72	2.34
Ca (wt%)	5.04	13.05	4.08	5.29
S (wt%)	2.95	3.34	1.50	2.90
Mg (wt%)	1.58	1.37	1.26	1.25
Na (wt%)	-	-		0.36

CS: raw carnauba straw; DCS: dewaxed carnauba straw; CSB: carnauba straw biochar; DCSB: dewaxed carnauba straw biochar.

Values are expressed as mean ± SD when applicable (n=4 for yield, bulk density, and proximate and PSD analyses; n=2 for ultimate analysis). Values with different superscripts (a, b) in the same row and comparison group (CS vs DCS or CSB vs DCSB) are significantly different ($p \leq 0.05$).

Source: Adapted from Coutinho da Silva *et al.* (2026)

The elemental composition analysis (Figure 19a) revealed the typical transformation associated with thermal treatment, with enrichment in carbon and a reduction in hydrogen and oxygen contents in the biochars. Consequently, lower H/C and O/C molar ratios were observed, indicating the formation of more aromatic and structurally stable carbon matrices. The Van Krevelen diagram (Figure 19b) illustrates this transition, highlighting a slightly higher degree of deoxygenation for DCSB compared to CSB.

Figure 19 - (a) Elemental composition of the biomasses and biochars samples; (b) Van Krevelen diagram

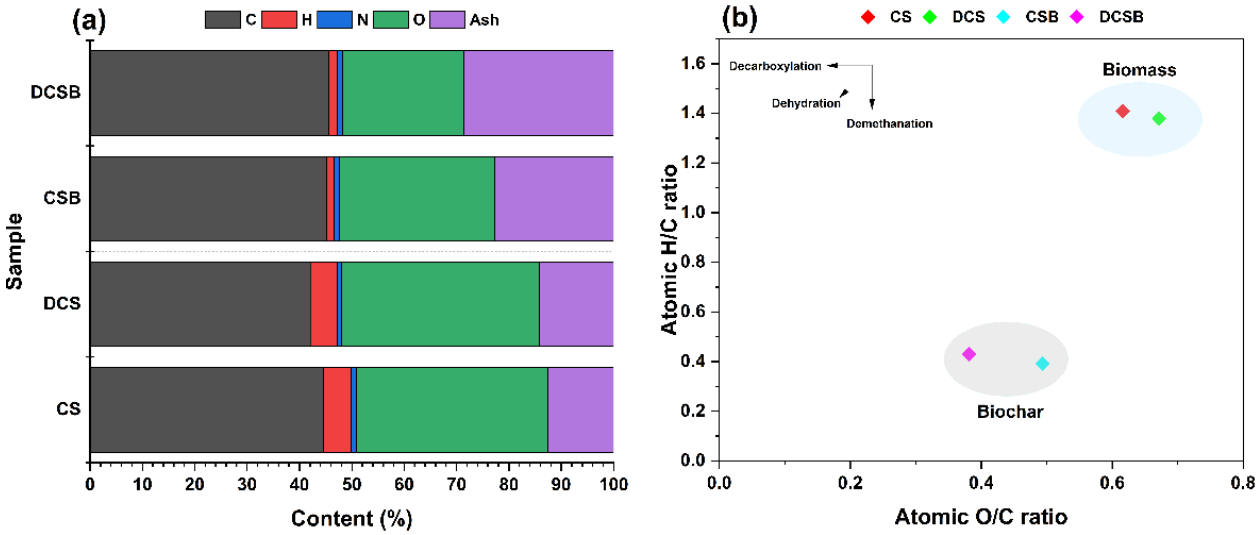

Source: Reproduced from Coutinho da Silva *et al.* (2026)

Morphological analysis by scanning electron microscopy (Figure 20a-f) demonstrated that both biomasses exhibit fibrous and heterogeneous structures, with the presence of silica-rich phytoliths distributed over the surface. After pyrolysis, the biochars showed fragmented and irregular carbonaceous structures with the development of porous features. The DCSB sample exhibited a more compact and aggregated morphology compared to CSB, which is consistent with its lower volatile matter content and greater degree of structural condensation.

Figure 20 - SEM micrographs of the raw biomasses and biochars. (a, b) CS at 30x and 1000x magnification. (c, d) DCS at 30x and 1200x magnification. (e) CSB (1200x). (f) DCSB (1200x)

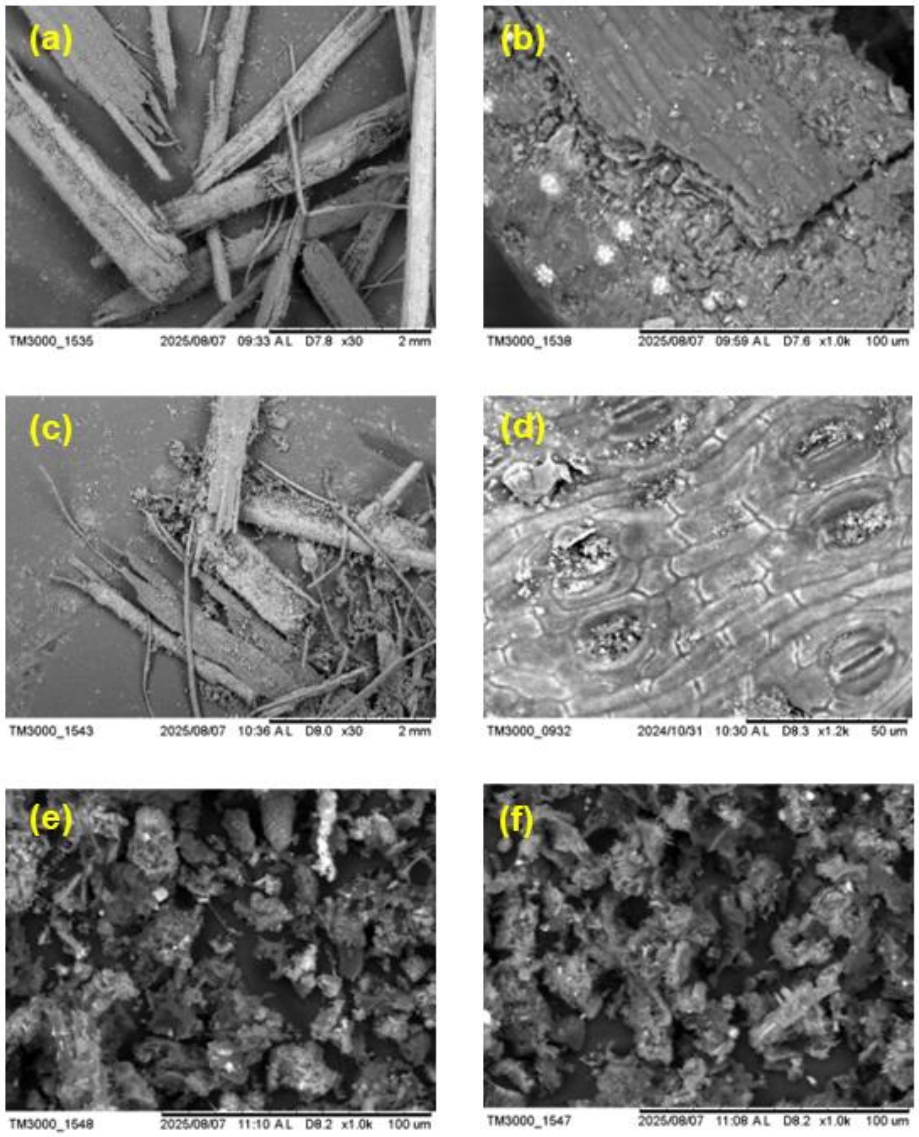

Source: Reproduced from Coutinho da Silva *et al.*(2026)

The elemental composition obtained by EDS (Table 9) confirmed the presence of silicon in all samples indicating the presence of phytogenic silica. After pyrolysis, an enrichment of inorganic components was observed due to the loss of organic matter. In contrast, potassium and chlorine contents decreased significantly, likely due to volatilization during thermal treatment.

X-ray diffraction spectrum (Figure 21) showed that the main crystalline phases present in the biomasses were preserved after pyrolysis, with increased peak intensity resulting from the removal of amorphous organic fractions. Additionally, the presence of a broad diffraction

band in the biochars is associated with turbostratic carbon structures, indicating the formation of partially ordered aromatic domains.

Figure 21 - XRD spectra of the biomasses and biochars samples

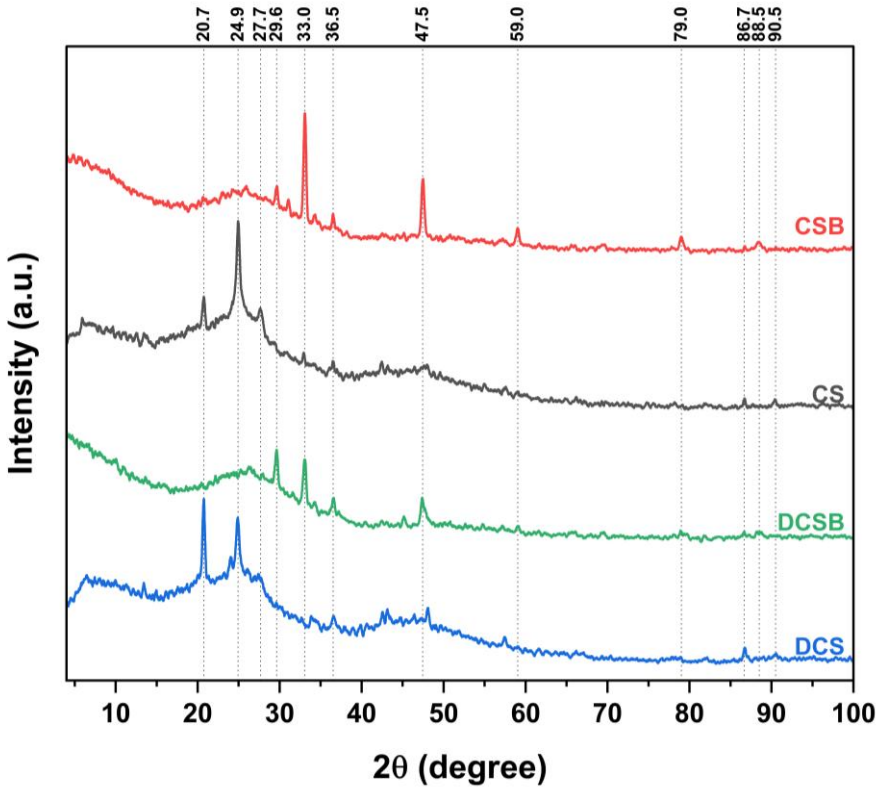

Source: Reproduced from Coutinho da Silva *et al.* (2026)

FTIR spectra (Figure 22) revealed the typical functional groups of lignocellulosic materials in the biomasses, including hydroxyl, aliphatic, and carbonyl groups. After pyrolysis, a significant reduction in oxygenated functional groups was observed, accompanied by the persistence of aromatic structures. These results confirm the progression toward a more condensed and recalcitrant carbon matrix.

Figure 22- FTIR spectra of the biomasses and biochars samples

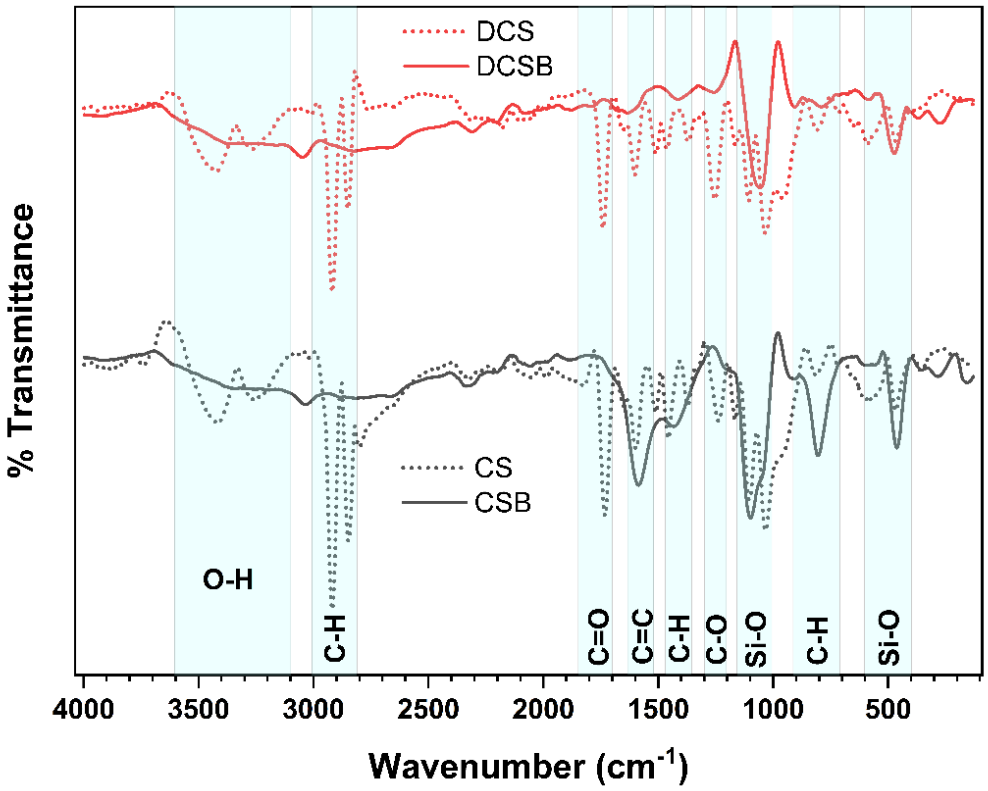

Source: Reproduced fromCoutinho da Silva *et al.* (2026)

Thermal analysis (Figure 23) demonstrated that biochars exhibit higher thermal stability than their precursor biomasses. The biomasses presented significant mass losses associated with hemicellulose and cellulose degradation, whereas the biochars showed reduced weight loss and degradation peaks shifted to higher temperatures. This behavior reflects the formation of thermally stable carbon structures during pyrolysis.

Figure 23 - Thermal analyses of biomasses and biochars: a)biomasses TG/DTG curves; b) biochars TG/DTG curves; c) biomasses DTA curves; and d)biochars DTA curves.

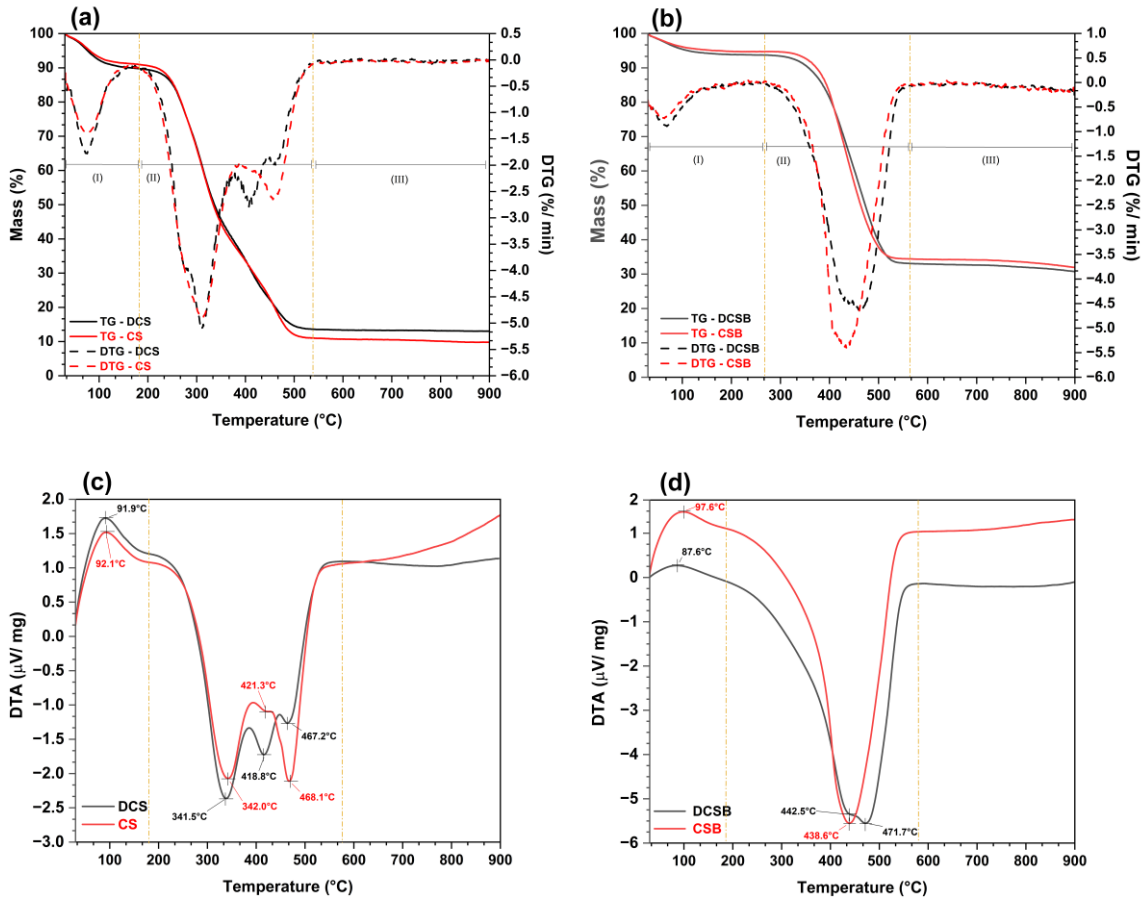

Source:Coutinho da Silva *et al.*(2026)

4.2.2 Characterization of Selected Milled Biochars and Biochar-Clay Composites

4.2.2.1 SEM/EDS

Figure 24 (a–h) shows the SEM micrographs of the modified biochars. The images reveal that the HEBM resulted in a highly fragmented morphology, with the samples presenting a fine powder-like appearance. The excessive particle size reduction led to the loss of the original structural features of the biochar, preventing the clear visualization of pores or surface textures. Similar morphological changes have been reported in the literature, where ball milling reduces particle size to the micro- and nanoscale, often leading to aggregated structures due to repeated compression and interparticle interactions(Lopez-Tenllado; Motta; Hill, 2021; Ng et al., 2022; Wang et al., 2023a). Additionally, prolonged or high-intensity milling may enhance agglomeration through particle–particle interactions and increased surface energy (Ng *et al.*, 2022).

Figure 24 - SEM micrographs of HEBM biochar and BCC selected samples: (a) CSB3006; (b) CSB4002; (c) BCSB2006; (d)BCSB4006; (e) DCSB2006; (f) DCSB4006; (g) BDCSB3004 and (h) BDCSB4002

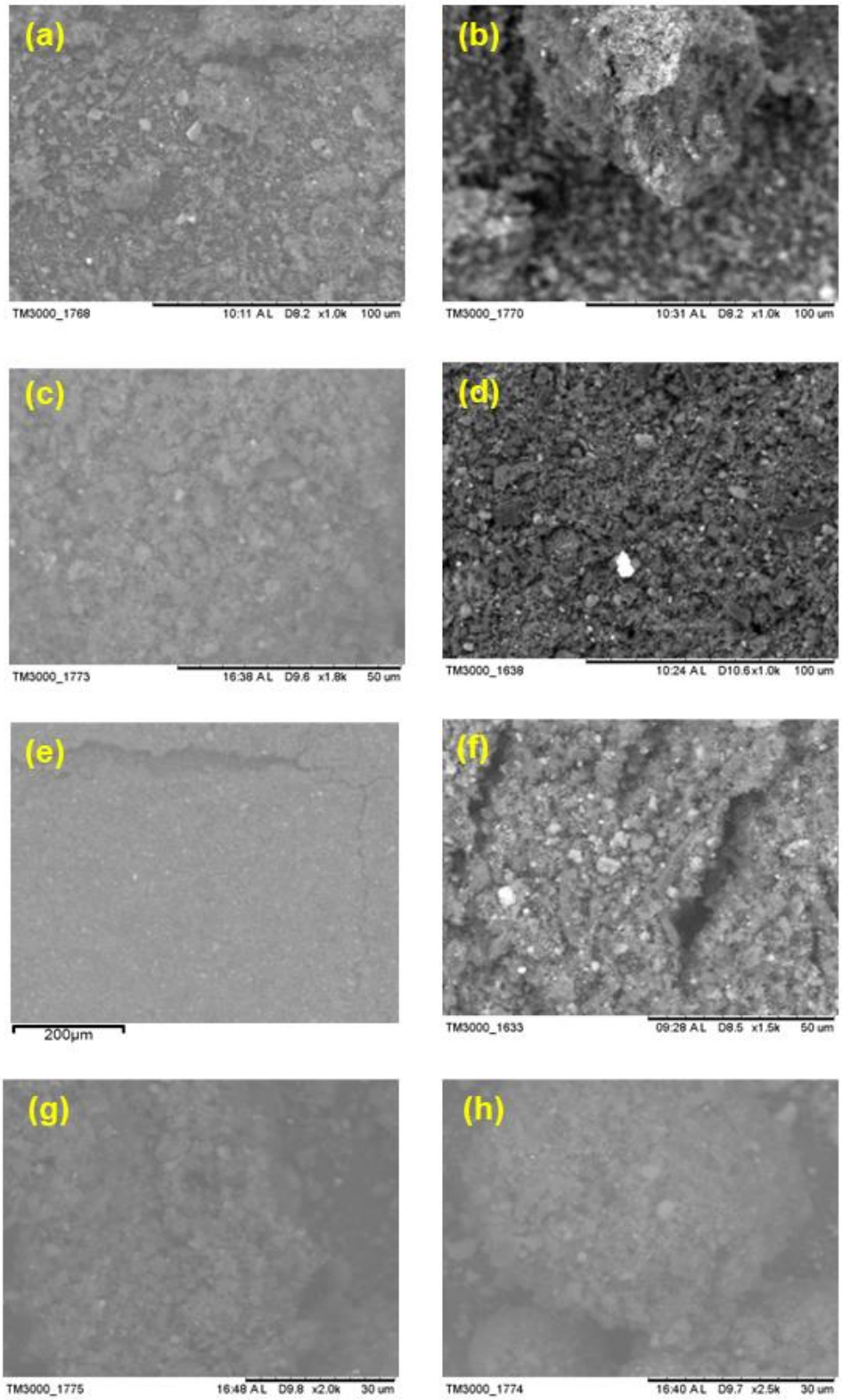

Source: Author

The observed morphology is also consistent with reports showing that HEBM can reduce biochar particle sizes from the micrometric range to submicron or nanometric scales, often accompanied by the formation of compact aggregates, which may limit the effectiveness of techniques such as DLS due to high variability and agglomeration effects (Lopez-Tenllado; Motta; Hill, 2021).

The elemental composition (wt%) determined by EDS analysis is shown in table 11. The results indicate significant variations among the samples, mainly associated with the modification process and the intrinsic composition of the precursor materials.

Table 11 - EDS composition of selected HEBM biochar and BCC samples

	Sample							
Element (wt%)	**CSB4002**	**CSB3006**	**BCSB4006**	**BCSB2006**	**DCSB4002**	**DCS2006**	**BDCSB3004**	**BDCSB4002**
Si	27.90	28.39	32.23	42.02	33.95	12.57	33.13	34.97
K	–	–	5.67	1.94	5.05	1.49	3.53	2.4
Cl	0.78	0.99	3.78	0.83	3.29	0.98	1.97	1.51
Ca	0.76	0.69	5.30	0.58	4.84	1.26	3.25	6.03
Mg	0.25	–	1.59	0.55	1.45	0.76	1.60	5.38
Na	–	–	0.53	0.39	–	–	0.99	0.65
Al	–	–	–	1.67	–	–	2.30	1.38
Fe	0.69	0.60	0.91	0.36	–	36.60	3.35	–
S	0.36	–	3.40	0.43	3.71	0.91	2.28	3.51
Cr	–	–	–	–	–	8.50	–	–
Ni	–	–	–	–	–	4.33	–	–

Note: Carbon (C) and oxygen (O) were omitted from the EDS results because the quantification of light elements by EDS is subject to significant uncertainty in carbon-rich matrices. Consequently, the reported concentration represents only the remaining detected elements and do not total 100%.

Source: Author

In BCC samples, an increase in Si and the presence of Al were observed, confirming the successful incorporation of the clay mineral, which is predominantly composed of silica and alumina. This is particularly evident in samples such as BCSB2006 and BDCSB3004, which show higher Si contents compared to their respective unmodified biochars.

No consistent trend was observed for K and Cl contents across all samples, suggesting that these elements are influenced by both the original biomass composition and the modification processes, including possible redistribution or concentration effects. This result is consistent with previous studies, where mineral elements such as Si, K, Ca, and Mg are commonly detected in biochars in the form of oxides or other inorganic phases, and their relative proportions can change significantly depending on post-treatment or modification processes (Wang, et al., 2023).

On the other hand, the presence of Fe, Cr, and Ni—particularly pronounced in sample DCSB2006—indicates contamination from the stainless steel milling media (AISI 304) used during high-energy ball milling.

4.2.2.2 FTIR

Figure 25 shows the FTIR spectra of milled biochars and biochar–clay composites (BCC) derived from (a) CSB and (b) DCSB. No significant shifts in peak positions were observed, indicating that the applied modifications did not alter the fundamental chemical structure of the biochar.

Figure 25 - FTIR spectra of HEBM biochars and BCC samples derived from (a) CSB and (b) DCSB

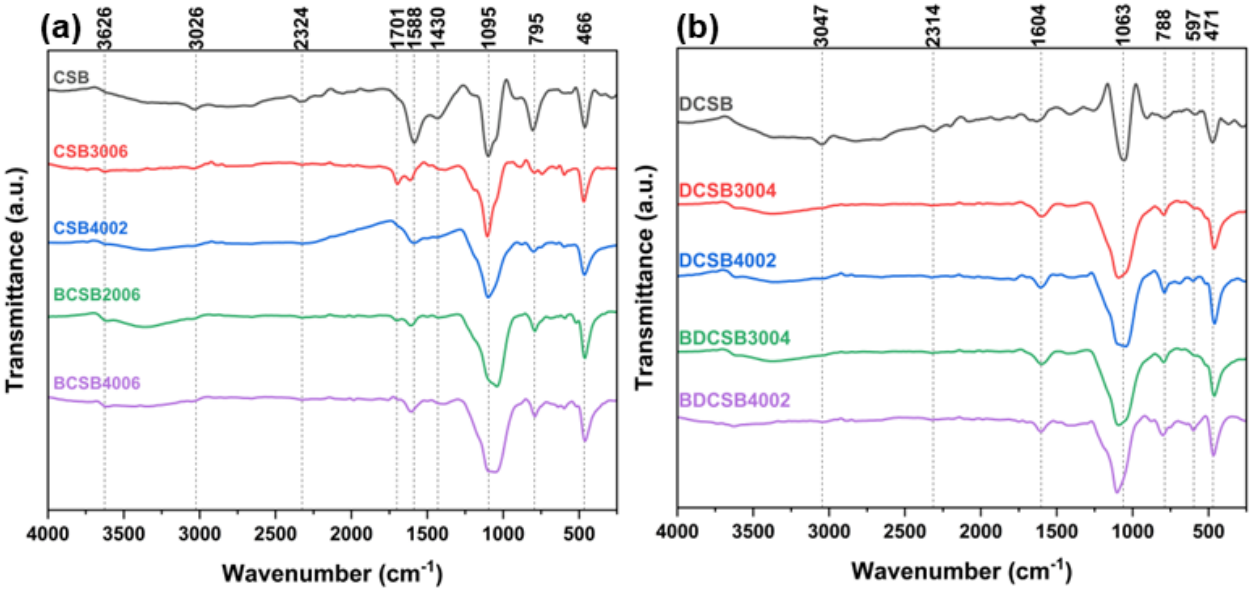

Source: Author

In Figure 25a, a slight decrease in the intensity of the band at ~1588 cm^{-1}, attributed to aromatic C=C stretching (Lopez-Tenllado; Motta; Hill, 2021; Ng *et al.*, 2022), was observed after milling. Since ball milling does not induce chemical changes in the biochar structure (Ng *et al.*, 2022), this variation is likely associated with changes in surface exposure or structural organization rather than modification of the aromatic framework itself.

In contrast, in Figure 25b, the band at ~1604 cm^{-1} (aromatic C=C)(Lopez-Tenllado; Motta; Hill, 2021; Ng et al., 2022; Wang et al., 2023) presented similar intensity across all samples, indicating that the aromatic structure of DCSB-derived materials remained largely unaffected by both milling and bentonite incorporation.

More pronounced differences were observed in the region between ~1000 and 1100 cm^{-1}, assigned to C–O stretching vibrations with possible contributions from Si–O bonds(Jiang et al., 2023; Ramesh; Raghavan, 2025; Wang et al., 2023). In bentonite-containing samples (BCSB and BDCSB), this band became broader and more intense, with a slight shift towards lower wavenumbers, indicating overlap between C–O and Si–O–Si vibrations and confirming the incorporation of the clay phase.

Additionally, bands in the ~460–600 cm^{-1} region, associated with Si–O and Al–O vibrations(Jiang *et al.*, 2023; Lopez-Tenllado; Motta; Hill, 2021), showed increased intensity in the modified samples, particularly those containing bentonite, further supporting the presence of mineral phases. Other bands, such as those around ~790 cm^{-1}, assigned to aromatic C–H out-

of-plane vibrations with possible contributions from silicate structures(Jiang *et al.*, 2023; Lopez-Tenllado; Motta; Hill, 2021; Ng *et al.*, 2022), became more defined in bentonite-containing samples, indicating increased structural heterogeneity.

These structural changes, particularly the increased contribution of siloxane (Si–O) groups and the preservation of oxygen-containing functionalities, may enhance adsorption performance by providing additional active sites. Such groups are known to contribute to adsorption through hydrogen bonding, electrostatic interactions, and n–π interactions with organic molecules such as methylene blue*(Jiang et al., 2023; Wang, et al., 2023)*.

The absence of peak shifts across all samples confirms that high-energy milling acts primarily as a physical modification method, without altering the chemical structure of the biochar(Ng *et al.*, 2022; Sewu *et al.*, 2019).

4.2.2.3 XRD

Figure 26 provides the XRD patterns of HEBM biochars and BCC samples. Consistent with previous findings for unmodified CSB and DCSB, all HEBM samples exhibited broad, low-intensity diffraction features characteristic of predominantly amorphous materials, with a diffuse shoulder at 2θ ≈ 20–30° assigned to the (002) plane reflection of turbostratic carbon structures (Ng *et al.*, 2022; Ramesh; Raghavan, 2025)

Figure 26 - XRD pattern of HEBM biochars and BCC samples derived from (a) CSB and (b) DCSB

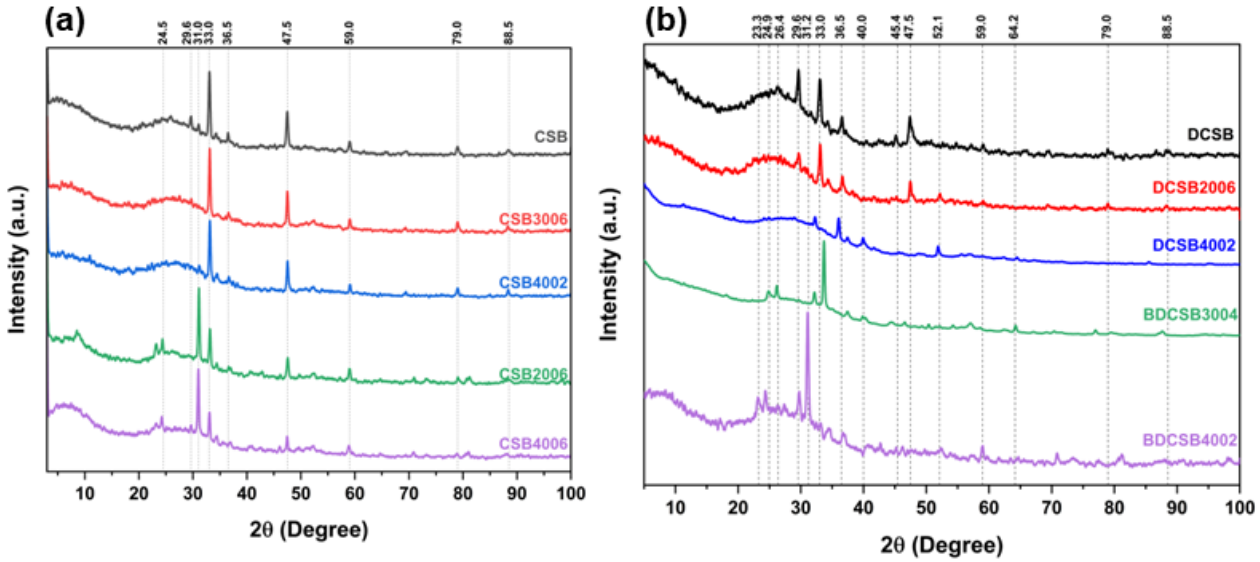

Source: Author

Compared to the unmodified biochars (CSB and DCSB), all HEBM samples showed a progressive decrease in overall peak intensity with increasing milling energy and time. Among

the CSB-derived samples, the order of decreasing intensity was: CSB4002 > CSB2006 > CSB4006 > CSB3006. This trend is consistent with the effect of high-energy ball milling, which induces mechanical stress, particle size reduction, and partial amorphization of the carbon structure (Li, H. *et al.*, 2023; Ng *et al.*, 2022). The shift in peak positions and the broadening of reflections, particularly in samples subjected to longer milling times (e.g., CSB3006 and CSB4006), can be attributed to residual stress accumulated within the turbostratic layers during the milling process (Ng *et al.*, 2022).

For the DCSB-derived samples, the intensity decreased in the order: DCSB2006 > BDCSB3004 > BDCSB4002. The bentonite-containing composites (BDCSB samples) exhibited lower intensities compared to the pristine milled DCSB. This reduction may reflect both the dilution effect of the clay fraction and additional structural disorder introduced by the interaction between biochar and bentonite during co-milling(Gao; Goldfarb, 2021). Characteristic reflections of montmorillonite were identified in the BDCSB samples at $2\theta \approx 5.4°$, 19.6°, and 35.3° (d = 18 Å), suggesting that the bentonite was well-dispersed within the biochar matrix and partially lost its crystalline order due to the HEBM process (Gao; Goldfarb, 2021; Ramesh; Raghavan, 2025).

Consistent with previous findings for unmodified biochars(Coutinho da Silva *et al.*, 2026), the milled samples retained the same mineral phases — i.e, calcite (≈29.7°), Ca- and K-bearing silicates and phosphates (≈33°), and quartz (≈36.5°, with higher-order reflections at ≈47.5°, ≈79°, and ≈90.5°) — although with reduced relative intensities. Similar mineral phases have been reported in bentonite-containing composites, with characteristic reflections of SiO_2, Al_2O_3, and MgO appearing at comparable 2θ angles(Hamad *et al.*, 2024). The persistence of these phases after ball milling indicates that the inorganic fraction remained largely unaffected by the mechanical treatment, while the carbonaceous structure became increasingly amorphous.

4.2.2.4 Thermal Analysis

The TG/DTG and DSC curves of the modified biochars are presented in Figure 27, and the main thermal parameters are summarized in Table 12.

Figure 27 - TG/DTG curves for the selected samples derived from (a) CSB (b)DCSB; and DSC curves for the selected samples derived from (c) CSB and (d) DCSB

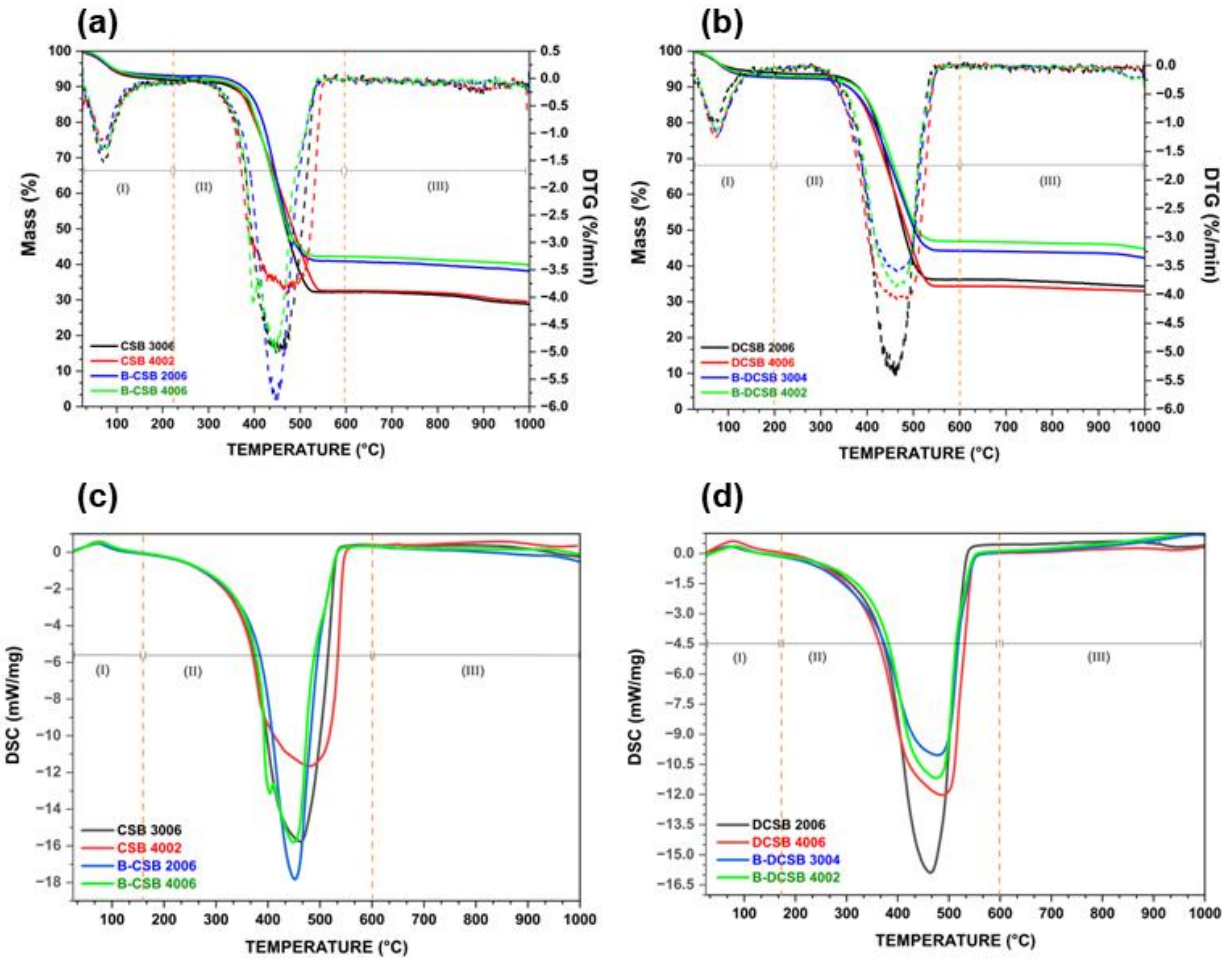

Source: Author

The thermal profiles show three main degradation regions, consistent with the behavior previously reported for CSB and DCSB(Coutinho da Silva *et al.*, 2026), but with important differences arising from bentonite incorporation and HEBM conditions.

In the first region (up to ~150 °C), all samples exhibited a relatively small mass loss (≈5.95–8.36%), with T_{max} values between 67 and 77 °C. This event is attributed to the release of physically adsorbed water and residual low-molecular-weight volatiles remaining after carbonization(Călin *et al.*, 2024; Yang *et al.*, 2007). These values are consistent with those previously reported for CSB and DCSB, indicating that the modification process does not

significantly alter the nature of moisture retention. However, slightly lower mass losses observed for bentonite-containing samples suggest that the mineral phase may reduce the amount of free water or modify its interaction with the carbon surface. The DSC curves in this region display mild endothermic signals, confirming that the process is dominated by dehydration phenomena.

The second region (≈200–600 °C) corresponds to the main degradation step, with mass losses ranging from approximately 46.45% to 60.07%. These values are comparable to those reported for unmodified biochars (~60.43%), confirming that this stage remains governed by the decomposition of residual organic structures and surface functional groups. This temperature range is typically associated with the degradation of labile and recalcitrant organic carbon fractions, including cellulose-derived structures and lignin-derived aromatic domains(Chen, D.; Zhou; Zhang, 2014; Leng *et al.*, 2019). Although biochars are already carbonized materials, remnants of these structural motifs still contribute to the observed mass loss.

The incorporation of bentonite leads to a clear reduction in mass loss, indicating increased thermal stability. This effect can be attributed to both the dilution of the organic fraction and the interaction between the carbon matrix and aluminosilicate phases, which can hinder thermal decomposition. Similar effects of additives or modifiers promoting changes in degradation behavior and residue formation have been reported in thermogravimetric studies of complex organic systems (Liu, L. *et al.*, 2023).

The T_{max} values further support this interpretation. Samples produced at higher temperatures show a shift toward higher T_{max} (up to 486.2 °C), consistent with increased structural ordering and enhanced resistance to thermal degradation, as peak temperature is widely recognized as a reliable indicator of thermal stability(Leng *et al.*, 2019). This trend agrees with previous observations for CSB and DCSB and reflects the formation of more condensed carbon structures.

On the other hand, some bentonite-modified samples exhibit slight decreases in T_{max} and higher degradation rates (e.g., BCSB 2006), suggesting that the mineral phase may also promote localized catalytic effects, accelerating the decomposition of specific carbon fractions. This behavior can be associated with mineral-induced alterations in decomposition pathways, which are not directly observable in TG alone but are commonly inferred from changes in DTG peak intensity and position(Wang, S. *et al.*, 2017).

The DSC curves reinforce these observations. In this region, all samples show pronounced exothermic peaks associated with the decomposition of remaining organic structures and rearrangement of the carbon matrix. The broad and overlapping nature of these peaks reflects the heterogeneous composition of the material, which includes carbon structures derived from hemicellulose, cellulose, and lignin that decompose over different temperature ranges (Chen, D.; Zhou; Zhang, 2014; Yang *et al.*, 2007). Variations in peak intensity and position among the modified samples indicate that bentonite influences not only thermal stability but also the decomposition pathways, likely by facilitating or hindering specific reactions.

In the third region (>600 °C), only minor mass losses are observed (≈1.37–3.42%), consistent with previously reported values for biochars. This stage is associated with the gradual degradation of highly condensed carbon structures and the stabilization of the material. According to the literature, this region may also involve transformations of refractory organic carbon and inorganic components, such as carbonates or mineral phases(Leng *et al.*, 2019; Liu, L. *et al.*, 2023). The absence of significant features in the DSC curves supports the interpretation that the carbon framework is largely stabilized at this stage. Slight differences among samples may be related to transformations in the mineral phase, particularly in bentonite-containing materials.

Generally, while thermal behavior remains consistent with that of previously reported biochars(Coutinho da Silva *et al.*, 2026), the present results demonstrate that bentonite incorporation and synthesis conditions significantly influence both the extent of mass loss and the degradation kinetics. In particular, the reduced mass loss in the main decomposition region and the modifications in T_{max} and V_{max} indicate that the mineral phase plays an active role in controlling the thermal response, rather than acting solely as an inert additive.

Table 12 - TG/DTG thermal degradation regions of the HEBM biochars and BCC samples

	Region I			Region II			Region III		
Sample	Δ (%)[a]	T_{max} (°C)[b]	V_{max} (% min^{-1})[c]	Δ (%)[a]	T_{max} (°C)[b]	V_{max} (% min^{-1})[c]	Δ (%)[a]	T_{max} (°C)[b]	V_{max} (% min^{-1})[c]
CSB 3006	8.36	70.1	-1.52	59.44	447.1	-5.02	3.42	–	–
CSB 4002	7.33	77.2	-1.15	60.07	476.6	-3.94	3.01	–	–
BCSB 2006	6.72	67	-1.31	52.41	446.5	-5.86	2.72	–	–
BCSB 4006	7.04	70.6	-1.32	50.9	448.3	-4.98	2.27	–	–
DCSB 2006	5.95	70.5	-0.98	57.83	462.8	-5.48	1.91	–	–
DCSB 4006	7.37	71.4	-1.26	58.26	486.2	-4.07	1.37	–	–
BDCSB 3004	7.13	75.9	-1.17	48.6	465.2	-3.59	1.99	–	–
BDCSB 4002	6.6	73.2	-1.15	46.45	461.9	-3.86	2.1	–	–

[a] Δ indicates the percentage of mass loss.
[b] T_{max} is the maximum degradation temperature obtained from DTG curves.
[c] V_{max} corresponds to the maximum degradation rate.

Source: Author

4.3 Methylene Blue Adsorption Experiments

4.3.1 Adsorption Performance of Unmodified Biochar

This section is based on results previously published in the article *"Production and Characterization of Carnauba Straw (Copernicia prunifera) Biochar: Influence of Wax Removal on Adsorption of Methylene Blue"(Coutinho da Silva et al., 2026)*, available through ACS Publications (DOI: 10.1021/acsomega.6c00684). As these results have already been discussed in detail in that work, only a summary of the main findings related to the adsorption performance of unmodified biochar is presented here to avoid redundancy.

4.3.1.1 Effect of biochar dose

The effect of biochar dosage on methylene blue adsorption (Figure 28a-b) followed the typical behavior observed in batch systems. An increase in adsorbent mass resulted in higher removal efficiency, while the adsorption capacity (q_e) decreased for both CSB(Figure 28a) and DCSB(Figure 28b). This inverse relationship is attributed to the greater availability of active

sites at higher dosages, leading to their incomplete saturation under fixed solute concentration conditions.

Figure 28 - Effect of biochar dosage on MB adsorption for (a) CSB and (b) DCSB

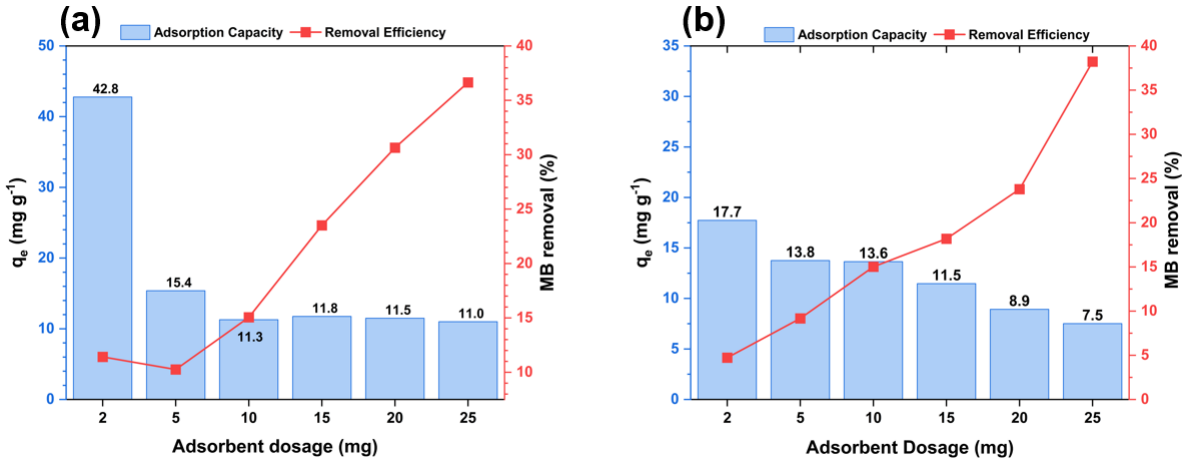

Source: Adapted from (Coutinho da Silva *et al.*, 2026)

DCSB exhibited higher adsorption capacities at lower dosages, indicating a more efficient utilization of active sites under conditions of high dye-to-adsorbent ratio. In contrast, CSB showed lower q_e values, suggesting more limited accessibility of adsorption sites.

4.3.1.2 Effect of contact time and kinetics models

The adsorption process was characterized by a rapid initial uptake within the first 60 minutes for both biochars, followed by a slower approach to equilibrium, which was reached at approximately 120 minutes (Figure 29a-b). This behavior reflects the initial abundance of available active sites and the subsequent reduction in adsorption rate as these sites become progressively occupied.

Figure 29 - Effect of contact time and kinetics models for (a) CSB and (b) DCSB

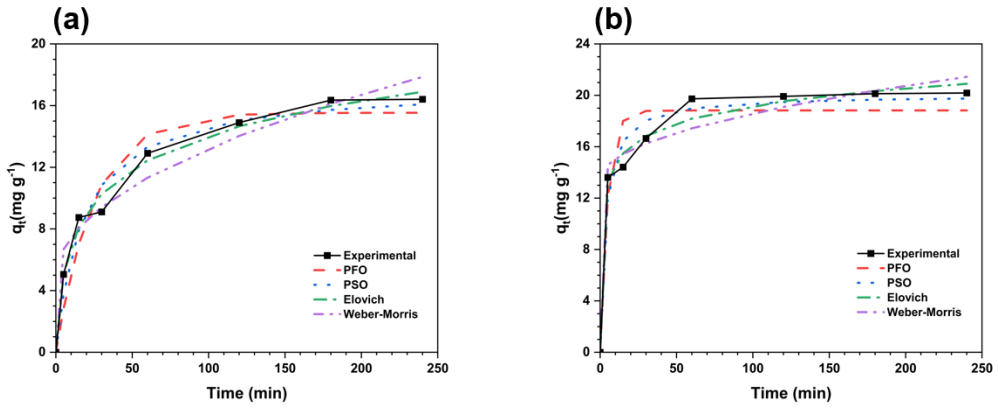

Source: Adapted from Coutinho da Silva *et al.*(2026)

As illustrated in Figure 29a (CSB) and Figure 29b (DCSB), DCSB presented a higher equilibrium adsorption capacity compared to CSB, indicating stronger affinity toward methylene blue molecules. The kinetic modeling revealed that the pseudo-first-order model did not adequately describe the experimental data, whereas the pseudo-second-order model provided the best fit for both materials (Table 13), suggesting that the adsorption process is predominantly governed by chemisorption mechanisms.

Table 13 – Parameters of the kinetic models fitted to MB adsorption data for pristine biochars

Model Type	Paramete	DCSB	CSB
Experimental	q_e(mg g^{-1})	20.18	16.41
Pseudo-first-order (PFO)	q_e (mg g^{-1})	18.82	15.54
	k_1 (h^{-1})	0.209	0.040
	R^2	0.496	0.876
Pseudo-second-order (PSO)	q_e (mg g^{-1})	20.02	17.28
	k_2(g mg^{-1} h^{-1})	0.0153	0.0033
	h (mg g^{-1} h^{-1})	6.12	0.97
	R^2	0.809	0.948
Elovich	α (mg/g h)	361.25	2.45
	β (g mg^{-1})	0.512	0.308
	R^2	0.913	0.980
Intraparticle diffusion (Weber–Morris)	k_p (mg/g h$^{1/2}$)	0.517	0.843
	C (mg g^{-1})	13.43	4.79
	R^2	0.804	0.925

Source: Reproduced from Coutinho da Silva *et al.*(2026)

Additionally, the Elovich model supported the presence of heterogeneous adsorption surfaces, while the intraparticle diffusion analysis indicated that adsorption occurs through multiple steps. The non-zero intercepts demonstrate that intraparticle diffusion is not the sole rate-limiting step, and that boundary layer diffusion also plays a significant role.

4.3.1.3 Effect of Initial MB dye concentration and adsorption isotherms

The increase in initial methylene blue concentration led to higher adsorption capacities for both biochars (Figure 30a-b), due to the enhanced mass-transfer driving force. At low concentrations, removal efficiency remained relatively constant, whereas higher concentrations promoted greater dye uptake until saturation of the available active sites was approached.

Figure 30 - Effect of Initial MB dye concentration and adsorption isotherms for (a) CSB and (b)DCSB

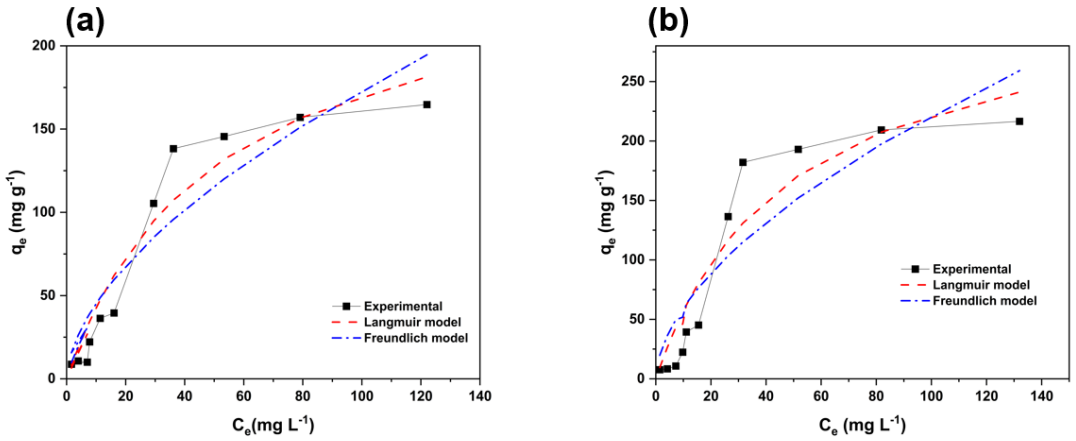

Source: Reproduced from Coutinho da Silva *et al.*(2026)

The equilibrium data (Table 14) were best described by the Langmuir isotherm model, indicating a predominance of monolayer adsorption. The maximum adsorption capacities confirmed the superior performance of DCSB in comparison to CSB. Furthermore, the values of the separation factor (R_L) indicated that the adsorption process was favorable across the studied concentration range. The Freundlich model also suggested favorable adsorption behavior, although with lower correlation compared to Langmuir.

Table 14 - Equilibrium data for CSB and DCSB

Model Type	Parameter	DCSB	CSB
Langmuir	**q_m (mg g^{-1})**	**328.13**	**255.70**
	K_L (L mg^{-1})	0.02102	0.02000
	R^2	0.902	0.934
	R_L	0.24-0.95	0.25-0.95
Freundlich	K_F	16.17	11.81
	N	1.76	1.71
	R^2	0.823	0.869

Source: Reproduced from Coutinho da Silva *et al.* (2026)

4.3.2 Adsorption Performance of Selected Milled Biochar and BCC samples

4.3.2.1 Effect of biochar dose

The effect of adsorbent dosage on MB removal for the selected samples is presented in Fig. 31a–b. For all materials, removal efficiency increased with increasing adsorbent mass, reflecting the greater availability of adsorption sites. However, this increase tended to level off at higher dosages, indicating a typical saturation behavior observed in batch adsorption systems(Nautiyal; Subramanian; Dastidar, 2016).

Figure 31 - Effect of biochar dose on MB removal for the selected samples derived from (a) CSB and (b) DCSB

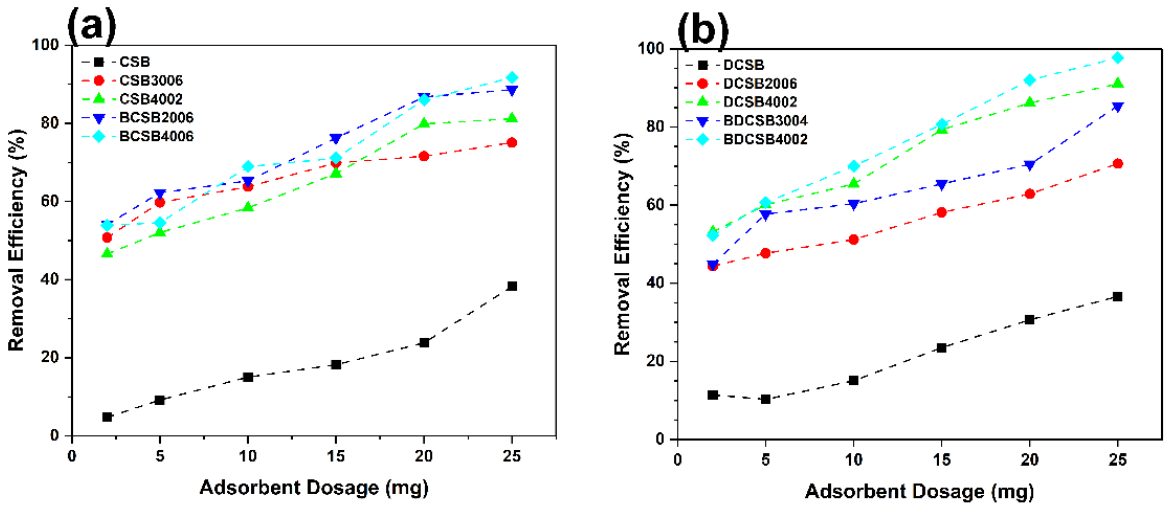

Source: Author

The extent of this increase depended on both milling conditions and material type. For CSB-derived samples, milling improved removal efficiency, with CSB3006 outperforming CSB4002, suggesting that longer milling time may be more effective than higher rotational

speed for this material. In contrast, DCSB-derived samples exhibited consistently higher efficiencies across the entire dosage range, with DCSB2006 showing better performance than DCSB4002, indicating that increasing milling intensity does not necessarily result in proportional gains in removal. This behavior is consistent with previous findings for dewaxed biochars, which generally exhibit improved adsorption performance compared to their wax-containing counterparts (Coutinho da Silva *et al.*, 2026).

A distinct behavior was observed for the BCC samples, which showed significantly higher removal efficiencies and reduced sensitivity to milling parameters. For instance, BDCSB4002 and BCSB4006 reached 97.75% and 91.72% removal at 25 mg, respectively. This trend is consistent with studies reporting that co-milling biochar with mineral phases promotes synergistic effects, leading to enhanced adsorption compared to individual or separately milled components(Jiang *et al.*, 2023).

Despite the general increase in removal efficiency, a diminishing return was observed at higher dosages, particularly above 20 mg. This behavior is typical of batch adsorption systems and is associated with a decrease in the adsorbate-to-adsorbent ratio, resulting in incomplete utilization of active sites and possible overlap at higher solid concentrations(Pan *et al.*, 2024; Ramola *et al.*, 2020).

4.3.2.2 Effect of contact time and kinects models

The kinetic behavior of the modified samples was evaluated and compared with the pristine biochars previously discussed. The experimental data and model fits for the selected samples are shown in Figure 32, where panels a–d correspond to CSB-derived samples, while panels e–h represent DCSB-derived samples.

Figure 32 - Effect of contact time and kinects models for the selected CSB- and DCSB-derived samples

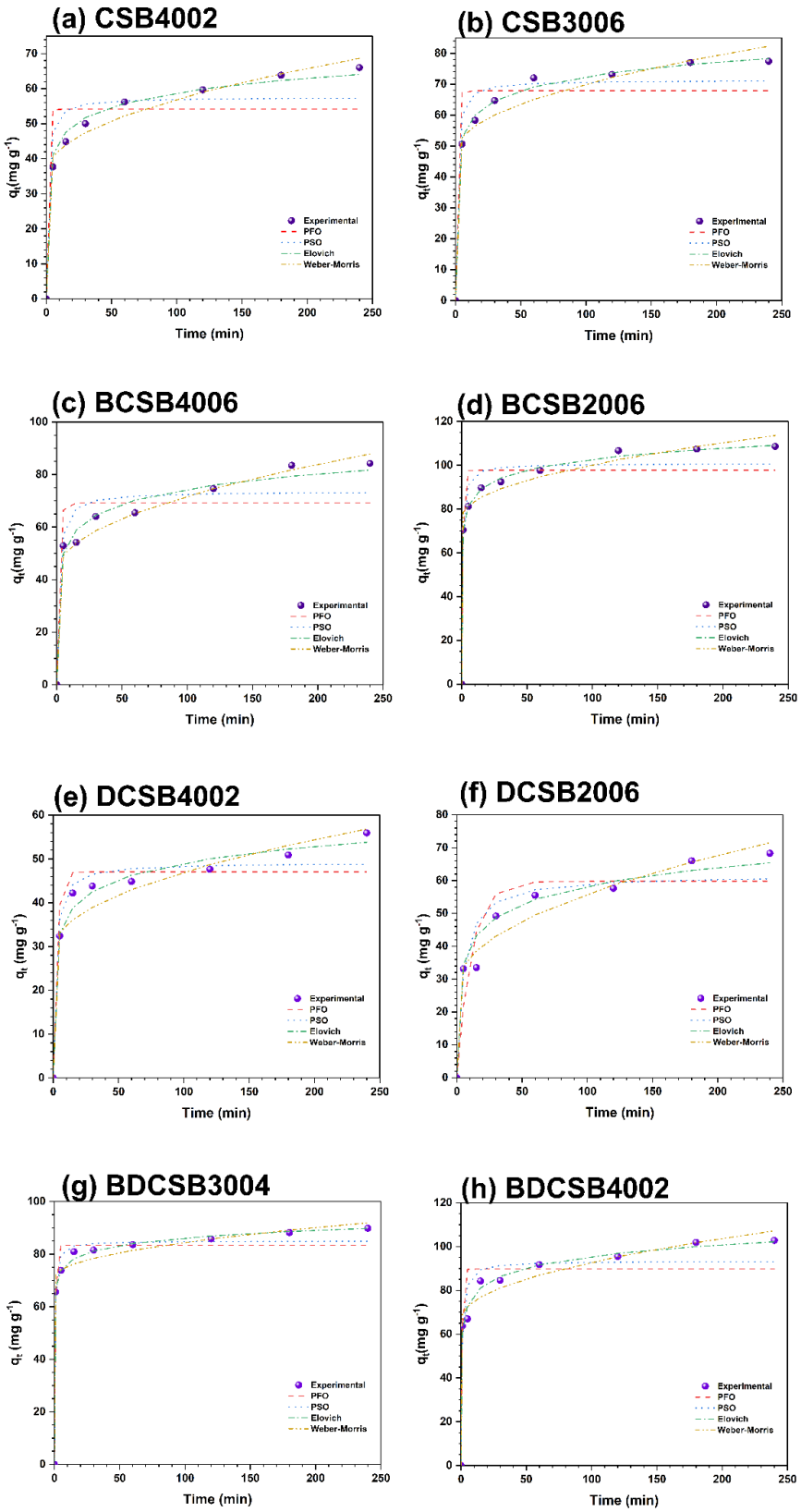

Source: Author

All samples exhibited a rapid initial adsorption stage followed by a gradual decrease in the adsorption rate until equilibrium was reached. This behavior is consistent with that observed for the pristine biochars (Figure 29) and reflects the initial abundance of available adsorption sites, followed by progressive site occupation(Coutinho da Silva *et al.*, 2026; Li, D. *et al.*, 2023; Wei *et al.*, 2020).

Within each group, differences associated with milling conditions and the presence of bentonite can be identified. In general, both milled biochars and BCC samples exhibited steeper initial slopes compared to the pristine materials, indicating faster adsorption kinetics. This improvement is commonly associated with particle size reduction, increased surface area, and enhanced accessibility of adsorption sites induced by ball milling(Kumar *et al.*, 2020).

The kinetic parameters (Table 15) indicate that the PFO did not adequately describe the adsorption behavior, as reflected by lower R^2 values and discrepancies between experimental and calculated q_e. The PSO model showed an improved fit compared to the PFO; however, it did not provide the best overall description of the adsorption kinetics.

Table 15 - Parameters of the kinetic models fitted to MB adsorption data for modified biochars and BCC samples

Model	Parameter	CSB4002	CSB3006	BCSB4006	BCSB2006	DCSB4002	DCSB2006	BDCSB3004	BDCSB4002
Experimental	q_e(mg g^{-1})	55.41	69.33	71.2	98.65	60.12	48.32	84.77	91.85
PFO	q_e (mg g^{-1})	54.23	67.88	69.24	97.73	59.82	47.05	83.41	89.8
	k_1 (h^{-1})	1.015	0.956	0.641	1.257	0.091	0.365	1.539	1.2
	R^2	0.317	0.463	0.479	0.501	0.448	0.669	0.619	0.394
PSO	q_e (mg g^{-1})	57.53	71.31	73.56	100.74	61.68	49.15	85.01	93.4
	k_2(g mg^{-1} h^{-1})	0.0162	0.0148	0.0093	0.0183	0.00345	0.0119	0.0347	0.0159
	h (mg g^{-1} h^{-1})	53.72	75.05	50.05	185.7	13.13	28.75	250.39	138.63
	R^2	0.572	0.716	0.686	0.709	0.651	0.848	0.807	0.639
Elovich	α (mg/g h)	1.23×10^{3}	3.81×10^{3}	6.74×10^{2}	1.24×10^{5}	1.16×10^{2}	4.66×10^{2}	4.02×10^{7}	2.16×10^{4}
	β (g mg^{-1})	0.169	0.151	0.121	0.14	0.125	0.185	0.24	0.131
	R^2	0.949	0.983	0.954	0.99	0.909	0.962	0.976	0.959
Weber–Morris	k_p (mg/g $h^{1/2}$)	2.115	2.22	2.913	2.421	2.838	1.785	1.349	2.609
	C (mg g^{-1})	35.87	47.92	42.69	76.02	27.55	29.17	71.03	66.79
	R^2	0.954	0.87	0.935	0.891	0.932	0.823	0.805	0.886

Source: Author

The highest R^2 values were generally obtained for the Elovich and intraparticle diffusion (Weber–Morris) models. The good fit of the Elovich model suggests that adsorption occurs on energetically heterogeneous surfaces(Nascimento *et al.*, 2020), which is consistent with the structural complexity of biochar-based materials and the modifications introduced by milling and clay incorporation(Akanji *et al.*, 2023; Kumar *et al.*, 2020).

A marked increase in the initial adsorption rate (h) was observed after modification. While the pristine biochars presented values of 6.12 mg $g^{-1}h^{-1}$ (DCSB) and 0.97 mg $g^{-1}h^{-1}$ (CSB), the modified samples exhibited significantly higher values. For instance, CSB3006 reached 75.05 mg $g^{-1}h^{-1}$, while BCC samples such as BCSB2006 and BDCSB3004 exhibited values of 185.70 and 250.39 mg $g^{-1}h^{-1}$, respectively, indicating a substantial enhancement in adsorption kinetics.

The Elovich parameter α also increased considerably after modification, particularly for BCC samples, reflecting a much faster initial adsorption stage. However, these values should be interpreted with caution due to their sensitivity to the fitting procedure(Nascimento *et al.*, 2020).

4.3.2.3 Effect of Initial MB dye concentration and adsorption isotherms

The effect of initial concentration on methylene blue adsorption for the modified samples is presented in Figure 33, where panels a–d correspond to CSB-derived materials and panels e–h to DCSB-derived samples. For all samples, the adsorption capacity increased with increasing initial dye concentration, reflecting the stronger mass-transfer driving force and enhanced diffusion of MB molecules toward available adsorption sites (Chistie et al., 2025; Goswami et al., 2022; Li, D. et al., 2023; Nautiyal; Subramanian; Dastidar, 2016).

Figure 33 - Effect of Initial MB dye concentration and adsorption isotherms for the the selected CSB- and DCSB-derived samples

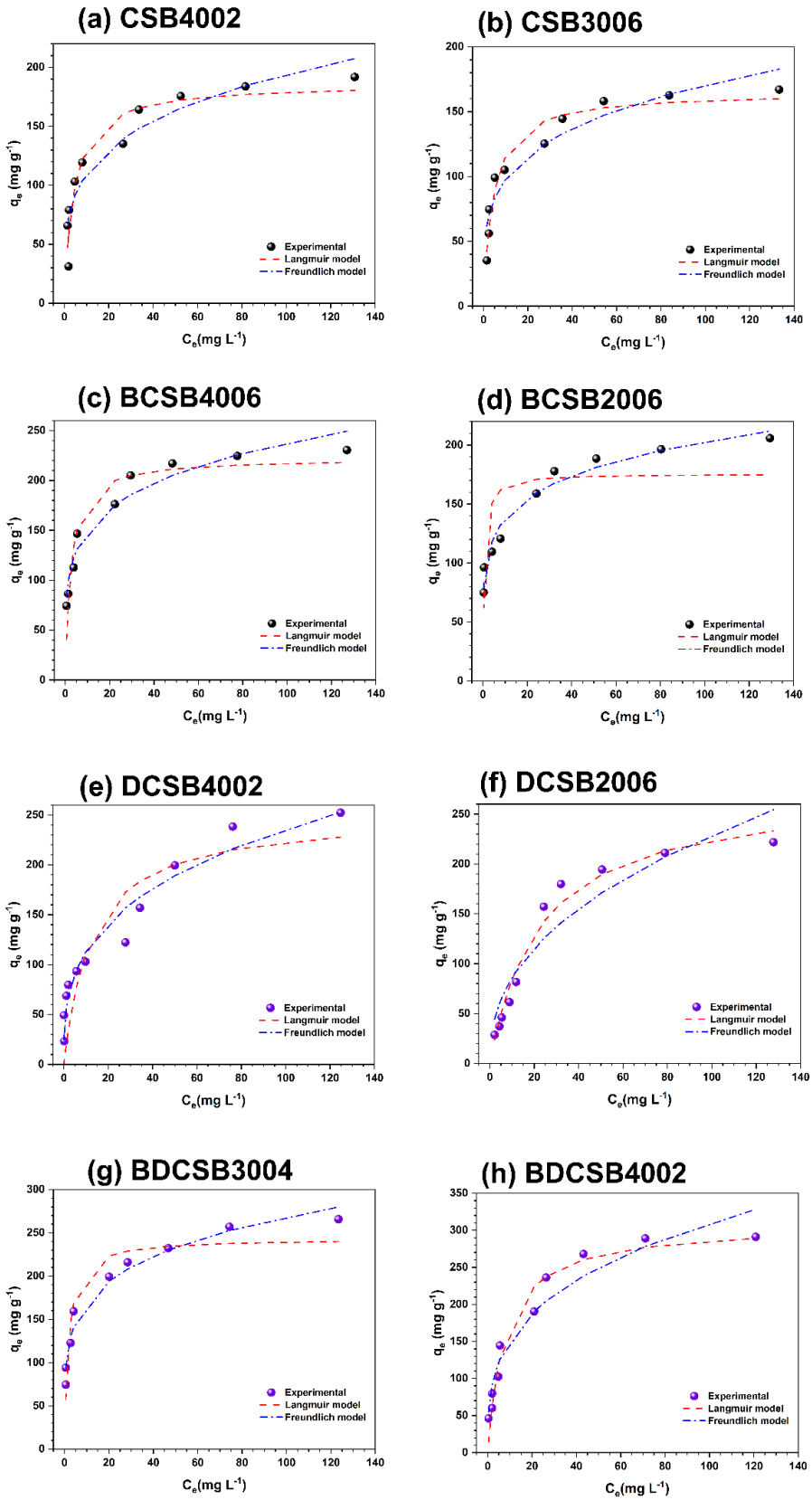

Source: Author

At low concentrations, the excess of active sites limits changes in removal efficiency, whereas at higher concentrations, the increased dye-to-site ratio promotes higher uptake until saturation is approached (Nautiyal; Subramanian; Dastidar, 2016; Shakya; Vithanage; Agarwal, 2022). This behavior is characteristic of L-type isotherms, where high affinity is observed at low concentrations followed by progressive site saturation (Meng *et al.*, 2026). This trend is consistently observed across all panels in Figure 33.

The shape of the isotherms (Figure 33) and the fitted parameters (Table 16) indicate that both Langmuir and Freundlich models can describe the adsorption behavior of the modified materials, although with varying adequacy depending on the sample. For the pristine biochars, the Langmuir model provided the best fit, suggesting predominance of monolayer adsorption on relatively uniform active sites(Coutinho da Silva *et al.*, 2026). In contrast, the modified samples exhibit more variable behavior, reflecting the structural heterogeneity introduced by milling and composite formation.

Table 16 - Equilibrium data for selected samples derived from CSB and DCS

Model Type	Parameter	DCSB4002	DCSB2006	BDCSB3004	BDCSB4002	CSB4002	CSB3006	BCSB2006	BCSB4002
Langmuir	q_m (mg g^{-1})	250.85	274.61	243.51	307.86	186.26	165.12	175.78	222.46
	K_L (L mg^{-1})	0.0795	0.0442	0.5493	0.1273	0.2378	0.2338	1.4871	0.3958
	R^2	0.8	0.977	0.903	0.963	0.918	0.958	0.654	0.917
	R_L	0.077–0.834	0.131–0.900	0.012–0.421	0.050–0.758	0.027–0.627	0.028–0.631	0.004–0.212	0.017–0.503
Freundlich	K_F	54.53	32.19	105.9	73.85	62.02	56.29	93.33	93.66
	n	3.15	2.35	4.96	3.21	4.04	4.15	5.93	4.95
	R^2	0.948	0.894	0.972	0.937	0.899	0.912	0.958	0.951

Source: Author

A more detailed analysis of the isotherm parameters reveals differences in adsorption capacity depending on both the precursor biomass and the modification conditions. For DCSB-derived materials, DCSB2006 and BDCSB4002 showed the highest adsorption capacities (274.61 and 307.86 mg g^{-1}, respectively), approaching the value reported for pristine DCSB (328.13 mg g^{-1}).

For CSB-derived samples, a less consistent trend was observed. Although milling altered adsorption behavior , the maximum capacities for CSB4002 (186.26 mg g^{-1}) and CSB3006 (165.12 mg g^{-1}) remained lower than that of pristine CSB (255.70 mg g^{-1}), indicating that milling alone does not necessarily improve adsorption performance under all conditions. However, the BCC sample BCSB4002 (222.46 mg g^{-1}) showed improved performance compared to its milled counterpart, suggesting that bentonite incorporation may partially compensate for limitations associated with milling alone.

The Freundlich model provided better fits for several modified samples, particularly BCC materials (R^2 up to 0.97), indicating increased surface heterogeneity after modification. Similar behavior has been reported for biochar-based composites, where improved Freundlich fitting is associated with heterogeneous adsorption sites and multilayer interactions(Li, D. *et al.*, 2023; Wei *et al.*, 2020). The Freundlich exponent (n>1 for all samples) confirms favorable adsorption and suggests non-ideal surface behavior(Nascimento *et al.*, 2020).

The combined analysis of dosage, kinetic, and equilibrium results reveals that the modification process leads to a trade-off between adsorption rate and maximum capacity. While modified samples exhibit improved removal efficiency and significantly faster adsorption kinetics, their maximum adsorption capacity (q_m) remains lower than that of pristine biochars.

This behavior may be attributed to structural changes induced during modification, such as pore blockage or alteration of the pore network, which can reduce the accessibility of internal adsorption sites, consequently lowering the maximum adsorption capacity(Fahmi *et al.*, 2018). At the same time, ball milling and composite formation are known to enhance surface area, expose functional groups, and improve adsorbate diffusion, leading to increased adsorption efficiency and faster kinetics(Chauhan *et al.*, 2023). In addition, the introduction of diverse functional groups and adsorption mechanisms contributes to increased surface heterogeneity, as reflected by the better fit of the Freundlich model(Liu, Z. *et al.*, 2022). Therefore, adsorption performance is governed by the interplay between pore structure and surface chemistry(Mao; Liu; Long, 2025).

4.3.3 Proposed adsorption mechanisms

To contextualize the effect of the modification processes, a brief comparison with the pristine biochars is necessary. As previously reported, DCSB exhibited superior adsorption performance toward MB, mainly associated with its higher degree of aromatic condensation and more favorable surface organization, which enhance interactions such as π–π stacking and electrostatic attraction. In contrast, CSB presented lower adsorption efficiency, attributed to its less structured carbon matrix and reduced availability of effective interaction domains(Coutinho da Silva *et al.*, 2026).

The adsorption of MB dye onto the milled biochars and BCC samples is governed by a heterogeneous, multi-site mechanism resulting from the combined effects of HEBM and bentonite incorporation. The integration of structural, chemical, and adsorption data indicates that the system deviates from ideal monolayer behavior and cannot be adequately described by homogeneous adsorption models. A schematic representation of the proposed adsorption mechanisms is presented in Figure 34.

Figure 34 - Proposed adsorption mechanisms

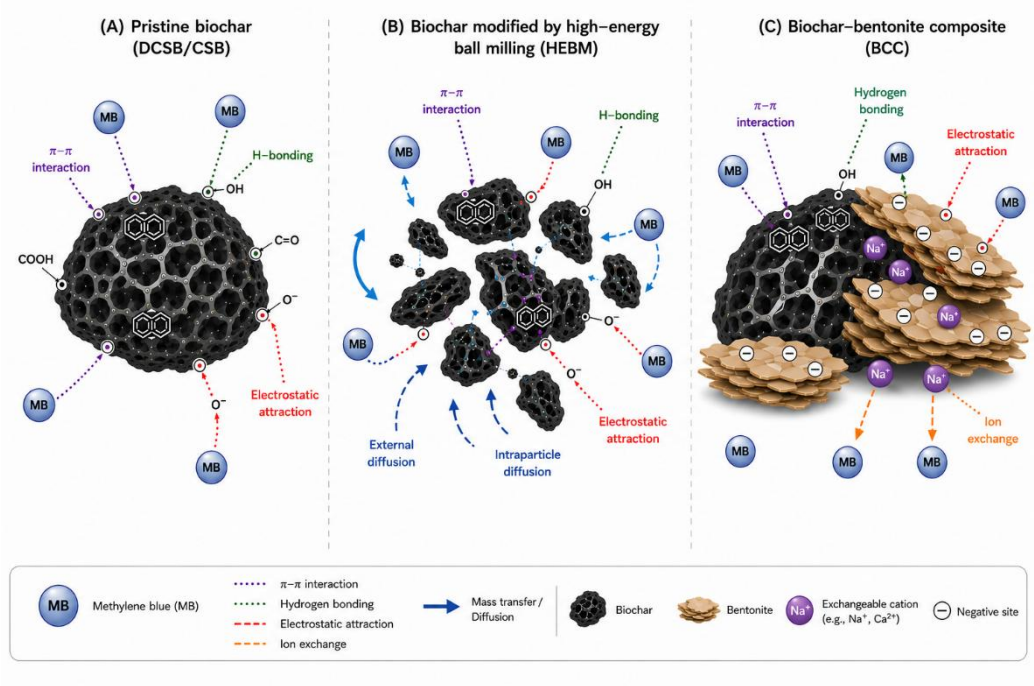

Source: Author

Morphological analysis indicates that HEBM promotes intense particle fragmentation, leading to reduced particle size and increased external surface area, although accompanied by aggregation(Harindintwali *et al.*, 2023; Kovalchuk *et al.*, 2023; Lopez-Tenllado; Motta; Hill, 2021; Ng *et al.*, 2022). This structural modification enhances mass transfer and reduces

diffusion limitations, explaining the significantly faster adsorption kinetics observed for the modified samples(Harindintwali *et al.*, 2023; Nascimento *et al.*, 2020). However, this process may also induce partial pore collapse or blockage, limiting access to internal adsorption sites and contributing to the reduced maximum adsorption capacity observed in some cases(Kovalchuk *et al.*, 2023; Ng *et al.*, 2022).

The kinetic results strongly support a heterogeneous adsorption mechanism. The poor fit of the pseudo-first-order model and the improved performance of the pseudo-second-order model indicate that adsorption is not governed by simple physisorption(Nascimento *et al.*, 2020). More importantly, the excellent fit of the Elovich model confirms that adsorption occurs on energetically heterogeneous surfaces(Nascimento *et al.*, 2020), with a distribution of activation energies. This is further supported by the intraparticle diffusion model, which indicates that adsorption proceeds through multiple steps, including boundary layer diffusion and pore diffusion, rather than a single rate-limiting mechanism(Nascimento *et al.*, 2020).

Equilibrium data reinforce this interpretation. Although the Langmuir model was applied, it does not adequately describe the adsorption behavior of the modified materials. In several cases, the estimated q_m values are lower than those obtained for the unmodified biochars, which is inconsistent with the observed improvements in adsorption kinetics and removal efficiency. This underestimation indicates that the assumptions of the Langmuir model—namely homogeneous surface, identical sites, and monolayer coverage—are not valid for these systems(Nascimento *et al.*, 2020). In contrast, the Freundlich model provides a better fit, indicating adsorption on heterogeneous surfaces with different site energies and the possibility of multilayer interactions. Therefore, the adsorption process is better described as a non-ideal heterogeneous system.

From a chemical standpoint, the preservation of aromatic carbon structures ensures the availability of π-electron-rich domains, which interact with MB through π–π stacking(Ahmad, M. *et al.*, 2014; Tan, I. A. W.; Ahmad; Hameed, 2008). At the same time, oxygen-containing functional groups contribute to hydrogen bonding and electrostatic interactions. The incorporation of bentonite introduces additional Si–O–Si and Al–O groups, increasing the density of negatively charged and polar sites(Akanji *et al.*, 2023). These sites enhance electrostatic attraction toward the cationic dye and may also enable ion-exchange mechanisms, explaining the superior removal efficiencies observed for BCC samples.

XRD analysis indicates that the materials are predominantly amorphous, with turbostratic carbon structures and dispersed mineral phases(Keiluweit *et al.*, 2010; Ng *et al.*,

2022; Ramesh; Raghavan, 2025). The increased structural disorder induced by milling contributes to a greater diversity of adsorption sites, further reinforcing surface heterogeneity.

An additional factor influencing adsorption is the presence of metallic contaminants (Fe, Cr, and Ni), particularly in samples subjected to more intense milling conditions. These elements originate from the wear of stainless steel milling media and introduce additional heterogeneity to the system. Metal species may contribute to adsorption through coordination interactions or by modifying the surface charge(Meng *et al.*, 2026; Wei *et al.*, 2020). However, since their presence is not controlled, their contribution should be interpreted cautiously, as they may introduce variability rather than systematic improvement in adsorption performance.

Thermal analysis supports structural interpretation by indicating increased stability in bentonite-containing samples, suggesting stronger interactions between the mineral and carbon phases. This stabilization may influence the distribution and accessibility of adsorption sites, favoring surface-controlled interactions(WANG; GUO, 2020).

In general, the adsorption mechanism can be described as a combination of electrostatic attraction, π–π interactions, hydrogen bonding, and diffusion-controlled processes occurring on a structurally and energetically heterogeneous surface. The superior performance of BCC samples arises from the synergistic interaction between biochar and bentonite, where the carbon matrix provides aromatic domains for π interactions, while the clay contributes polar and negatively charged sites(Pereira *et al.*, 2020).

In contrast, ball milling alone primarily enhances adsorption kinetics by increasing surface accessibility but does not necessarily improve adsorption capacity, due to competing effects such as pore blockage and structural collapse. Therefore, the adsorption behavior is governed by the balance between surface chemistry, structural accessibility, and heterogeneity, rather than by idealized monolayer adsorption.

5 CONCLUSIONS

This study successfully produced and characterized biochar and biochar–bentonite composites derived from raw and dewaxed carnauba straw via HEBM and demonstrated their potential for MB adsorption from aqueous solutions. The results obtained confirmed that dewaxing, HEBM, and bentonite incorporation significantly influenced the physicochemical properties and adsorption behavior of the produced materials.

RSM screening revealed material-dependent optimal milling conditions: CSB required higher specific energy (26.46 kJ g^{-1}) than DCSB (7.86 kJ g^{-1}), indicating that dewaxing alters mechanochemical susceptibility. Bentonite-containing composites exhibited broader energy tolerance, suggesting a protective role of the clay phase during HEBM. These findings highlight that milling parameters must be optimized on a case-by-case basis.

Adsorption performance was influenced by adsorbent dosage, with removal efficiencies increasing with increasing mass and reaching up to 97.75% (BDCSB4002) and 91.72% (BCSB4006) at 25 mg. At higher dosages, a plateau was observed, indicating reduced utilization of active sites, which is consistent with typical batch adsorption behavior.

Kinetic analysis showed a rapid initial adsorption stage followed by a gradual approach to equilibrium. The modification process significantly increased adsorption rates, with the initial adsorption rate (h) rising from 0.97 mg g^{-1} h^{-1} (CSB) and 6.12 mg g^{-1} h^{-1} (DCSB) to 185.70 mg g^{-1} h^{-1} (BCSB2006) and 250.39 mg g^{-1} h^{-1} (BDCSB3004). Among the evaluated models, the Elovich equation provided the best fit (R^2 up to 0.99), indicating adsorption on energetically heterogeneous surfaces. Intraparticle diffusion analysis suggested that the process occurs through multiple steps rather than a single rate-controlling mechanism.

Equilibrium results showed that adsorption capacity increased with initial MB concentration. The Langmuir model yielded maximum adsorption capacities up to 307.86 mg g^{-1}(BDCSB4002) and 274.61 mg g^{-1} (DCSB2006); however, it did not consistently provide the best fit. The Freundlich model showed higher correlation coefficients for several modified samples (R^2 up to 0.97), indicating heterogeneous adsorption and possible multilayer formation. The Freundlich parameter ($n > 1$) suggests favorable adsorption conditions.

The combined analysis of dosage, kinetic, and equilibrium data indicates that the modification processes affect adsorption behavior in different ways. HEBM contributed primarily to increased adsorption rates, likely due to improved accessibility of adsorption sites, while bentonite incorporation influences removal efficiency and surface heterogeneity. At the

same time, structural changes induced during modification may limit maximum adsorption capacity in some cases.

The adsorption mechanism is consistent with a combination of π–π interactions, electrostatic attraction, hydrogen bonding, and diffusion processes occurring on heterogeneous surfaces(Goswami *et al.*, 2022).

Generally, the results demonstrate that the preparation of biochar–bentonite composites through HEBM is an effective strategy for tailoring the physicochemical and adsorption properties of carnauba-derived biochar, supporting its application as a sustainable adsorbent material for dye-contaminated wastewater treatment.

Furthermore, the valorization of carnauba straw residues into functional adsorbent materials aligns with the principles of circular bioeconomy and contributes to the objectives of Sustainable Development Goals (SDGs) 6 (Clean Water and Sanitation), 12 (Responsible Consumption and Production), and 13 (Climate Action) by promoting water pollution control, waste valorization, and the sustainable utilization of renewable biomass resources.

6 LIMITATIONS AND FUTURE PERSPECTIVES

Despite the comprehensive evaluation of HEBM conditions through response surface methodology (RSM), which allowed the identification of optimal operational parameters and demonstrated the strong influence of milling on adsorption performance, some limitations should be acknowledged.

The absence of textural characterization by N_2 adsorption–desorption (BET analysis) limits a more detailed correlation between surface area, pore structure, and adsorption capacity. Although the RSM results clearly indicate that milling enhances adsorption—mainly through particle size reduction and increased accessibility—the lack of quantitative porosity data prevents a deeper understanding of the balance between pore development and possible pore blockage or aggregation effects induced at higher milling energies.

Additionally, the HEBM produced very fine biochar particles, which posed a challenge for solid–liquid separation after adsorption. Although centrifugation was employed, some supernatants remained slightly turbid, potentially interfering with UV–Vis absorbance readings. Furthermore, for more concentrated methylene blue solutions, the absorbance exceeded the reliable detection limit (absorbance > 2), requiring dilution of the samples before measurement. This procedural step, while necessary, may introduce additional uncertainty into the concentration determinations.

Moreover, adsorption assays with the pristine bentonite could not be performed to evaluate potential synergistic effects with biochar due to a significant hypsochromic shift (blue shift) of the maximum absorption wavelength of methylene blue from ~664 nm to ~568 nm in the presence of the clay. This spectral change, likely caused by molecular aggregation or metachromatic effects induced by the clay surface, prevented reliable quantification of the dye concentration by UV–Vis spectrophotometry at the standard wavelength.

In addition, the influence of solution pH was not systematically investigated. Since pH directly affects surface charge, ionization of functional groups, and the speciation of MB, its evaluation would provide further insight into the relative contribution of electrostatic interactions in the proposed mechanism.

Thermodynamic parameters were also not determined, limiting the evaluation of the spontaneity and energetic nature of the adsorption process. While kinetic and equilibrium analyses indicate a heterogeneous mechanism, the absence of thermodynamic data restricts a more complete physicochemical interpretation.

Although the adsorption results clearly indicate heterogeneous behavior—well described by the Freundlich and Elovich models—advanced isotherm models that account for heterogeneity (such as Sips, Redlich–Peterson, or Toth) were not applied. Consequently, the maximum adsorption capacities derived from the Langmuir model may be underestimated and should be interpreted cautiously.

Another important aspect is the presence of metallic contaminants (Fe, Cr, and Ni) originating from the stainless steel milling media in some samples. While their detection provides valuable insight into mechanochemical effects, their uncontrolled incorporation introduces uncertainty regarding their exact role in adsorption and may contribute to variability among samples.

Future studies should therefore focus on integrating textural analysis (BET), pH-dependent adsorption experiments, and thermodynamic evaluation to provide a more complete description of the adsorption process. The application of heterogeneous isotherm models would allow a more accurate estimation of adsorption capacity and improve the interpretation of equilibrium data.

Additionally, further investigations under more realistic conditions are recommended, including the use of multicomponent systems, real wastewater matrices, and varying ionic strengths. Studies on adsorbent regeneration and reuse are also essential to assess long-term performance and economic feasibility.

Finally, studies on the reusability and regeneration of the developed adsorbents under continuous flow conditions are recommended to evaluate their practical feasibility for large-scale wastewater treatment applications.

REFERENCES

ABIN-BAZAINE, A. *et al.* Adsorption Isotherms: Enlightenment of the Phenomenon of Adsorption. *Wastewater Treatment*, 19 abr. 2022. Disponível em: https://www.intechopen.com/chapters/81400. Acesso em: 23 ago. 2025.

AHMAD, A. *et al.* Removal of methylene blue dye using rice husk, cow dung and sludge biochar: Characterization, application, and kinetic studies. *Bioresource Technology*, v. 306, p. 123202, 1 jun. 2020. Disponível em: https://www.sciencedirect.com/science/article/pii/S0960852420304739. Acesso em: 24 ago. 2025.

AHMAD, M. *et al.* Biochar as a sorbent for contaminant management in soil and water: A review. *Chemosphere*, v. 99, p. 19–33, mar. 2014. Disponível em: https://linkinghub.elsevier.com/retrieve/pii/S0045653513015051. Acesso em: 22 fev. 2026.

AKANJI, M. A. *et al.* Synthesis and Characterization of Clay-Biochar Composites. In: VITHANAGE, M.; LAZZARA, G.; RAJAPAKSHA, A. U. R. (Org.). *Clay Composites: Environmental Applications*. Singapore: Springer, 2023. p. 91–112. Disponível em: https://link.springer.com/chapter/10.1007/978-981-99-2544-5_5. Acesso em: 11 ago. 2025.

AL-RUMAIHI, A. *et al.* A review of pyrolysis technologies and feedstock: A blending approach for plastic and biomass towards optimum biochar yield. *Renewable and Sustainable Energy Reviews*, v. 167, p. 112715, 1 out. 2022. Disponível em: https://www.sciencedirect.com/science/article/pii/S1364032122006049. Acesso em: 15 ago. 2025.

ALVES, M. O.; COÊLHO, J. D. *Extrativismo da Carnaúba: Relações de Produção, Tecnologia e Mercado*. 1. ed. Fortaleza: Banco do Nordeste do Brasil, 2008. v. 20. Disponível em: https://www.bnb.gov.br/s482-dspace/bitstream/123456789/784/1/2008_ART_Alves.pdf. Acesso em: 8 ago. 2025.

AMALINA, F. *et al.* A comprehensive assessment of the method for producing biochar, its characterization, stability, and potential applications in regenerative economic sustainability – A review. *Cleaner Materials*, v. 3, p. 100045, 1 mar. 2022. Disponível em: https://www.sciencedirect.com/science/article/pii/S2772397622000053. Acesso em: 25 ago. 2025.

AMERICAN SOCIETY FOR TESTING AND MATERIALS. *Practice for Preparation of Biomass for Compositional Analysis*. West Conshohocken, PA: ASTM International. Disponível em: http://www.astm.org/cgi-bin/resolver.cgi?E1757-01R15. Acesso em: 28 ago. 2025.

AMERICAN SOCIETY FOR TESTING AND MATERIALS. *Test Method for Ash in Biomass*. West Conshohocken, PA: ASTM International. Disponível em: http://www.astm.org/cgi-bin/resolver.cgi?E1755-01. Acesso em: 28 ago. 2025.

AMERICAN SOCIETY FOR TESTING AND MATERIALS. *Test Method for Moisture in the Analysis Sample of Coal and Coke*. West Conshohocken, PA: ASTM International. Disponível em: http://www.astm.org/cgi-bin/resolver.cgi?D3173-11. Acesso em: 28 ago. 2025.

AMERICAN SOCIETY FOR TESTING AND MATERIALS. *Test Method for Volatile Matter in the Analysis of Particulate Wood Fuels*. West Conshohocken, PA: ASTM International. Disponível em: http://www.astm.org/cgi-bin/resolver.cgi?E872-82R19. Acesso em: 28 ago. 2025.

AMIN, F. R. *et al.* Biochar applications and modern techniques for characterization. *Clean Technologies and Environmental Policy*, v. 18, n. 5, p. 1457–1473, 1 jun. 2016. Disponível em: https://link.springer.com/article/10.1007/s10098-016-1218-8. Acesso em: 25 ago. 2025.

ARIF, M. *et al.* Synthesis, characteristics and mechanistic insight into the clays and clay minerals-biochar surface interactions for contaminants removal-A review. *Journal of Cleaner Production*, v. 310, p. 127548, 10 ago. 2021. Disponível em: https://www.sciencedirect.com/science/article/pii/S0959652621017662. Acesso em: 25 ago. 2025.

AWASTHI, M. K. *et al.* Refining biomass residues for sustainable energy and bio-products: An assessment of technology, its importance, and strategic applications in circular bio-economy. *Renewable & Sustainable Energy Reviews*, v. 127, p. 109876, 1 jul. 2020. Disponível em: https://experts.esf.edu/esploro/outputs/journalArticle/Refining-biomass-residues-for-sustainable-energy/99952181904826. Acesso em: 5 jun. 2026.

BAO, Z. *et al.* Recent developments in modification of biochar and its application in soil pollution control and ecoregulation. *Environmental Pollution*, v. 313, p. 120184, 15 nov. 2022. Disponível em: https://www.sciencedirect.com/science/article/pii/S0269749122013987. Acesso em: 28 ago. 2025.

BLUE rivers and water as strong as bleach: The ‘destructive’ impact of fast fashion in Africa. *Euronews*. Disponível em: https://www.euronews.com/green/2021/08/19/blue-rivers-and-water-as-strong-as-bleach-the-destructive-impact-of-fast-fashion-in-africa. Acesso em: 5 fev. 2026.

BUJDÁK, J. Adsorption kinetics models in clay systems. The critical analysis of pseudo-second order mechanism. *Applied Clay Science*, v. 191, p. 105630, 15 jun. 2020. Disponível em: https://www.sciencedirect.com/science/article/pii/S0169131720301952. Acesso em: 24 ago. 2025.

CAI, F. *et al.* Preparation of nitrogen-doped bagasse-derived biochar with outstanding methylene blue adsorption performance. *Industrial Crops and Products*, v. 224, p. 120415, 1 fev. 2025. Disponível em: https://www.sciencedirect.com/science/article/pii/S0926669024023926. Acesso em: 24 ago. 2025.

CĂLIN, C. *et al.* A Thermogravimetric Analysis of Biomass Conversion to Biochar: Experimental and Kinetic Modeling. *Applied Sciences,* v. 14, n. 21, 27 out. 2024. Disponível em: https://www.mdpi.com/2076-3417/14/21/9856. Acesso em: 25 abr. 2026.

CHANDRARATNE, M. R. *et al.* Recent Advances in Thermochemical Conversion of Biomass. In: *Recent Perspectives in Pyrolysis Research*. London: IntechOpen, 21 set. 2021. Disponível em: https://www.intechopen.com/chapters/78641. Acesso em: 14 ago. 2025.

CHAUDHARY, H.; DINAKARAN, J.; RAO, K. S. Comparative analysis of biochar production methods and their impacts on biochar physico-chemical properties and adsorption of heavy metals. *Journal of Environmental Chemical Engineering*, v. 12, n. 3, p. 113003, 1 jun. 2024. Disponível em: https://www.sciencedirect.com/science/article/pii/S2213343724011333. Acesso em: 4 jun. 2026.

CHAUHAN, S. *et al.* Biochar-mediated removal of pharmaceutical compounds from aqueous matrices via adsorption. *Waste Disposal & Sustainable Energy*, v. 5, n. 1, p. 37–62, 16 mar. 2023.

CHEN, D.; ZHOU, J.; ZHANG, Q. Effects of heating rate on slow pyrolysis behavior, kinetic parameters and products properties of moso bamboo. *Bioresource Technology*, v. 169, p. 313–319, 1 out. 2014. Disponível em: https://www.sciencedirect.com/science/article/pii/S0960852414009742. Acesso em: 25 abr. 2026.

CHEN, S. *et al.* Research on mechanical-activated nanoscale bentonite and surface aging behavior of its modified asphalt. *Construction and Building Materials*, v. 321, p. 126356, 28 fev. 2022. Disponível em: https://www.sciencedirect.com/science/article/pii/S0950061822000502. Acesso em: 26 abr. 2026.

CHISTIE, S. M. *et al.* Production and characterization of magnetic Biochar derived from pyrolysis of waste areca nut husk for removal of methylene blue dye from wastewater. *Scientific Reports*, v. 15, n. 1, p. 23209, 2 jul. 2025. Disponível em: https://www.nature.com/articles/s41598-025-03359-z. Acesso em: 26 nov. 2025.

COUTINHO DA SILVA, L. *et al.* Production and Characterization of Carnauba Straw (Copernicia prunifera) Biochar: Influence of Wax Removal on Adsorption of Methylene Blue. *ACS Omega*, v. 11, n. 16, p. 24522–24535, 28 abr. 2026. Disponível em: https://pubs.acs.org/doi/10.1021/acsomega.6c00684. Acesso em: 13 abr. 2026.

DA SILVA, E. O. *et al.* Removal of methylene blue from aqueous solution by ryegrass straw. *International Journal of Environmental Science and Technology,* v. 17, n. 8, p. 3723–3740, 11 jun. 2020. Disponível em: https://link.springer.com/article/10.1007/s13762-020-02718-9. Acesso em: 24 ago. 2025.

DA SILVA, N. E. P. *et al.* Coconut shell-based biochars produced by an innovative thermochemical process for obtaining improved lignocellulose-based adsorbents. *International Journal of Biological Macromolecules*, v. 275, p. 133685, 1 ago. 2024. Disponível em: https://www.sciencedirect.com/science/article/pii/S0141813024044908. Acesso em: 4 jun. 2026.

DA SILVA NETO, L. D. *et al.* Application of Clay-Biochar Composites as Adsorbents for Water Treatment. In: VITHANAGE, M; LAZZARA, G.; RAJAPAKSHA, A. U. (Org.). *Clay Composites: Environmental Applications*. Singapore: Springer, 2023. p. 113–142. Disponível em: https://link.springer.com/chapter/10.1007/978-981-99-2544-5_6. Acesso em: 21 ago. 2025.

DAI, L. *et al.* A review on selective production of value-added chemicals via catalytic pyrolysis of lignocellulosic biomass. *Science of The Total Environment*, v. 749, p. 142386, 20 dez. 2020. Disponível em: https://www.sciencedirect.com/science/article/pii/S0048969720359155. Acesso em: 11 ago. 2025.

DAOU, I. *et al.* Adsorption of methyl orange and methylene blue from aqueous solutions on pure bentonite: statistical physical modeling provides an analytical interpretation. *Environmental Monitoring and Assessment*, v. 196, n. 11, p. 1–22, 1 nov. 2024. Disponível em: https://link.springer.com/article/10.1007/s10661-024-13239-0. Acesso em: 24 ago. 2025.

DELLISANTI, F.; VALDRÉ, G. Study of structural properties of ion treated and mechanically deformed commercial bentonite. *Applied Clay Science*, v. 28, n. 1–4, p. 233–244, 1 jan. 2005. Disponível em: https://www.sciencedirect.com/science/article/pii/S0169131704000821. Acesso em: 21 ago. 2025.

EARLE, S. Clay Minerals. *Environmental Geology*. 1. ed. Kamloops: Thompson River University, [S.d.]. Disponível em: https://environmental-geology-dev.pressbooks.tru.ca/chapter/clay-minerals/. Acesso em: 17 ago. 2025.

ESTEVES, B.; SEN, U.; PEREIRA, H. Influence of Chemical Composition on Heating Value of Biomass: A Review and Bibliometric Analysis. *Energies,* v. 16, n. 10, p. 4226, 20 maio 2023. Disponível em: https://www.mdpi.com/1996-1073/16/10/4226/htm. Acesso em: 14 ago. 2025.

FAHMI, A. H. *et al.* Physical modification of biochar to expose the inner pores and their functional groups to enhance lead adsorption. *RSC Advances*, v. 8, n. 67, p. 38270–38280,14 nov. 2018. Disponível em: https://pubs.rsc.org/en/content/articlelanding/2018/ra/c8ra06867d. Acesso em: 14 ago. 2025

FAHMY, T. Y. A. *et al.* Biomass pyrolysis: past, present, and future. *Environment, Development and Sustainability*, v. 22, n. 1, p. 17–32, 1 jan. 2020. Disponível em: https://link.springer.com/article/10.1007/s10668-018-0200-5. Acesso em: 10 ago. 2025.

FERNANDES, J. E. *et al.* Carnauba straw: Characterization and chemical treatments. *Journal of Applied Polymer Science*, v. 122, n. 3, p. 1614–1621, 5 nov. 2011. Disponível em: https://onlinelibrary.wiley.com/doi/10.1002/app.33882. Acesso em: 9 ago. 2025.

FERRAZ, D.; PYKA, A. Circular economy, bioeconomy, and sustainable development goals: a systematic literature review. *Environmental Science and Pollution Research*, 13 set. 2023. Disponível em: https://link.springer.com/article/10.1007/s11356-023-29632-0. Acesso em: 5 jun. 2026.

FERREIRA DA SILVA, A. J. *et al.* Copper removal using carnauba straw powder: Equilibrium, kinetics, and thermodynamic studies. *Journal of Environmental Chemical Engineering*, v. 6, n. 6, p. 6828–6835, 1 dez. 2018. Disponível em: https://www.sciencedirect.com/science/article/pii/S2213343718306365. Acesso em: 9 ago. 2025.

GAO, L.; GOLDFARB, J. L. Characterization and adsorption applications of composite biochars of clay minerals and biomass. *Environmental Science and Pollution Research*, v. 28, n. 32, p. 44277–44287, 13 ago. 2021. Disponível em: https://link.springer.com/10.1007/s11356-021-13858-x. Acesso em: 23 fev. 2026.

GOES, M. C. C. *et al.* Expressive Removal of Cationic Dyes (Methylene Blue and Crystal Violet) by Carnauba Straw (Copernicia cerifera). *The Pharmaceutical and Chemical Journal*, v. 3, n. 6, p. 37–52, 5 jul. 2019. Disponível em: https://tpcj.org/download/vol-6-iss-3-2019/TPCJ2019-06-03-37-52.pdf. Acesso em: 9 ago. 2025.

GONÇALVES, F. *et al.* Effect of Carnaúba Bagana Mulching on Tree Species Planted in Degraded Areas in Caatinga. *Floresta e Ambiente*, v. 30, n. 3, p. e20220091, 27 nov. 2023. Disponível em: https://www.scielo.br/j/floram/a/6ZyGj3MfXhkv8Twj6c8MCtG/. Acesso em: 9 ago. 2025.

GOSWAMI, L. *et al.* Surface Modification of Biochar for Dye Removal from Wastewater. *Catalysts 2022, Vol. 12,* v. 12, n. 8, 25 jul. 2022a. Disponível em: https://www.mdpi.com/2073-4344/12/8/817. Acesso em: 26 abr. 2026.

HAMAD, H. N. *et al.* Optimized Bentonite Clay Adsorbents for Methylene Blue Removal. *Processes*, v. 12, n. 4, p. 738, 1 abr. 2024. Disponível em: https://www.mdpi.com/2227-9717/12/4/738/htm. Acesso em: 24 ago. 2025.

HAMZAOUI, R. *et al.* Structural and thermal behavior of proclay kaolinite using high energy ball milling process. *Powder Technology*, v. 271, p. 228–237, fev. 2015. Disponível em: https://www.sciencedirect.com/science/article/pii/S0032591014009164. Acesso em: 13 mar. 2026.

HARINDINTWALI, J. D. *et al.* Effects of ball milling on biochar adsorption of contaminants in water: A meta-analysis. *Science of The Total Environment*, v. 882, p. 163643, 15 jul. 2023. Disponível em: https://linkinghub.elsevier.com/retrieve/pii/S0048969723022635. Acesso em: 12 mar. 2026.

IGALAVITHANA, A. D. *et al.* Advances and future directions of biochar characterization methods and applications. *Critical Reviews in Environmental Science and Technology*, v. 47, n. 23, p. 2275–2330, 2 dez. 2017. Disponível em: https://www.tandfonline.com/doi/abs/10.1080/10643389.2017.1421844. Acesso em: 25 ago. 2025.

INSTITUTO BRASILEIRO DE GEOGRAFIA E ESTATÍSTICA. *Produção da Extração Vegetal e da Silvicultura*. Rio de Janeiro: [s.n.], 2023. Disponível em: https://www.ibge.gov.br/estatisticas/economicas/agricultura-e-pecuaria/9105-producao-da-extracao-vegetal-e-da-silvicultura.html?edicao=41394. Acesso em: 8 ago. 2025.

INTERNATIONAL BIOCHAR INITIATIVE. *Standardized Product Definition and Product Testing Guidelines for Biochar That Is Used in Soil (aka IBI Biochar Standards)*. [S.l: s.n.], 23 nov. 2015. Disponível em: http://www.biochar-international.org/characterizationstandard. Acesso em: 10 ago. 2025.

JIANG, F. *et al.* Remarkable synergy between sawdust biochar and attapulgite/diatomite after co-ball milling to adsorb methylene blue. *RSC Advances*, v. 13, n. 21, p. 14384–14392, 9 maio 2023. Disponível em: https://pubs.rsc.org/en/content/articlehtml/2023/ra/d3ra01123b. Acesso em: 28 ago. 2025.

JUNIO, R. F. *et al.* Carnauba leaf fibers: correlation among diametrical variation, physical and mechanical properties. *Journal of Materials Research and Technology*, v. 22, p. 1888–1899, 1 jan. 2023. Disponível em: https://www.sciencedirect.com/science/article/pii/S2238785422019573. Acesso em: 9 ago. 2025.

JUNIO, R. F. *et al.* Thermochemical and structural characterization of promising carnauba novel leaf fiber (Copernicia prunifera). *Journal of Materials Research and Technology*, v. 18, p. 4714–4723, 1 maio 2022. Disponível em: https://www.sciencedirect.com/science/article/pii/S2238785422006275. Acesso em: 9 ago. 2025.

KAMBO, H. S.; DUTTA, A. A comparative review of biochar and hydrochar in terms of production, physico-chemical properties and applications. *Renewable and Sustainable Energy Reviews*, v. 45, p. 359–378, 1 maio 2015. Disponível em: https://www.sciencedirect.com/science/article/pii/S136403211500060X. Acesso em: 11 ago. 2025.

KEILUWEIT, M. *et al.* Dynamic Molecular Structure of Plant Biomass-Derived Black Carbon (Biochar). *Environmental Science and Technology*, v. 44, n. 4, p. 1247–1253, 2010. Disponível em: https://pubs.acs.org/doi/abs/10.1021/es9031419. Acesso em: 26 abr. 2026.

KHAN, I. *et al.* Review on Methylene Blue: Its Properties, Uses, Toxicity and Photodegradation. *Water*, v. 14, n. 2, p. 242, 14 jan. 2022. Disponível em: https://www.mdpi.com/2073-4441/14/2/242/htm. Acesso em: 24 ago. 2025.

KOVALCHUK, I. *et al.* The Effect of High-Energy Ball Milling of Montmorillonite for Adsorptive Removal of Cesium, Strontium, and Uranium Ions from Aqueous Solution. *Eng*, v. 4, n. 4, p. 2812–2825, 14 nov. 2023. Disponível em: https://www.mdpi.com/2673-4117/4/4/158/htm. Acesso em: 21 ago. 2025.

KUMAR, M. *et al.* Ball milling as a mechanochemical technology for fabrication of novel biochar nanomaterials. *Bioresource Technology*, v. 312, p. 123613, 1 set. 2020. Disponível em: https://www.sciencedirect.com/science/article/pii/S0960852420308853. Acesso em: 19 ago. 2025.

KUMARI, N.; MOHAN, C. Basics of Clay Minerals and Their Characteristic Properties. In: NASCIMENTO, G. M. DO (Org.). *Clay and Clay Minerals*. 1. ed. London: IntechOpen, 2021. v. 1.

LEHMANN, J.; JOSEPH, S. *Biochar for Environmental Management*. London: Routledge, 2015. Disponível em: https://www.taylorfrancis.com/books/9781134489534. Acesso em: 11 ago. 2025.

LENG, L. *et al.* Biochar stability assessment methods: A review. *Science of The Total Environment*, v. 647, p. 210–222, 10 jan. 2019. Disponível em: https://www.sciencedirect.com/science/article/pii/S0048969718328997. Acesso em: 25 abr. 2026.

LEONEL, E. C. *et al.* Effect of high-energy ball milling in the structural and textural properties of kaolinite. *Cerâmica*, v. 60, n. 354, p. 267–272, 2014. Disponível em: https://www.scielo.br/j/ce/a/rx5qmjgtvNkGshMXdTp4CHx. Acesso em: 19 ago. 2025.

LI, D. *et al.* Ball-milled magnetic sludge biochar enables fast aerobic granulation in anoxic/oxic process for the treatment of coal chemical wastewater. *Science of The Total Environment*, v. 880, p. 163241, 1 jul. 2023. Disponível em: https://www.sciencedirect.com/science/article/pii/S0048969723018600. Acesso em: 22 abr. 2026.

LI, H. *et al.* Mechanisms and adsorption capacities of ball milled biomass fly ash/biochar composites for the adsorption of methylene blue dye from aqueous solution. *Journal of Water Process Engineering*, v. 53, p. 103713, 1 jul. 2023. Disponível em: https://www.sciencedirect.com/science/article/pii/S2214714423002325. Acesso em: 3 abr. 2026.

LIN, M. *et al.* Biochar-clay, biochar-microorganism and biochar-enzyme composites for environmental remediation: a review. *Environmental Chemistry Letters*, v. 21, n. 3, p. 1837–1862, 14 mar. 2023. Disponível em: https://link.springer.com/article/10.1007/s10311-023-01582-6. Acesso em: 25 ago. 2025.

LIU, L. *et al.* Enhanced anaerobic co-digestion under a magnetic field by a synergistic host–guest strategy: Focusing on accelerant, biogas yield, fertilization and coupled effect. *Chemical Engineering Journal*, v. 476, p. 146508, 15 nov. 2023. Disponível em: https://www.sciencedirect.com/science/article/pii/S1385894723052397. Acesso em: 25 abr. 2026.

LIU, Z. *et al.* Modified biochar: synthesis and mechanism for removal of environmental heavy metals. *Carbon Research,* v. 1, n. 1, p. 8-, 18 jun. 2022. Disponível em: https://link.springer.com/article/10.1007/s44246-022-00007-3. Acesso em: 23 abr. 2026.

LOPEZ-TENLLADO, F. J.; MOTTA, I. L.; HILL, J. M. Modification of biochar with high-energy ball milling: Development of porosity and surface acid functional groups. *Bioresource Technology Reports*, v. 15, p. 100704, 1 set. 2021. Disponível em: https://www.sciencedirect.com/science/article/pii/S2589014X21000815. Acesso em: 21 ago. 2025.

MANDZHIEVA, S. *et al.* Preparation and Modification of Rape Straw Biochar and Its Adsorption Characteristics for Methylene Blue in Water. *Water 2022, Vol. 14, Page 3761*, v. 14, n. 22, p. 3761, 19 nov. 2022. Disponível em: https://www.mdpi.com/2073-4441/14/22/3761/htm. Acesso em: 24 ago. 2025.

MAO, X.; LIU, Y.; LONG, S. Research progress on adsorption mechanisms and regeneration applications of modified biochar for heavy metals in wastewater. *Desalination and Water Treatment*, v. 324, p. 101399, 1 out. 2025. Disponível em: https://www.sciencedirect.com/science/article/pii/S1944398625004151. Acesso em: 23 abr. 2026.

MAROUF, R. *et al.* Study of Adsorption Properties of Bentonite Clay. *Montmorillonite Clay*, 14 dez. 2021. Disponível em: https://www.intechopen.com/chapters/75461. Acesso em: 19 ago. 2025.

MARSH, A. T. M. *et al.* Relationships between milling input energy and chemical reactivity for mechanochemical activation of clays. *RSC Mechanochemistry*, v. 3, n. 2, p. 201–212, 10 mar. 2026. Disponível em: https://pubs.rsc.org/en/content/articlehtml/2026/mr/d5mr00088b. Acesso em: 26 abr. 2026.

MELO, A. L. F. C. *et al.* Using Activated Biochar from Caryocar brasiliense Pequi Almonds for Removing Methylene Blue Dye in an Aqueous Solution. *Water,* v. 15, n. 22, p. 4006, 17 nov. 2023. Disponível em: https://www.mdpi.com/2073-4441/15/22/4006/htm. Acesso em: 24 ago. 2025.

MENG, X. *et al.* Efficient Phosphate Adsorption by Ball-Milled Fe3O4–Modified Biochar Derived from Agricultural Waste. *ACS Omega*, v. 11, n. 7, p. 11094–11103, 24 fev. 2026. Disponível em: https://pubs.acs.org/doi/10.1021/acsomega.5c03908. Acesso em: 22 abr. 2026.

METHYLENE blue. *American Chemical Society,* 14 jun. 2011. Disponível em: https://www.acs.org/molecule-of-the-week/archive/m/methylene-blue.html. Acesso em: 24 ago. 2025.

NASCIMENTO, R. F. *et al. Adsorção: Aspectos teóricos e aplicações ambientais*. . Fortaleza: [s.n.], 2020.

NASCIMENTO, R. F.; NETO, V. DE O. *Uso de bioadsorventes lignocelulósicos na remoção de poluentes de efluentes aquosos*. 1. ed. Fortaleza: Imprensa Universitária, 2014.

NAUTIYAL, P.; SUBRAMANIAN, K. A.; DASTIDAR, M. G. Adsorptive removal of dye using biochar derived from residual algae after in-situ transesterification: Alternate use of waste of biodiesel industry. *Journal of Environmental Management*, v. 182, p. 187–197, 1 nov. 2016. Disponível em: https://linkinghub.elsevier.com/retrieve/pii/S030147971630500X. Acesso em: 28 nov. 2025.

NG, L. Y. F. *et al.* High-Energy Ball Milling for High Productivity of Nanobiochar from Oil Palm Biomass. *Nanomaterials*, v. 12, n. 18, p. 3251, 19 set. 2022. Disponível em: https://www.mdpi.com/2079-4991/12/18/3251. Acesso em: 21 ago. 2025.

NOBLE, R. D.; TERRY, P. A. Adsorption. *Principles of Chemical Separations with Environmental Applications*. 1. ed. Cambridge: Cambridge University Press, 2004. v. 1. p. 182–213. Disponível em: https://www.cambridge.org/core/product/identifier/CBO9780511616594A078. Acesso em: 21 ago. 2025.

NUNES, F. C. *et al.* Clay Composites: Physicochemical Characterization. In: VITHANAGE, METHTHIKA; LAZZARA, G.; RAJAPAKSHA, A. U. (Org.). *Clay Composites: Environmental Applications*. 1. ed. Singapore: Springer, 2023.

OLADOYE, P. O. *et al.* Methylene blue dye: Toxicity and potential elimination technology from wastewater. *Results in Engineering*, v. 16, p. 100678, 1 dez. 2022. Disponível em: https://www.sciencedirect.com/science/article/pii/S2590123022003486. Acesso em: 24 ago. 2025.

OUR colorful clothes are killing the environment. *CNN*, 28 set. 2020. Disponível em: https://edition.cnn.com/style/article/dyeing-pollution-fashion-intl-hnk-dst-sept. Acesso em: 5 fev. 2026.

PAN, T. *et al.* Preparation and characterization of calcite/biochar composites fabricated by co-pyrolysis technique. *International Journal of Electrochemical Science*, v. 19, n. 5, p. 100554, maio 2024. Disponível em: https://linkinghub.elsevier.com/retrieve/pii/S1452398124000956. Acesso em: 20 ago. 2025.

PEREIRA, J. E. S. *et al.* Carnauba straw powder treated with bentonite for copper adsorption in aqueous solution: isothermal, kinetic and thermodynamic study. *Water Science and Technology*, v. 82, n. 10, p. 2178–2192, 15 nov. 2020. Disponível em: http://iwaponline.com/wst/article-pdf/82/10/2178/789730/wst082102178.pdf. Acesso em: 9 ago. 2025.

PEREIRA, J. E. S. *et al.* Valorization of carnauba straw and cashew leaf as bioadsorbents to remove copper (II) ions from aqueous solution. *Environmental Technology & Innovation*, v. 23, p. 101706, 1 ago. 2021. Disponível em: https://www.sciencedirect.com/science/article/pii/S2352186421003540. Acesso em: 9 ago. 2025.

POURHAKKAK, P. *et al.* Adsorbent. *Interface Science and Technology*. [S.l.]: Elsevier, 2021. v. 33. p. 71–210. Disponível em: https://linkinghub.elsevier.com/retrieve/pii/B9780128188057000096. Acesso em: 19 ago. 2025.

QIN, F. *et al.* Lignocellulosic biomass carbonization for biochar production and characterization of biochar reactivity. *Renewable and Sustainable Energy Reviews*, v. 157, p. 112056, 1 abr. 2022. Disponível em: https://www.sciencedirect.com/science/article/pii/S1364032121013186. Acesso em: 10 ago. 2025.

RAMESH, K.; RAGHAVAN, V. Biochar/bentonite composite beads for controlled nitrogen release and reduced environmental impact: From banana waste to sustainable food security. *Results in Surfaces and Interfaces*, v. 19, p. 100500, maio 2025. Disponível em: https://linkinghub.elsevier.com/retrieve/pii/S266684592500087X Acesso em: 20 ago.2025.

RAMOLA, S. *et al.* Improved lead removal from aqueous solution using novel porous bentonite - and calcite-biochar composite. *Science of The Total Environment*, v. 709, p. 136171, 20 mar. 2020. Disponível em: https://linkinghub.elsevier.com/retrieve/pii/S0048969719361674. Acesso em: 3 jan. 2026.

REVELLAME, E. D. *et al.* Adsorption kinetic modeling using pseudo-first order and pseudo-second order rate laws: A review. *Cleaner Engineering and Technology*, v. 1, p. 100032, 1 dez. 2020. Disponível em: https://www.sciencedirect.com/science/article/pii/S266679082030032X. Acesso em: 24 ago. 2025.

SAMPAIO, T. Q. S.; LIMA, S. B.; PIRES, C. A. M. Influence of extractives on the composition of bio-oil from biomass pyrolysis – A review. *Journal of Analytical and Applied Pyrolysis*, v. 186, p. 106919, 1 mar. 2025. Disponível em: https://www.sciencedirect.com/science/article/pii/S0165237024005746. Acesso em: 14 ago. 2025.

SCHMIDT, H. P. *et al. Guidelines for a Sustainable Production of Biochar*. . Frick: [s.n.], 20 dez. 2024. Disponível em: https://www.european-biochar.org. Acesso em: 15 ago. 2025.

SEOW, Y. X. *et al.* A review on biochar production from different biomass wastes by recent carbonization technologies and its sustainable applications. *Journal of Environmental Chemical Engineering*, v. 10, n. 1, p. 107017, 1 fev. 2022. Disponível em: https://www.sciencedirect.com/science/article/pii/S2213343721019941. Acesso em: 11 ago. 2025.

SEWU, D. D. *et al.* Effect of bentonite-mineral co-pyrolysis with macroalgae on physicochemical property and dye uptake capacity of bentonite/biochar composite. *Journal of the Taiwan Institute of Chemical Engineers*, v. 104, p. 106–113, 1 nov. 2019. Disponível em: https://linkinghub.elsevier.com/retrieve/pii/S1876107019303360. Acesso em: 3 jan. 2026.

SHAH, S. W. A. *et al.* Lignin-based additive materials: A review of current status, challenges, and future perspectives. *Additive Manufacturing*, v. 74, p. 103711, 25 jul. 2023. Disponível em: https://linkinghub.elsevier.com/retrieve/pii/S221486042300324X. Acesso em: 8 set. 2025.

SHAKYA, A.; VITHANAGE, M.; AGARWAL, T. Influence of pyrolysis temperature on biochar properties and Cr(VI) adsorption from water with groundnut shell biochars: Mechanistic approach. *Environmental Research*, v. 215, p. 114243, 1 dez. 2022. Disponível em: https://linkinghub.elsevier.com/retrieve/pii/S0013935122015705. Acesso em: 25 out. 2025.

SHERWOOD, J. The significance of biomass in a circular economy. *Bioresource Technology*, v. 300, p. 122755, 1 mar. 2020. Disponível em:

https://www.sciencedirect.com/science/article/pii/S0960852420300249. Acesso em: 5 jun. 2026.

SILVA, F. L. DA. *Produção de enzimas lignocelulolíticas e de bioetanol a partir de resíduos da palha de carnaúba (Copernicia prunifera) pré-tratados*. 2017. 157 f. Tese (Doutorado em Biotecnologia). Universidade Federal do Rio Grande do Norte, Natal, 2017. Disponível em: https://repositorio.ufrn.br/jspui/handle/123456789/24948. Acesso em: 9 ago. 2025.

SONG, B. *et al.* Recent advances and challenges of inter-disciplinary biomass valorization by integrating hydrothermal and biological techniques. *Renewable and Sustainable Energy Reviews*, v. 135, p. 110370, 1 jan. 2021. Disponível em: https://www.sciencedirect.com/science/article/pii/S1364032120306584. Acesso em: 5 jun. 2026.

SUN, L. M. *et al.* Biochar production, activation, and applications: A comprehensive technical review. *Carbon Capture Science & Technology*, v. 16, p. 100421, 1 set. 2025. Disponível em: https://www.sciencedirect.com/science/article/pii/S2772656825000600. Acesso em: 26 abr. 2026.

SURYANARAYANA, C. Mechanical alloying and milling. *Progress in Materials Science*, v. 46, n.1-2, p.1-184, Jan. 2021. Disponível em: https://www.sciencedirect.com/science/article/pii/S0079642599000109. Acesso em: 13 mar. 2025.

TAN, H. *et al.* A Review On The Comparison Between Slow Pyrolysis And Fast Pyrolysis On The Quality Of Lignocellulosic And Lignin-Based Biochar. *IOP Conference Series: Materials Science and Engineering*, v. 1051, n. 012075, 2021. Disponível em: https://iopscience.iop.org/article/10.1088/1757-899X/1051/1/012075. Acesso em: 15 ago. 2025.

TAN, I. A. W.; AHMAD, A. L.; HAMEED, B. H. Adsorption of basic dye on high-surface-area activated carbon prepared from coconut husk: Equilibrium, kinetic and thermodynamic studies. *Journal of Hazardous Materials*, v. 154, n. 1–3, p. 337–346, 15 jun. 2008. Disponível em: https://linkinghub.elsevier.com/retrieve/pii/S0304389407014707. Acesso em: 3 jan. 2026.

THENG, B. K. *The Chemistry of Clay-Organic Reactions*. Boca Raton: CRC Press, 2024. v. 1.

TKACZYK, A.; MITROWSKA, K.; POSYNIAK, A. Synthetic organic dyes as contaminants of the aquatic environment and their implications for ecosystems: A review. *Science of The Total Environment*, v. 717, p. 137222, 15 maio 2020. Disponível em: https://linkinghub.elsevier.com/retrieve/pii/S0048969720307324. Acesso em: 30 nov. 2025.

UBANDO, A. T.; FELIX, C. B.; CHEN, W. H. Biorefineries in circular bioeconomy: A comprehensive review. *Bioresource Technology*, v. 299, p. 122585, 1 mar. 2020. Disponível em: https://www.sciencedirect.com/science/article/pii/S0960852419318152. Acesso em: 5 jun. 2026.

UÇURUM, M.; ÖZDEMIR, A. Wet mechanochemical surface modification of calcite employing an integration of conventional design and analytical hierarchy process. *Powder Technology*, v. 443, p. 119970, jul. 2024. Disponível em: https://www.sciencedirect.com/science/article/pii/S0032591024006132. Acesso em: 27 abr. 2026.

UNITED NATIONS GENERAL ASSEMBLY. *Transforming our world: the 2030 Agenda for Sustainable Development*. . New York: United Nations, 21 out. 2015. Disponível em: https://docs.un.org/en/A/RES/70/1. Acesso em: 30 nov. 2025.

VAZAMENTO de 2 mil litros de corante deixa azul água de córrego em SP e afeta animais; veja fotos. *Estadão*. Disponível em: https://www.estadao.com.br/sustentabilidade/vazamento-de-2-mil-litros-de-corante-deixa-azul-agua-de-corrego-em-sp-e-afeta-animais-veja-fotos-nprm. Acesso em: 5 fev. 2026.

WANG, J.; GUO, X. Adsorption kinetic models: Physical meanings, applications, and solving methods. *Journal of Hazardous Materials*, v. 390, p. 122156, 15 maio 2020. Disponível em: https://www.sciencedirect.com/science/article/pii/S0304389420301448. Acesso em: 21 ago. 2025.

WANG, J. *et al.* On the adsorption characteristics and mechanism of methylene blue by ball mill modified biochar. *Scientific Reports*, v. 13, n. 1, p. 21174, 1 dez. 2023. Disponível em: https://www.nature.com/articles/s41598-023-48373-1. Acesso em: 11 nov. 2025.

WANG, L. *et al.* Biochar composites: Emerging trends, field successes and sustainability implications. *Soil Use and Management*, v. 38, n. 1, p. 14–38, 1 jan. 2022. Disponível em: https://bsssjournals.onlinelibrary.wiley.com/doi/full/10.1111/sum.12731. Acesso em: 25 ago. 2025.

WANG, S. *et al.* Lignocellulosic biomass pyrolysis mechanism: A state-of-the-art review. *Progress in Energy and Combustion Science*, v. 62, p. 33–86, 1 set. 2017. Disponível em: https://www.sciencedirect.com/science/article/pii/S0360128517300266. Acesso em: 25 abr. 2026.

WEBER, K.; QUICKER, P. Properties of biochar. *Fuel*, v. 217, p. 240–261, 1 abr. 2018. Disponível em: https://www.sciencedirect.com/science/article/pii/S0016236117316216. Acesso em: 11 ago. 2025.

WEI, X. *et al.* Facile Ball-Milling Synthesis of CuO/Biochar Nanocomposites for Efficient Removal of Reactive Red 120. *ACS Omega*, v. 5, n. 11, p. 5748–5755, 24 mar. 2020. Disponível em: https://pubs.acs.org/doi/10.1021/acsomega.9b03787. Acesso em: 22 abr. 2026.

WIJESOORIYA, M. M. *et al.* Clays and Clay Minerals: Long-Lasting Applications in Environmental Remediation. In: VITHANAGE, M; LAZZARA, G.; RAJAPAKSHA, A. U. (Org.). . *Clay Composites: Environmental Applications*. 1. ed. Singapore: Springer, 2023. p. 3–28. Disponível em: https://link.springer.com/chapter/10.1007/978-981-99-2544-5_1. Acesso em: 28 ago. 2025.

XIE, Y. *et al.* A critical review on production, modification and utilization of biochar. *Journal of Analytical and Applied Pyrolysis*, v. 161, p. 105405, 1 jan. 2022. Disponível em: https://www.sciencedirect.com/science/article/pii/S0165237021003910. Acesso em: 16 ago. 2025.

YAASHIKAA, P. R. *et al.* A critical review on the biochar production techniques, characterization, stability and applications for circular bioeconomy. *Biotechnology Reports*, v. 28, p. e00570, 1 dez. 2020. Disponível em: https://www.sciencedirect.com/science/article/pii/S2215017X20300023. Acesso em: 14 ago. 2025.

YANG, H. *et al.* Characteristics of hemicellulose, cellulose and lignin pyrolysis. *Fuel*, v. 86, n. 12–13, p. 1781–1788, 1 ago. 2007. Disponível em: https://www.sciencedirect.com/science/article/pii/S001623610600490X. Acesso em: 25 abr. 2026.

ZUBAIR, M. *et al.* Adsorption Behavior and Mechanism of Methylene Blue, Crystal Violet, Eriochrome Black T, and Methyl Orange Dyes onto Biochar-Derived Date Palm Fronds Waste Produced at Different Pyrolysis Conditions. *Water, Air, and Soil Pollution*, v. 231, n. 5, p. 1–19, 1 maio 2020. Disponível em: https://link.springer.com/article/10.1007/s11270-020-04595-x. Acesso em: 24 ago. 2025.

APPENDIX A — Bentonite Clay Characterization

This appendix presents the physicochemical characterization of the bentonite clay used in the preparation of biochar–clay composites (BCC). The material was characterized by SEM/EDS, FTIR, XRD, and TG/DTG analyses (Figure A1), providing information on morphology, elemental composition, functional groups, crystalline structure, and thermal stability.

Figure A1 – Characterization of Bentonite Clay

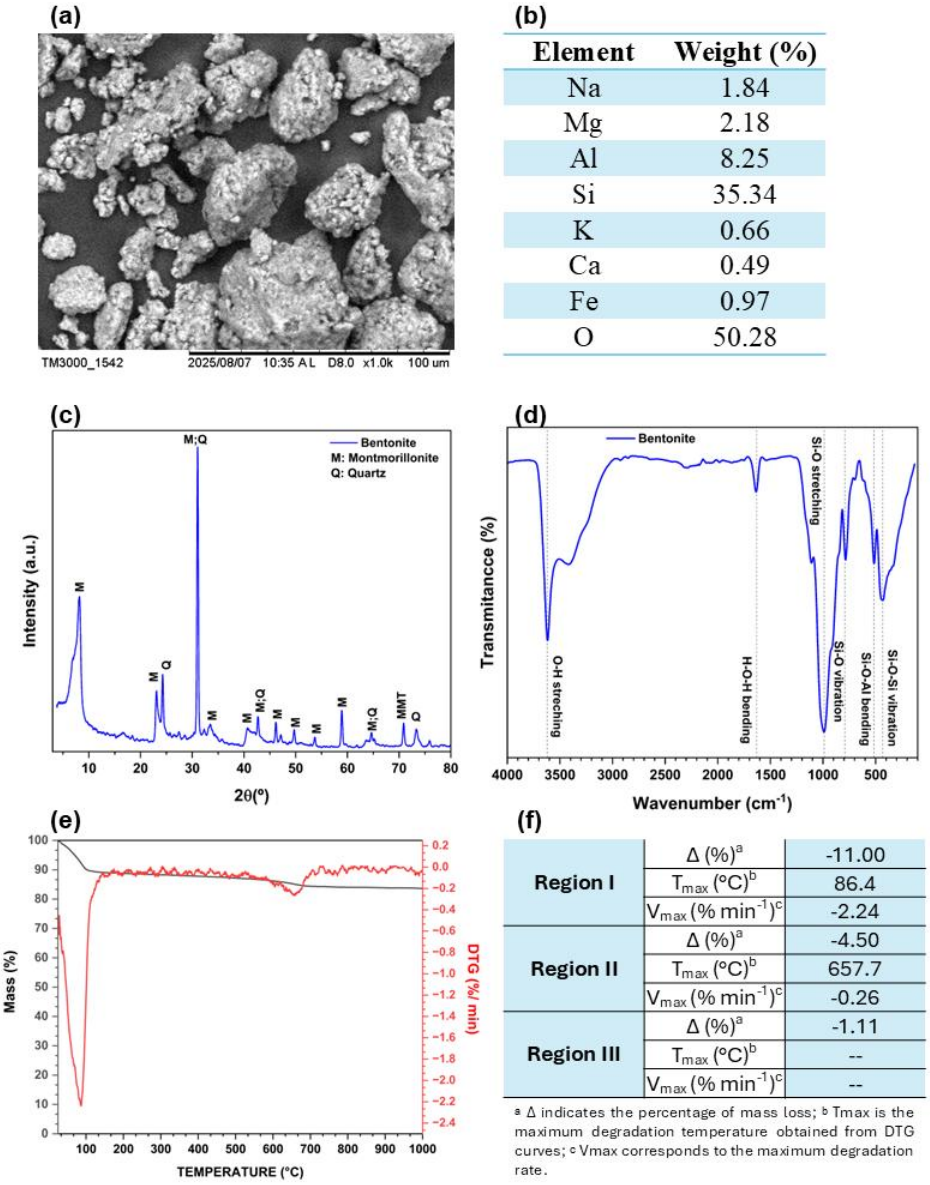

Source: Author

The SEM image (Fig. A1a) reveals irregular and heterogeneous aggregates with no defined geometry, typical of natural clays composed of stacked lamellar structures. This morphology is consistent with bentonites reported in the literature, which commonly exhibit

agglomerated particles with layered features and variable sizes(Daou *et al.*, 2024; Marouf *et al.*, 2021).

The EDS results (Fig. A1b) indicate that the material is mainly composed of O (50.28 wt%), Si (35.34 wt%), and Al (8.25 wt%), confirming its aluminosilicate nature. Minor amounts of Na, Mg, K, Ca, and Fe are also detected, which are commonly associated with exchangeable cations and accessory minerals in bentonite(Marouf *et al.*, 2021). The predominance of SiO_2 and Al_2O_3 is characteristic of montmorillonite-rich clays and is directly related to adsorption and ion-exchange properties(Kumari; Mohan, 2021; Marouf *et al.*, 2021)

The XRD pattern (Fig. A1c) shows the presence of montmorillonite as the main crystalline phase, along with quartz as a secondary phase. The peak around ~8° is attributed to the basal reflection (001) of montmorillonite, while the intense reflection near ~26° corresponds to quartz. Additional peaks in the 20–40° range further confirm the presence of aluminosilicate phases. This phase composition is consistent with typical natural bentonites containing montmorillonite, quartz, and minor mineral impurities(Daou *et al.*, 2024; Marouf *et al.*, 2021).

The FTIR spectrum (Fig. A1d) presents characteristic bands of bentonite. The band at ~3623 cm^{-1} is assigned to structural –OH stretching (Al–OH), while the band at ~1630 cm^{-1} corresponds to bending vibrations of adsorbed/interlayer water. The strong band near ~987 cm^{-1} is attributed to Si–O stretching in the tetrahedral structure, and the bands at ~518 and ~434 cm^{-1} are associated with Si–O–Al and Si–O–Si vibrations, respectively. The band at ~791 cm^{-1} indicates the presence of quartz. These features are consistent with typical FTIR spectra of montmorillonite clays in literature (Daou *et al.*, 2024; Marouf *et al.*, 2021).

Thermogravimetric analysis (Fig. A1e–f) shows three main mass-loss regions. The first region (~up to 150 °C) exhibits a mass loss of ~11%, associated with the removal of physically adsorbed and interlayer water. The second region (centered at ~657 °C) corresponds to a mass loss of ~4.5%, attributed to dehydroxylation of the clay structure. A minor third loss (~1.1%) is observed at higher temperatures, possibly related to residual structural changes. The high residual mass indicates good thermal stability, which is typical of bentonite and has been reported in previous studies (Hamad *et al.*, 2024).

These results indicates that the bentonite used in this study consists predominantly of montmorillonite with typical structural, chemical, and thermal features of natural bentonite. These characteristics support its suitability as a mineral phase in adsorption systems, particularly due to its layered structure, surface heterogeneity, and presence of exchangeable cations(Kumari; Mohan, 2021; Marouf *et al.*, 2021).

APPENDIX B — Calculation of Milling Specific Energy

The milling specific energy was calculated using the equations proposed by Chattopadhyay *et al.* (2001) for the adhesion (continuous cataracting) regime, which is the operative regime of the planetary ball mill under the conditions employed in this work. The calculation procedure followed the approach described in the supplementary information of Lopez-Tenllado *et al.* (2021).

The equations account for the collision velocity, impact frequency, kinetic energy per impact, total transmitted power, and finally the specific energy supplied to the biochar during milling. The following sections present the governing equations, the parameters used in the calculations, and the results obtained for different rotational speeds and milling times used in the present study.

B.1 Analysis of the Detachment Criterion

The original model considers the point where the normal reaction (N) between the ball and the vial wall becomes zero:

$$\mathrm{N} = \mathrm{m}[r_v(\omega_d - \omega_v)^2 + \mathrm{r}_d\omega_d^2\cos\varphi] = 0 \quad \text{Eq. B1}$$

Solving for $cos\varphi$ at the detachment point:

$$cos\varphi = -\frac{r_v(\omega_d-\omega_v)^2}{\mathrm{r}_d\omega_d^2} \quad \text{Eq.B2}$$

Chattopadhyay et al. (2001) defines a detachment parameter (S) from Eq.B2:

$$S = -\frac{r_v(\omega_d-\omega_v)^2}{\mathrm{r}_d\omega_d^2} \quad \text{Eq. B3}$$

Detachment and subsequent impact only occur if $0 \leq \mathrm{S} \leq 1$. Since $\omega_v \gg \omega_d$, therefore $(\omega_d - \omega_v)^2 \approx \omega_v^2$. Thus:

$$|S| \approx \frac{r_v\omega_v^2}{\mathrm{r}_d\omega_d^2} \quad \text{Eq. B4}$$

For the system in question, considering the high energy mill model, the disk radius $r_d = 0.0608$, the vial radius $r_v = 0.0375$, and the angular velocity ratio $\omega_v = 2.82 \cdot \omega_d$, the detachment can be obtained:

$$|S| \approx \frac{0{,}0375 \times (2.82)^2\omega_d^2}{0.0608\ \omega_d^2} \approx 4.9$$

Because $|S| \approx 4.9 > 1$, the detachment condition is never satisfied, confirming that the balls operate in a continuous cataracting (adhesion) regime.

B.2 Adapted Methodology for Adhesion Regime

B2.1 Collision Velocity (v_c)

In the adhesion regime, the relevant velocity is the tangential velocity of the ball relative to the laboratory reference frame, obtained by composition of motions:

$$v_c = \omega_d(r_d + 2.82r_v) \qquad \text{(Eq. B5)}$$

B2.2 Impact Frequency (f)

In the continuous adhesion regime, the ball-vial interaction frequency is governed by the vial rotation:

$$f = \frac{1.82\omega_d}{2\pi} \qquad \text{(Eq. B6)}$$

B2.3 Kinetic Energy per Impact (E_t)

For a ball of mass m_b:

$$E_t = \frac{1}{2} m_b v_c^2 \qquad \text{(Eq.B7)}$$

B2.4 Total Transmitted Power (P_t)

Considering n balls acting simultaneously:

$$P_t = n \cdot f \cdot E_t \qquad \text{(Eq.B8)}$$

B2.5 Milling Specific Energy (E)

The specific energy supplied during milling time t for a mass (m_s) of sample is:

$$E = \frac{P_t \cdot t}{m_s \times 1000} \qquad \text{(Eq.B9)}$$

B2.6 Parameters Used

Table B1 shows the parameters used for calculating the collision velocity, impact frequency, kinetic energy per impact, total transmitted power, and milling specific energy.

Table B1 - Parameters used for calcuating energy of milling

Parameter	Symbol	Value	Unit
Disk radius	r_d	0.0608	m
Vial radius	r_v	0.0375	m
Angular velocity ratio	ω_v/ω_d	2.82	–
Relative angular velocity (normalized)	$\frac{\omega_v - \omega_d}{\omega_d}$	1.82	–
Mass of one ball	m_b	0.0041	kg
Number of balls	n	24	–
Biochar mass	m_s	10	g

Source: Author

B.3 Results

Table B2 shows the specific energy values obtained for different rotational speeds and milling times used in the presented study.

Table B2 - Energy of the milling process for different speed and time conditions

Speed (RPM)	ω_d (rad/s)	Time (h)	Specific Energy (kJ/g)
200	20.94	2	2.62
200	20.94	4	5.24
200	20.94	6	7.86
300	31.42	2	8.82
300	31.42	4	17.64
300	31.42	6	26.46
400	41.89	2	20.91
400	41.89	4	41.82
400	41.89	6	62.73

Source: Author

APPENDIX C – RELATED PUBLICATIONS

This appendix compiles related publications produced during the master's program in which the author participated. While not all of them are directly derived from the results of this dissertation, they are all related to agricultural waste valorization and contributed to the author's academic training.

C.1 Articles

[1] **Silva, L. C.**; Santiago, P. Q.; Sousa, E. F.; Sousa, J. P.; Medeiros, S. L. S.; Nogueira, R. E. F. Q.; Rios, M. A. S. Production and Characterization of Carnauba Straw (*Copernicia prunifera*) Biochar: Influence of Wax Removal on Adsorption of Methylene Blue. *ACS Omega*, 2026, 11(16), 24522–24535. DOI: 10.1021/acsomega.6c00684.

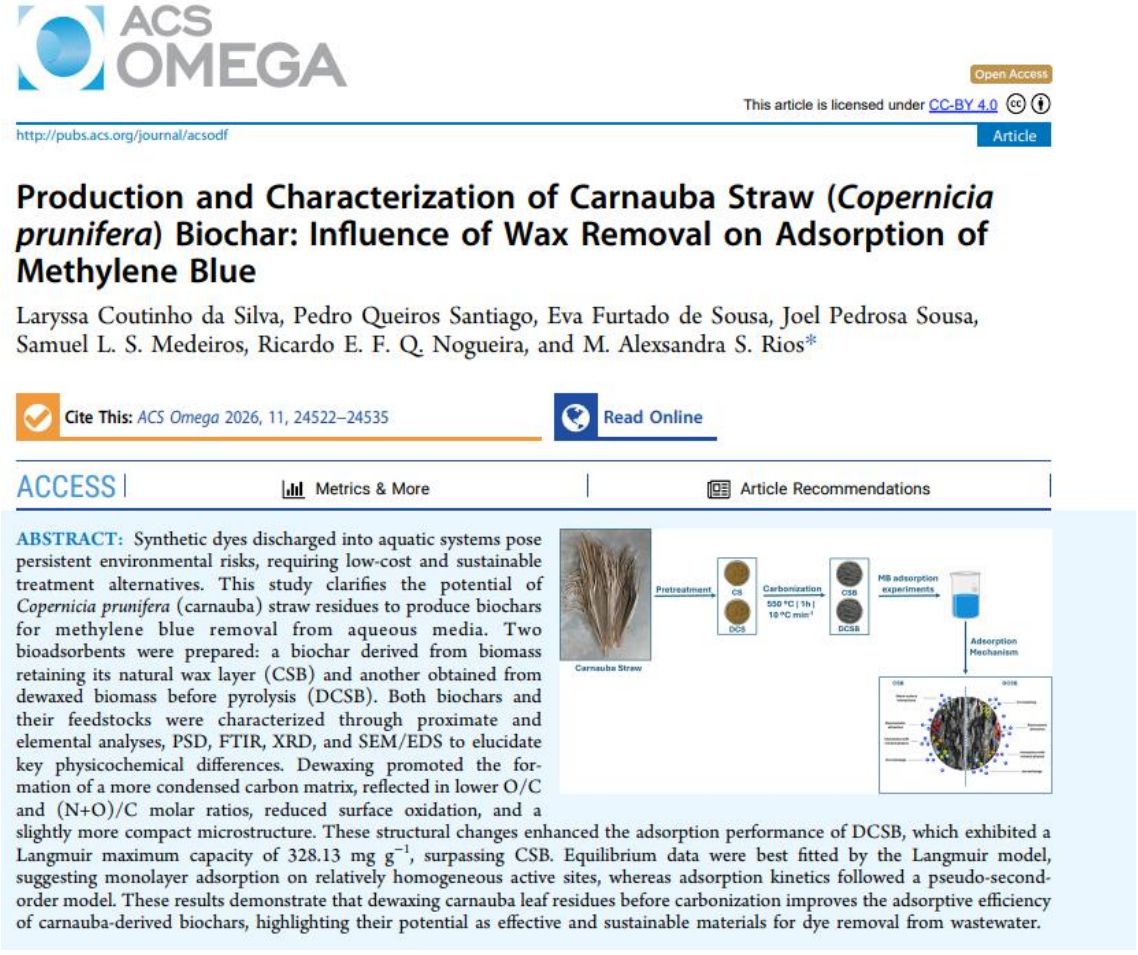

ACS OMEGA

Open Access

This article is licensed under CC-BY 4.0

http://pubs.acs.org/journal/acsodf

Article

Production and Characterization of Carnauba Straw (*Copernicia prunifera*) Biochar: Influence of Wax Removal on Adsorption of Methylene Blue

Laryssa Coutinho da Silva, Pedro Queiros Santiago, Eva Furtado de Sousa, Joel Pedrosa Sousa, Samuel L. S. Medeiros, Ricardo E. F. Q. Nogueira, and M. Alexsandra S. Rios*

Cite This: *ACS Omega* 2026, 11, 24522–24535

Read Online

ACCESS | Metrics & More | Article Recommendations

ABSTRACT: Synthetic dyes discharged into aquatic systems pose persistent environmental risks, requiring low-cost and sustainable treatment alternatives. This study clarifies the potential of *Copernicia prunifera* (carnauba) straw residues to produce biochars for methylene blue removal from aqueous media. Two bioadsorbents were prepared: a biochar derived from biomass retaining its natural wax layer (CSB) and another obtained from dewaxed biomass before pyrolysis (DCSB). Both biochars and their feedstocks were characterized through proximate and elemental analyses, PSD, FTIR, XRD, and SEM/EDS to elucidate key physicochemical differences. Dewaxing promoted the formation of a more condensed carbon matrix, reflected in lower O/C and (N+O)/C molar ratios, reduced surface oxidation, and a slightly more compact microstructure. These structural changes enhanced the adsorption performance of DCSB, which exhibited a Langmuir maximum capacity of 328.13 mg g^{-1}, surpassing CSB. Equilibrium data were best fitted by the Langmuir model, suggesting monolayer adsorption on relatively homogeneous active sites, whereas adsorption kinetics followed a pseudo-second-order model. These results demonstrate that dewaxing carnauba leaf residues before carbonization improves the adsorptive efficiency of carnauba-derived biochars, highlighting their potential as effective and sustainable materials for dye removal from wastewater.

[2] Santiago, P. Q.; **Silva, L. C.**; Sousa, E. F.; Sousa, J. P.; Medeiros, S. L. S.; Rios, M. A. S.; et al. Structural and Chemical Characterization of Carnauba Stalk Biochar (*Copernicia prunifera*) and Its Application in Methylene Blue Adsorption. *Processes* 2026, 14(6), 905. DOI: 10.3390/pr14060905.

processes

MDPI

Article

Structural and Chemical Characterization of Carnauba Stalk Biochar (*Copernicia prunifera*) and Its Application in Methylene Blue Adsorption

Pedro Queiros Santiago [1], Laryssa Coutinho da Silva [1], Eva Furtado de Sousa [2], Joel Pedrosa Sousa [3], Samuel Lucas Santos Medeiros [1], Maria Alexsandra de Sousa Rios [2,*] and Ricardo Emílio F. Q. Nogueira [1]

[1] Department of Metallurgical and Materials Engineering, Center of Technology, Federal University of Ceará, Fortaleza 60440-554, CE, Brazil; pedroqueiros@alu.ufc.br (P.Q.S.); laryssacoutinho@alu.ufc.br (L.C.d.S.); samuel_engmat@ufc.br (S.L.S.M.); emilio@ufc.br (R.E.F.Q.N.)
[2] Department of Mechanical Engineering, Center of Technology, Federal University of Ceará, Fortaleza 60455-760, CE, Brazil; evafurtadodesousa@alu.ufc.br
[3] Department of Geology, Center of Sciences, Federal University of Ceará, Fortaleza 60440-554, CE, Brazil; joelpedrosa@ufc.br
* Correspondence: alexsandrarios@ufc.br

Abstract

The improper discharge of industrial effluents containing dyes, such as methylene blue, represents a serious environmental problem. The present study, therefore, aimed to evaluate the potential of biochar derived from carnauba stalks as an adsorbent for removing dyes from aqueous media. The raw stalks were subjected to carbonization under an inert atmosphere to yield biochar, and both materials were characterized by proximate and elemental analyses, SEM/EDS, PSD, XRD, FTIR, and thermal analyses. Batch adsorption experiments were monitored by UV-Vis spectrophotometry. Pyrolysis resulted in an increase in aromatic fixed carbon (+26.5%) and ash content (+23.8%), while simultaneously reducing volatile matter (−39.3%), moisture, and the atomic H/C (0.39) and O/C (0.07) ratios. Furthermore, thermal stability was enhanced without causing a significant alteration to the average particle size (~30 µm). Adsorption tests showed a maximum uptake of 32.5 $mg \cdot g^{-1}$ at low dosage (2 mg), corresponding to 8.66% removal, while 27.83% removal was achieved at higher dosage (25 mg). Equilibrium data were best described by the Langmuir model (q_m = 210.7 $mg \cdot g^{-1}$; R^2 = 0.971), with q_m representing a theoretical fitting parameter. These findings of this study demonstrate the adsorption potential of carnauba stalk biochar and support its evaluation as a lignocellulosic material for dye removal applications.

Keywords: bioadsorbent; carnauba stalks; methylene blue; dye adsorption; agroforestry residues; wastewater treatment

[3] Soares Do Nascimento, R.; Alves, R.; **Silva, L. C.**; Santiago, P. Q.; Pascoal, C.; Rios, M. A. S.; Quevedo, R. E. F. Evaluation of methylene blue dye adsorption in the composite of babassu coconut biochar – bentonite. *Matéria (Rio de Janeiro)*. **Submitted for publication (Mar.2026).**

C.2 Conference Proceedings

[1] **Silva, L. C.**; Santiago, P. Q.; Nogueira, M. D.; Sousa, E. F.; Soares Júnior, L.; Nogueira, R. E. Q.; Rios, M. A. S. Solid Biofuels from Agrowaste: The Effect of Particle Size in the Thermochemical Behavior of Green Coconut Husk and Safflower Seed Residue. In *Proceedings of the XXIII B-MRS Meeting*; Salvador, Brazil, 2026; p 536. ISBN: 978-85-63273-75-8

Solid Biofuels from Agrowaste: The Effect of Particle Size in the Thermochemical Behavior of Green Coconut Husk and Safflower Seed Residue.

Laryssa Coutinho da Silva[1], Pedro Queiros Santiago[1], Matheus Dias Nogueira[2], Eva Furtado de Sousa[3], Luiz Soares Júnior[4], Ricardo Emilio Quevedo Nogueira[5], Maria Alexsandra de Sousa Rios[4]

[1]Universidade Federal do Ceará (*Departamento de Engenharia Metalúrgica e de Materiais*) , [2]Universidade Federal do Ceará (*Departamento de Engenharia Mecânica*) , [3]Universidade Federal do Ceará (*Departamento de Engenharia de Energias Renováveis*) , [4]Universidade Federal do Ceará (*Departamento de Engenharia Mecânica/ Centro de Tecnologia*) , [5]Universidade Federal do Ceará (*Departamento de Engenharia Metalúrgica e de Materiais/ Centro de Tecnologia*)

e-mail: laryssacoutinho@alu.ufc.br

As the demand for renewable energy grows [1], the valorization of agro-industrial residues as sustainable solid biofuels becomes relevant. This study investigates the thermochemical properties of green coconut husk (GCH) and safflower seed residue (SSR), both byproducts of agro-industrial processes, to evaluate their viability for energy applications. Proximate analysis and Higher Heating Value (HHV) were determined for samples with particle sizes of 250 µm, 710 µm, and 1mm. GCH exhibited higher moisture levels (16.2–18.0%) than SSR (7.2–9.2%), suggesting that SSR may offer superior energy efficiency due to reduced pre-drying requirements. Both materials demonstrated high volatile matter content (GCH: 65.3–77.9%; SSR: 75.4–79.7%), indicating favorable combustion reactivity [2]. Ash content remained low for both residues (GCH: 4.0–6.7%; SSR: 5.4–7.7%), highlighting their potential for minimal post-combustion waste [2]. Notably, fixed carbon content increased with particle size, peaking at 29.4% (GCH) and 18.8% (SSR) for 1000 µm particles, suggesting enhanced combustion stability in coarser fractions. The HHV values confirmed the energy potential of both residues, with GCH exhibiting slightly higher calorific values (18.17–18.99 MJ/kg) compared to SSR (17.98–18.49 MJ/kg). The 710 µm fraction yielded the highest HHV for both materials, suggesting an optimal balance between combustion efficiency and material density. Preliminary results show SSR as a promising high-energy feedstock, while larger GCH particle sizes offer advantages for stable combustion, highlighting the value of agrowaste valorization in circular economy strategies.

[2] Lima, M. D.; Santiago, P. Q.; **Silva, L. C**.; Sousa, E. F.; Melo Neta, M. M. F.; Luna, F. M. T.; Nogueira, R. E. Q.; Rios, M. A. S. Use of Bench-Scale Equipment for the Validation of Protocols for Assessing the Oxidative Stability of Biodiesel. In *Proceedings of the XXIII B-MRS Meeting*; Salvador, Brazil, 2026; p 557. ISBN: 978-85-63273-75-8

Use of Bench-Scale Equipment for the Validation of Protocols for Assessing the Oxidative Stability of Biodiesel.

Mauricio Dorneles Lima[1], Pedro Queiros Santiago[2], Laryssa Coutinho da Silva[2], Eva Furtado de Sousa[3], Maria Marliete Fernandes de Melo Neta[4], Francisco Murilo Tavares de Luna[4], Ricardo Emilio Quevedo Nogueira[5], Maria Alexsandra de Sousa Rios[6]

[1]Universidade Federal do Ceará (*Departamento de Engenharia Química/Programa de Pós-graduação em Engenharia*) , [2]Universidade Federal do Ceará (*Departamento de Engenharia Metalúrgica e de Materiais/PPGECMAT*) , [3]Universidade Federal do Ceará (*Departamento de Engenharia de Energias Renováveis*) , [4]Universidade Federal do Ceará (*Programa de Pós-graduação em Engenharia/ Departamento de Engenharia Química*) , [5]Universidade Federal do Ceará (*Departamento de Engenharia Metalúrgica e de Materiais*) , [6]Universidade Federal do Ceará (*Departamento de Engenharia Mecânica*)

e-mail: mauricio.dorneles@alu.ufc.br

Biodiesel is prone to oxidation when exposed to air, light, and heat, making the addition of antioxidants necessary to maintain its stability. The Rancimat method (EN 14112) is used to assess the effectiveness of these additives. However, the cost and lengthy experimental duration of the Rancimat method prompt the use of alternative techniques such as UV-Vis, fluorescence, and physicochemical properties for monitoring biodiesel oxidation [1]. This study assessed the efficiency of the antioxidants butylated hydroxytoluene (BHT) and 2,4,6 tris(dimethylaminomethyl)phenol (DMP-30) using UV-Vis, acidity index (EN 14104), peroxide index (AOCS Cd 8-53), density, and kinematic viscosity (ASTM D7042). The soybean biodiesel underwent accelerated oxidation in bench-top equipment (BR1020140321802) with antioxidants (1000 mg kg^{-1}) for 14 hours at 110 ± 5 °C. The sample containing DMP-30 exhibited lower values for acidity index (16.02 ± 0.14 mg KOH g^{-1}), density (975.3 ± 0.06 kg m^{-3}), and kinematic viscosity (31.63 ± 0.05 mm^2 s^{-1}), but a higher peroxide index (0.164 ± 0.01 meq kg^{-1}) compared to the sample with BHT. The UV-Vis spectra indicated that, after 14 hours, the samples with BHT displayed a maximum absorbance of 1.114 (247.2 nm), with DMP-30 showing 0.559 (246.8 nm), and the control sample without antioxidants at 0.842 (247.5 nm). DMP-30 was found to be more efficient at inhibiting oxidation thanks to its aromatic amines, which provide better thermal resistance than phenolic antioxidants like BHT [2]. Furthermore, a supplementary approach to Rancimat, simple bench-top equipment, can also be used to validate the quality of biodiesel.

[3] Sousa, E. F.; Coimbra, K. R. G.; **Silva, L. C.**; Santiago, P. Q.; Silva, P. C.; Rios, M. A. S. Physicochemical and Energetic Characterization of Carnauba–Babassu Biomass Blends for Sustainable Solid Biofuel Applications. In *Proceedings of the 34th European Biomass Conference and Exhibition (EUBCE 2026)*; The Hague, Netherlands, 2026. **Accepted for presentation.**